Title
Implementation of a Rotationally Symmetric Ring Ion Trap and Coherent Control of Rotational States

Permalink
https://escholarship.org/uc/item/6nk6w90k

Author
Urban, Erik Gron

Publication Date
2019

Peer reviewed|Thesis/dissertation

Implementation of a Rotationally Symmetric Ring Ion Trap and Coherent Control of Rotational States

by

Erik Urban

A dissertation submitted in partial satisfaction of the

requirements for the degree of

Doctor of Philosophy

in

Physics

in the

Graduate Division

of the

University of California, Berkeley

Committee in charge:

Professor Hartmut Haeffner, Chair
Professor Roger Falcone
Professor Xiang Zhang

Spring 2019

Implementation of a Rotationally Symmetric Ring Ion Trap and Coherent Control of Rotational States

Abstract

Implementation of a Rotationally Symmetric Ring Ion Trap and Coherent Control of Rotational States

by

Erik Urban

Doctor of Philosophy in Physics

University of California, Berkeley

Professor Hartmut Haeffner, Chair

In this thesis, I present the design, implementation, and characterization of a novel, rotationally symmetric ion trap. Our compact design creates a toroidal trapping potential for charged atoms that has a radius that is much smaller than the height at which the ions are positioned above the surface of the trap. We trap ions at a height of 385 μm and a radius of 45 μm as expected from simulation. We demonstrate that this ring is rotationally symmetric with imperfections in the potential of much less than 3 mK.

With two ions contained in a point Paul trap, we demonstrate the creation of a 100 kHz rotating ring using a rotating quadrupole. By releasing the quadrupole potential, we demonstrate the ability to create superpositions of rotational states using the modulation of the laser light produced by the classical rotation of the crystal in a symmetric potential. Superpositions of rotational states differing by up to four quanta are observed.

With these rotational superpositions, we describe an experiment capable of observing the identical nature of two ions in a Coulomb crystal. By creating a rotational interferometer, one can coherently exchange two particles and observe their interference upon recombination. We describe what this interference signature would be and how particle indistinguishability would affect it. We present experimental efforts towards realizing this exchange and reflect on our unexpectedly short rotational superposition coherence times.

To my wife, Heather, who has always supported me through all of our adventures.

Acknowledgments

The completion of a Ph.D. is undoubtedly a team effort and throughout my academic life I have had the immense fortune of being surrounded by a fantastic group of teammates. First and foremost, I need to thank my caring wife, Heather, who not only patiently listened to me think through my physics problems through high school and college, but then picked up everything and moved to California only to listen to more physics problems and practice talks for another six years. I also need to thank my parents who have always encouraged my numerically driven mind to value a broad range of pursuits. Throughout my life, they have made sure I had the opportunity to pursue my goals and to expand my horizons. For that I am immensely grateful.

I do not believe I would be where I am today without the support and advice of the faculty at my undergraduate institution, Hendrix College. I am very grateful for the education provided to me by a small liberal arts college where the availability of the faculty and their willingness to invest time one-on-one with students was a key factor in my success there. I would like to thank two professors in particular. First, a thank you to Dr. Damon Spayde who gave me the opportunity to get involved with research my freshman year and coached me through my academic path during college and into graduate school. And a second thanks to Dr. Todd Tinsely, who was always willing to give a helpful new perspective, taught me how to represent myself, and how to write like a scientist.

Finally, I want to thank my support system at Berkeley. I am indebted to my advisor, Hartmut Häffner, who taught me that there is no such thing as being 'out of ideas'. Hartmut always struck a balance between being an engaged member of the experimental team while giving me enough ownership to practice and grow as a scientist. The community in our lab is one of the things for which I am most grateful. I want to thank my lab-mates who I had the pleasure of working with directly, Hao-Kun, Neil, Boerge, Crystal, Alex, Kai, and Sara not only for their contributions to the work presented here but for sharing their time and laughter with me as well. I'm also grateful to the rest of my lab-mates and friends Dylan, Soenke, Clemens, Eli, Chi-Chi, Maya, Joe, Ryan, Wei-Ting, and Nicole. Thank you to Matt for always being available to bounce ideas off of and thank you to Crystal who throughout the bursts of highs and prolonged lows that are inherent to research, weathered the whole process with me.

Contents

List of Figures

List of Tables

Chapter 1

Introduction

Trapped ions have proven to be a very successful platform for studying quantum mechanical phenomena in a controlled environment. A single ion is a spatially-resolved quantum system with controllable internal degrees of freedom, perfectly identical to all other ions of the same species. Cooled to mK temperatures, they form crystals that have shared motion which can be used to generate complex interactions across the entire system. For these reasons, ions have been used as platforms for quantum simulation, quantum computing, and studying fundamental science with precision measurement. The success of this system motivates the community to increase the technical capabilities of trapped ions in order to improve our current control and open up new avenues of study.

In this thesis, I will describe my work extending the capabilities of trapped ions to include experiments requiring rotational symmetry through implementation of the first symmetric ion ring trap. Rotational symmetry allows one to consider the utility of trapped ions in a qualitatively different energy environment compared to standard trapped ion experiments. Typically, ions are trapped in such a way that their spatial positions are very well confined in all three dimensions within a few tens of nanometers. However with a rotationally symmetric trap, the ions are unconfined in the angular direction which enables a number of interesting properties such as periodic boundary conditions and the ability to rotate. A useful application of these properties includes generating an ion crystal with symmetric spacing and a symmetric vibrational structure. This is important for designing experiments where it is required that each ion interacts with its environment identically to all other ions. Additionally, rotation yields the ability to exchange ions, create large spatial wavefunctions, and achieve new properties of quantized motion. These and other novel properties allow us to consider a new class of experiments to perform with trapped ions.

My thesis is organized as follows. Chapter 2 presents the background fundamentals of ion trapping including the operation of linear Paul traps and the dynamics of Coulomb crystals. Chapter 3 continues the background with a description of the calcium atom and how it can be manipulated through optical addressing.

Chapter 4 begins my personal work where I describe the design and implementation of a rotationally symmetric ring ion trap. The design and fabrication of the trap was done

in collaboration with the Zhang group in the mechanical engineering department of UC Berkeley with the goal of creating a spacetime crystal as described by Li et al. [1]. The design was envisioned such that even if the symmetry of the ring would be distorted by stray electric fields as appear in all surface ion traps, the symmetry could be restored through the use of only a few field compensating electrodes. Demonstration of the viability of such a trap was the first goal. We crystallized over 15 ions in a ring with a radius of 47 μm at a height of 385 μm as expected from our simulations. In Chapter 5, I continue the evaluation of this trap by characterizing our ability to restore the symmetry of the ring and achieve a translationally invariant environment. We found our design to be successful as we were able to restore the symmetry of the ring such that any imperfections in the potential landscape were much lower than the temperature of the ion crystal (3 mK), a previously unrealized benchmark. The viability of this platform as a future tool is dependent on the degree of control we can exert over it. To this end, Chapter 6 discusses our ability to perform optical spectroscopy on the ring and our ability to manipulate the temperature of the crystal and well as its angular orientation.

In Chapter 7, I discuss a more advanced protocol for gaining precise control over the classical rotation of the ion crystal and creating quantum superpositions of rotational states. These experiments are done with the same trap as those of the previous chapter, however, the trap is operated in a different configuration such that the trapping location for the ions is a single point rather than a ring. Loading two ions into such a trap also creates a ring but with a much smaller radius, about 3 μm. The protocol established in this chapter would extend to much larger rings; however, many elements are easier with a smaller system. Using a rotating quadrupole, we are able rotate a two ion crystal up to 350 kHz. Then, by decreasing the size of the quadrupole, we release the ions into a symmetric potential where they continue to rotate. This free rotation allows us to drive coherent transitions between rotational states using a laser beam which is modulated by the rotational motion of the ions, thereby creating quantum superpositions of rotational states. We observe this rotational superposition by driving Rabi oscillations as well as running a Ramsey experiment and observing the expected behavior.

Finally, in Chapter 8, I discuss a potential application of such rotational superpositions. Using coherent superpositions of rotational states, we can set up a rotational interferometer and use it to coherently exchange the two ions in our trap. This can be used to demonstrate the indistinguishability of two well-separated ions in a Paul trap. In this chapter I discuss how we create the rotational interferometer, the theoretical expected signature of the interferometer, and how indistinguishability would affect these results. I discuss the experimental requirements for such an experiment and our progress in realizing those requirements. Finally, I conclude by reflecting upon the coherence of the rotational interferometer which is much lower than theoretically expected.

Chapter 2

Ion Traps

Trapped ions are powerful model system for studying quantum phenomena. When trapped, their mutual Coulomb repulsion causes them to form crystals with spacings on the order of microns. Therefore, ions are a natural way to create a system of identical, spatially-resolved, model quantum objects with controllable internal degrees of freedom that can interact through shared vibrational motion. This makes them very useful for solving problems where Hamiltonians can be mapped onto interacting, individual sites such as some quantum simulation problems, quantum computing, and other fundamental physics questions. All of the work done in this thesis is done with ion crystals trapped in a radio frequency Paul trap. In this chapter, I will describe the operational theory behind Paul traps as well as the dynamics of ion crystals trapped within them.

2.1 Paul Traps

Interaction with Electric Fields

Because ions have a permanent electric charge, electric fields are a natural method of confinement. However, static electric fields have the property that they cannot be confining in all dimensions simultaneously. This comes out of Laplace's equation,

$$\Delta V = \frac{\partial^2 V}{\partial x_1^2} + \frac{\partial^2 V}{\partial x_2^2} + \frac{\partial^2 V}{\partial x_3^2} = 0, \tag{2.1}$$

where V is the electrical potential and x_1, x_2, and x_3 are orthogonal spatial dimensions. In order to be trapping in the ith dimension, the force generated by the potential V must be restorative, i.e. $\frac{\partial^2 V}{\partial x_i^2} < 0$. However, since the sum of the field gradients in all three dimensions must be zero according to Equation 2.1, if the potential is trapping in any dimension, it must be anti-trapping in at least one other dimension.

In order to create a 3D confining potential, one can use radio frequency (RF) fields in a quadrupole configuration such as given here:

$$V_{RF} = V_0 \sum_i \frac{\alpha_i x_i^2}{r_0^2} \cos(\Omega_{RF} t). \tag{2.2}$$

where i indexes the spatial dimensions, V_0 is the amplitude of the potential, α_i is the size of the quadrupole in the ith dimension, r_0 is a characteristic length scale, Ω_{RF} is the oscillation frequency, and t is time. With RF quadrupole fields, at any given point at least one dimension is anti-confining because $\sum_i \alpha_i = 0$; however, with careful choice of parameters the motion of the ion over many RF periods is on average confining. Such traps are known as Paul traps [2].

Consider the dynamics of ion motion in the potential $V_{RF} + V_{DC}$ where V_{DC} is an additional time-independent potential. The force felt on an ion in a single dimension is $F_i = -e\frac{\partial V}{\partial x_i} = 2e(\frac{\partial V_{DC}}{\partial x_i} + V_0 \cos \Omega_{RF} t)\frac{\alpha_i x_i}{r_0^2}$. This leads us to the differential equation:

$$\ddot{x}_i + \frac{2e\alpha_i}{mr_0^2}(V_{DC} + V_0 \cos(\Omega_{RF} t))x_i = 0 \tag{2.3}$$

This takes the form of the Mathieu differential equation [2]

$$\frac{d^2 u}{d\xi^2} + (a - 2\cos(2\xi))u = 0 \tag{2.4}$$

if $a_i = \frac{-8\alpha_i e V_{DC}}{mr_0^2 \Omega_{RF}^2}$ and $q_i = \frac{4\alpha_i e V_0}{mr_0^2 \Omega_{RF}^2}$, and $\xi = \frac{1}{2}\Omega_{RF} t$.

Leibfried et al. describe a class of solutions to this equation which are stable and periodic given certain relationships between a_i and q_i [3]. That is to say with appropriate choice of V_0 (which can be converted to the voltage applied to the trap), Ω_{RF} (the drive frequency), and V_{DC} (the static fields), one can create a time-averaged 3D stable trap for charged particles. For $a_i < q_i \ll 1$, the Mathieu equation takes the following form:

$$x(t) = A_i \cos(\beta_i \frac{\Omega_{rf}}{2} t)[1 - \frac{q_i}{2} \cos(\Omega_{RF} t)] \tag{2.5}$$

where A_i is the amplitude of motion and $\beta_i = \sqrt{a_i + q_i^2/2}$.

This formula for the classical trajectory of the ion has two interesting features. Firstly, the particle moves as if trapped by a harmonic potential with frequency $\beta_i \Omega_{RF}/2$. This is known as 'secular' motion. Secondly, the amplitude of the secular motion is modulated at the RF frequency with a depth of $q_i/2$. This modulation is driven by RF fields present away from the exact RF null. The trapping point of the quadrupole trap has no dipole field present; however, the DC potential might move the ion off the electric field null. This modulated motion is called 'micromotion' and increases as the ion is moved away from the RF null by DC fields.

Collectively, the effective potential that generates this harmonic motion is known as the 'pseudopotential,' Ψ, where $\Psi = \frac{e^2}{4m\Omega_{RF}^2}|\vec{E}|^2$ where $\vec{E}$ is the maximum instantaneous field produced by the RF potential. One can think of the pseudopotential as the force an ion experiences averaged over many RF cycles. The trapping nature of the pseudopotential can

be understood intuitively as follows. At any given instant near the RF null, the amplitude of the electric field increases with distance. Therefore, when an atom experiences an outward, anti-trapping force at one phase of the RF, it moves outward; however, when the potential changes phase, the ion then experiences an even stronger RF field pointing back towards the RF null, the trapping point. Within a cycle, this results in a time-averaged force towards the trapping point that increases linearly with distance, i.e. a harmonic trap. However, if the RF drive becomes too strong, the ion moves through the RF null as the phase of the RF changes, parametrically imparting more energy to the ion each half cycle of the RF and causing the trapping potential to be unstable. This instability occurs at lower powers for lighter ions, because they are accelerated more for the same field strength. Additionally, the instability manifests earlier at lower RF drive frequencies because the ions have more time need to reach a smaller velocity in order to cross the RF null before the phase of the drive changes.

Types of Paul Traps

3D Macro Traps

Traditional ion traps for quantum information processing are known as 3D blade traps. In such a trap, the quadrupole potential is created using four, linear metal blade electrodes, as shown in Fig. 2.1. RF voltage is applied to one pair of opposite blades in-phase with one another. The other pair of blades is either held at ground or applied the same voltage out-of-phase with the original pair. This yields a quadrupole RF field at the center of the trap. As discussed in the previous section, this creates an RF null where ions can be trapped if the voltages on the blades are varied at the appropriate frequencies. Confinement out of the plane is created by DC end caps (not shown in Fig. 2.1).

The traps are very deep (several eV), have little electric field noise at the ion location, and are easy to make. Unfortunately, they are bulky and not very customizable.

Linear Surface Traps

In order increase the compactness and customizability of the trap, the surface trap was first developed by Chiaverini et al. [4]. 3D traps naturally evoke the shape of a quadrupole field; however, there are other ways to create that field geometry. For example, one can continuously morph the blades of a 3D trap into a single plane and maintain the characteristic quadrupole field. Fig. 2.2 shows how the cross section of a 3D trap can be morphed into a single plane by moving three of the blades into a plane and moving the fourth to infinity without distorting the qualitative structure of the electric fields near the trapping point.

By moving all electrodes into a plane, one can now design traps on small chips. Chip design allows ion traps a much higher degree of customizability and precision manufacturing. Electrodes on chips can be fabricated much closer to one another and have much more customizability demonstrated by the numerous creative designs currently made from surface
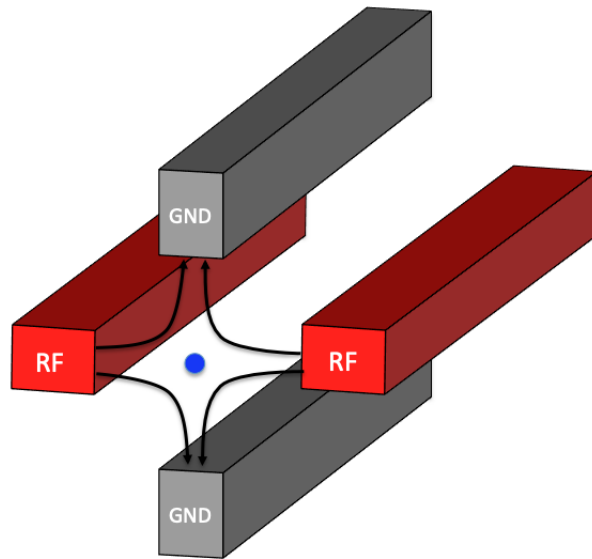
Figure 2.1: Cartoon example of a 3D linear trap. Black arrows represent the instantaneous electric fields produced by the electrodes. A single ion is shown at the trapping location.
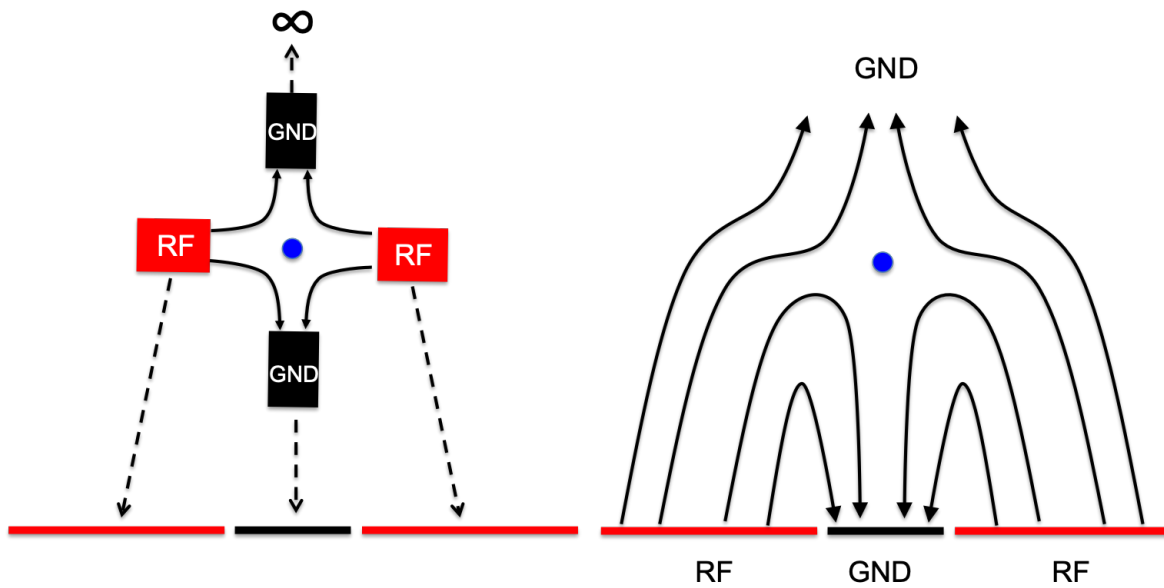
Figure 2.2: Left: Cross section of 3D trap shown in Fig. 2.1 with dashed arrows showing the equivalent electrode in a surface trap. Right: Electric fields produced by a surface trap.

traps [5, 6, 7, 8]. Chapters 4 and 5 of this thesis will focus on the design and implementation of a new type of surface ion trap.

2.2 Coulomb Crystals

In the presence of a trapping pseudopotential, ionized atoms can be held almost indefinitely, up to 10s of hours depending on the vacuum quality. Under Doppler cooling conditions for Calcium (to be discussed in Section 3.3) and with a secular trap frequency of 1 MHz, the potential felt by a single ion is very well approximated as a 3D harmonic trap and the ion is localized within a standard deviation of 16 nm.

If a second ion is placed in the trap, the ions' mutual Coulomb repulsion causes them to displace from the original trapping location along the direction of weakest confinement. Most ion traps are designed such that the potentials they create are weakest in the dimension confined by DC fields. This way, the displaced ions do not experience additional micromotion. If more ions are loaded into the trap, they will form a chain along the axis of weakest confinement where ion positions are dictated by the balance of their coulomb repulsion and the trap frequency, given in the equation below:

$$\forall i, \sum_{j \neq i} \frac{e^2}{4\pi\epsilon_0(x_i - x_j)^2} = m\omega_{\text{trap}}^2 x_i \tag{2.6}$$

where i and j label the ion, e is the fundamental charge, ϵ_0 is the vacuum permittivity, x is the ion position along the crystallization axis, m is the ion mass, and ω_{trap} is secular trap frequency in the direction of weakest confinement. Well-localized ions within a trap are known as Coulomb crystals.

The collective motion of Coulomb crystals can be analyzed in a normal mode picture. The motion of each ion is coupled to those around it through the Coulomb force. Each ion introduces three motional degrees of freedom into the system. A chain of N ions possess $3N$ normal modes. The frequency and ion participation of each of these modes can be found by solving for the eigenvalues and vectors of the Hessian of the system energy.

The energy of ion i in a Coulomb crystal is

$$E = \sum_i \left(\frac{1}{2}m\omega_{\text{trap}}^2 x_i^2 + \sum_{i \neq j} \frac{e^2}{4\pi\epsilon_0(x_i - x_j)} \right). \tag{2.7}$$

Therefore, the Hessian for this system is

$$H_{i,j}(E) = \frac{\partial^2 E}{\partial x_i \partial x_j} = \begin{cases} m\omega_{\text{trap}}^2 + \sum_{i \neq j} \frac{e^2}{\pi\epsilon_0 |x_i - x_j|^3}, & \text{if } i = j \\ -\sum_{i \neq j} \frac{e^2}{2\pi\epsilon_0 |x_i - x_j|^3}, & \text{if } i \neq j \end{cases}. \tag{2.8}$$

From this Hessian we can find the eigenvectors and eigenfrequencies of the ions' motion.

$$H(E)\vec{r}_\lambda = m\omega_\lambda^2 \vec{r} \tag{2.9}$$

where $\vec{r}_\lambda$ is the eigenvector of the motional mode and ω_λ is that mode's motional frequency.

The formation of Coulomb crystals is one of hallmark properties of ion traps. The well-defined spatial separation of ion crystal allows for individual manipulation of a group of

quantum systems, a property not possessed by other cold atom platforms. But in addition to individual addressability, we have shown that they are also coupled through their collective harmonic motion. In this way, not only does one have individually separated, controllable, identical quantum systems, but a means by which one can manipulate and couple them collectively.

Chapter 3

The Calcium Atom and Laser Interactions

Generally, trapped ion experiments can be done with any charged particle, including molecules [9] and highly charged atoms [10]; however, ionized Alkali earth metals are by far the most common atoms used due to the fact that after a single ionization event, one valence electron remains giving the atom a hydrogen-like level structure. Within this group, a single atom can be chosen for a number of reasons including but not limited to its mass, the frequency of its electronic transitions, and the stability of its electronic states against spontaneous decay or magnetic field fluctuations. In all experiments presented here, ^{40}Ca$^+$ is used. In this chapter, I will present its properties and typical methods of control.

3.1 The Calcium Atom

A ^{40}Ca$^+$ ion has a single valence electron giving it a hydrogen-like level structure. It has no nuclear spin and therefore no hyperfine structure. The calcium ion has two groups of electronic levels which are utilized in this work. The first forms a fast cycling manifold which is used to Doppler cool the ion and for state readout (Section 3.3) shown on the left in Fig. 3.1. The $4S_{1/2}$ electronic ground state of ^{40}Ca$^+$ is separated from the $4P_{1/2}$ level by 397 nm. This excited state has a line-width of 23.2 MHz and a lifetime of 6.87 ns [11]. The majority of the time the excited state decays to the ground state; however, it has a 1:15 branching ratio to the $3D_{3/2}$ state [12]. This state can be repumped with 866 nm light. This closes the level structure so the S to P transition may be driven indefinitely without losing population.

The second group of electronic states are used for qubit manipulation, shown on the right in Fig. 3.1. The $3D_{5/2}$ state lies 729 nm above the ground state. The transition between these two states is dipole forbidden, meaning they are not coupled through the magnitude of oscillating dipole electric fields, but their gradients. Therefore, the $3D_{5/2}$ state is a metastable state with a lifetime of 1.17 s and sub-Hz linewidth [13]. Although the transition is dipole

forbidden, with sufficient power the transition can be driven coherently. For this reason, we use the S and D levels as qubit states (Section 3.4). Because the linewidth is so narrow, one can individually address the transitions between each of the Zeeman lines within the manifold. There are two Zeeman sub-levels for the ground state and six for the $3D_{5/2}$ state. The 1.17 s lifetime of the D state is nearly infinite for the purposes of our experiments; however, the population in that state can be reinitialized to the ground state by repumping to the $4P_{3/2}$ with an 854 nm laser where the population quickly decays back to the ground state.
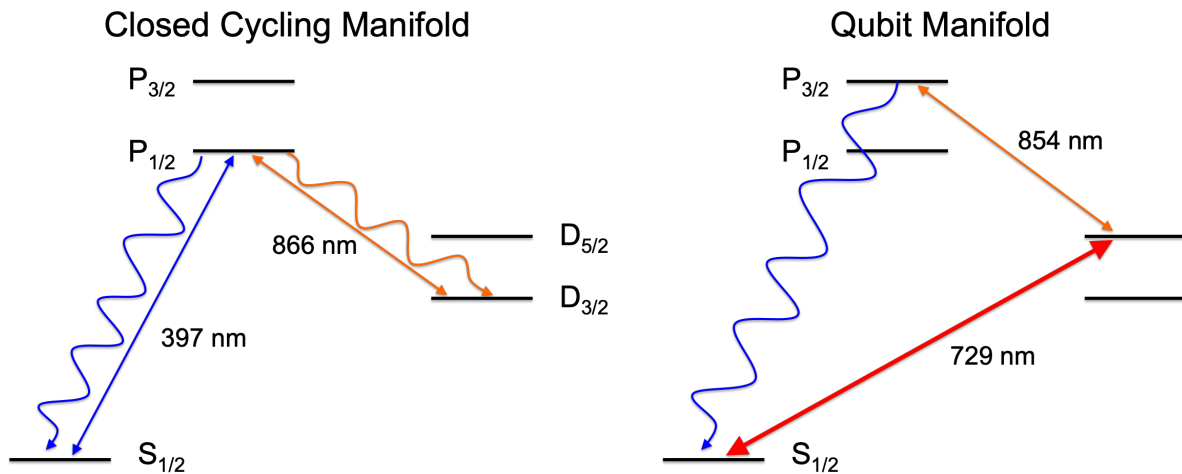
Figure 3.1: Relevant electronic energy levels within a $^{40}\text{Ca}^+$ ion. Left: Cycling manifold used for cooling. Straight arrows represent coupling by lasers and curved arrows spontaneous emission paths. Right: Qubit manifold with the relevant couplings and decays labeled.

3.2 Ion Production

Calcium ions are first produced from a neutral, bulk calcium source. For this, we use a Calcium 'oven'. This oven is made of a small steel tube a few mm in diameter loaded with neutral calcium grains. The calcium grains must be stored in an oxygen free environment as they oxidize after about one hour in air. Once in the oven and in vacuum, 2-5 A of current is run through the oven to sublimate the calcium. Aiming the oven towards the ion trap, a spray of neutral calcium passes over the trap and can be ionized. The neutral atom is ionized by a pair of laser beams. The first resonantly excites the atom to the $P_{1/2}$ state at 422 nm. After being excited, the neutral calcium is ionized by exciting the electron into the continuum with a 375 nm laser beam.

Though the calcium oven is not very precise in the direction that it sprays, one must be careful of its alignment. In order to capture ions, one must ionize calcium within the trapping volume a few hundred microns above the surface of the trap but at the same time

be careful not to coat the trap surface itself in calcium. Though calcium is a conductor, it can still form insulating oxide layers in vacuum. Therefore, any residue on the surface of the trap could begin to charge resulting in large, unstable fields at the trapping location. In order to precisely align the flow of neutral calcium, we use its fluorescence. To begin, the oven is aligned well below the trap as shown in Fig. 3.2. In this way, the clamp holding the trap to the breakout board shields the trap itself from the calcium. With the 422 nm laser positioned above the trap, we can detect the fluorescence of the neutral calcium with a photomultiplier tube (PMT) and observe the height at which the calcium beam is being shielded by adjusting the height of the 422 nm laser and observing the point at which the fluorescence disappears. Finally, we slowly raise the oven, thereby lowering the height at which the calcium passes over the trap, until we detect fluorescence at the trapping location but not below it.
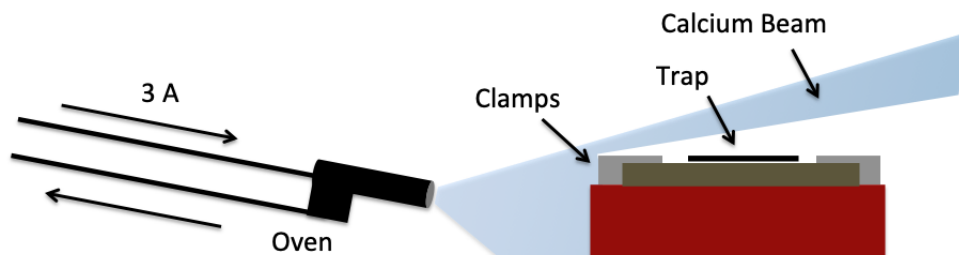
Figure 3.2: Configuration of the neutral calcium oven relative to the trap used for ion loading (not to scale).

3.3   Laser Cooling

With ions present within the trapping region, the pseudopotential will force them towards the trap center. However, without any dissipative forces, the ions will not crystalize. In this section, I will present several methods used to extract energy from the ions, or cool, via laser interactions. In any given experiment, some or all may be used.

Doppler Cooling

The first stage of cooling in all of our experiments is Doppler cooling. Doppler cooling is implemented using 397 nm light to drive the S to P transition in combination with 866 nm repump to prevent population leakage. The lifetime of the $4P_{1/2}$ level is 6.87 ns; therefore absorption and reemission events happen much faster than the motional period of the ion (around 1 μs). In this limit, the velocity of the ion can be modeled as constant during one of these events and a semiclassical analysis of Doppler cooling can be performed where the cooling force is modeled as a velocity dependent radiation pressure [3].

Doppler cooling can be performed on many motional modes of the ion crystal (Eq. 2.9) simultaneously as long as the cooling laser has projection along the mode's eigenvector; however, for this analysis we will consider only a single mode. The velocity of a trapped ion as a function of time is $v = v_0 \cos \omega_t t$ where v_0 is the amplitude of the velocity and ω_t is the trap frequency. If the laser is propagating in the positive direction with wavevector $\vec{k}$, every absorption event changes the momentum of the atom by $\Delta p = \hbar k$. Since the excited state has an angular momentum $J = 1/2$, emission of the photon is isotropic [14] and therefore will add zero momentum to the ion on average. However, the emission does create a random walk in momentum space which is the equivalent to a heating process which we will consider later.

The force felt on the ion is $F = dp/dt$. As stated before, $\Delta \vec{p} = \hbar \vec{k}$ for every absorption event. In order to absorb again, the ion must dissipate the energy through spontaneous emission. Therefore, the rate of emission is the product of the excited state lifetime, Γ, and the chance of the atom being in the excited state, ρ_{ee}. Therefore,

$$\vec{F} = \hbar \vec{k} \Gamma \rho_{ee}. \tag{3.1}$$

Leibfried et al. [3] gives the excited state population as

$$\rho_{ee} = \frac{s/2}{1 + s + (\frac{2\delta}{\Gamma})^2} \tag{3.2}$$

where s is the saturation parameter ($s = \frac{2|\Omega|^2}{\Gamma^2}$ where Ω is the resonant Rabi frequency) and $\delta = \Delta - \vec{k}\vec{v}$ where Δ is the laser detuning from resonance. In the limit where the Doppler shift is small ($\vec{k}\vec{v} << 1$), which is the case when the ion is cold, the force on the ion can be expanded to

$$\vec{F} = \hbar \vec{k} \Gamma \frac{s/2}{1 + s + (\frac{2(\Delta - \vec{k}\vec{v})}{\Gamma})^2} \approx \hbar \vec{k} \Gamma \frac{s/2}{1 + s + (\frac{2\Delta}{\Gamma})^2} \left(1 + \frac{8\vec{k}\vec{v}\Delta}{\Gamma^2(1 + s + (2\Delta/\Gamma)^2)} \right). \tag{3.3}$$

The rate at which this force puts energy into (or out of) the system, $\dot{E}_c$, is $\langle \vec{F}\vec{v} \rangle$ which comes out to

$$\dot{E}_c = \hbar \vec{k} \Gamma \frac{s/2}{1 + s + (\frac{2\Delta}{\Gamma})^2} \left(\langle \vec{v} \rangle + \frac{8\vec{k}\Delta}{\Gamma^2(1 + s + (2\Delta/\Gamma)^2)} \langle v^2 \rangle \right) \tag{3.4}$$

As $\langle v \rangle = 0$ for a trapped particle, we finally solve that the rate at which energy is put into the system by absorption is

$$\dot{E}_c = \hbar \vec{k} \Gamma \frac{s/2}{1 + s + (\frac{2\Delta}{\Gamma})^2} \left(\frac{8\vec{k}\Delta}{\Gamma^2(1 + s + (2\Delta/\Gamma)^2)} \langle v^2 \rangle \right). \tag{3.5}$$

From this equation we can gain an intuitive understanding of how Doppler cooling works. If Δ is negative, the rate at which the energy flows into the system is negative, i.e. cooling. This can be understood as when the laser is red-detuned from resonance, the ion preferentially absorbs photons when traveling towards the light field; therefore, absorption events are biased towards times when absorption slows the atom rather than accelerating it.

Until this point we have ignored the heating accrued by spontaneous emission mentioned earlier. Because the absorbed photon is reemitted in a random direction, this causes a random walk in momentum space which is equivalent to a heating mechanism. As a random walk process around 0, the uncertainty in the final momentum is the step size of the momentum walk ($\hbar k$) squared times the number of steps, N:

$$\langle p^2 \rangle = \sigma_p = \hbar^2 k^2 N. \tag{3.6}$$

In this case, the heating rate, $\dot{E}_h$ would be

$$\dot{E}_h = \frac{1}{2m}\frac{d\langle p^2 \rangle}{dt} = \frac{(\hbar k)^2}{2m}\Gamma\rho_{ee}(1+\xi) \tag{3.7}$$

where m is the mass of calcium, $\Gamma\rho_{ee}$ is the rate of absorption events found earlier, and ξ is a geometrical factor of 2/5 derived in Leibfried et al. [3] that accounts for an additional random walk process that occurs during absorption due to the varying phase of the ion motion at which absorption occurs.

Equating $\dot{E}_c = \dot{E}_h$, we find the minimum achievable temperature to be

$$T_{min} = \frac{\hbar\Gamma}{4k_B}(1+\xi) \tag{3.8}$$

for small powers ($s << 1$) where k_B is Boltzmann's constant and when $\Delta = \Gamma/2$. For ^{40}Ca$^+$, this temperature comes out to 0.29 mK.

This derivation was semi-classical in the sense that the velocity can be modeled as oscillatory with a certain amplitude, v_0. However, when the ion is very cold, this does not capture the full picture as 0.3 mK corresponds to only 6 quanta of occupation in a harmonic oscillator with a trap frequency of 1 MHz. Therefore in this regime, we must be careful how we define temperature. From now on, when referring to temperature we mean that if we perform cooling on an ion, if we were to collapse to wave function into the Fock state basis, we would find it in state $|n\rangle$ with a probability defined by a thermal distribution parameterized by the temperature, T such that

$$P(|n\rangle) = P_0 e^{n\hbar\omega_t/k_B T}. \tag{3.9}$$

When averaging over many experiments (typically 100 in our case), this definition of temperature proves useful.

Sideband Cooling and Quantized Interaction with a Light Field

In many experiments, temperatures below the Doppler limit are required. There are several ways to achieve sub-Doppler temperatures; however, the most common method used in the work is resolved sideband cooling. But in order to understand sideband cooling, we must first understand quantized interactions between the ion and light fields. Since the $S_{1/2}$ to $D_{5/2}$ transition is less than 1 Hz wide, with a sufficiently narrow laser (< 200 Hz) we can address each pairing of Zeeman sublevels between the two electronic states individually and model any given pair as a two level system. In addition to electronic levels, the atom also possesses motional degrees of freedom. As discussed in Section 2.2, this motion can be modeled as many harmonic oscillators with trap frequencies ω_i. Therefore, the Hamiltonian for the bare atom in this system is

$$H_0 = \hbar \frac{\omega_e}{2} \sigma_z + \sum_i \hbar \omega_i (a_i^\dagger a_i + 1/2) \tag{3.10}$$

where ω_e is the energy difference between the two electronic states, σ_z is the z-Pauli spin operator, i indexes the motional modes of the ions, ω_i is the trap frequency of the ith normal mode, and $a_i^\dagger$ and a_i are the raising and lowering operators respectively for the ith mode.

As found in [3], the coupling between two levels by a narrow frequency laser field is

$$H_{int} = \frac{\hbar \Omega_0}{2} \sigma_+ e^{i(kx_i \cos\theta - \omega_L t + \phi)} + h.c. \tag{3.11}$$

where Ω_0 is the resonant Rabi frequency, k is the magnitude of the wavevector of the laser, x is the spatial dimension along the motional mode, θ is the angle between k and x, and ω_L is the frequency of the applied laser field.

Since we will be dealing with harmonic oscillator Fock states, it is useful to make the substitution $\vec{k}\vec{x}_i = kx_i \cos\theta \sqrt{\hbar/2m\omega_i} = \eta_i(a + a^\dagger)$. η is known as the Lambe-Dicke parameter and typically is a useful expansion parameter. It is also a measure of the ratio of the laser wavelength to the size of the ground state wave function of the harmonic oscillator. Making this substitution,

$$H_{int} = \frac{\hbar \Omega_0}{2} \sigma_+ e^{i(\eta_i(a + a^\dagger) - \omega_L t + \phi)} + h.c. \tag{3.12}$$

When this interaction Hamiltonian is applied to the eigenstates of H_0, coupling can be engineered between many different states depending on the detuning. Specifically, when detuned from the electronic transition by an integer multiple, m, of the trap frequency ω_i, we find non-zero couplings. From [3],

$$\Omega_{n,n+m} = \Omega_0 |\langle n + m | e^{i\eta_i(a+a^\dagger)} | n \rangle| = \Omega_0 e^{-\eta^2/2} \eta^{|m|} \sqrt{\frac{n_<!}{n_>!}} L_{n_<}^{|s|}(\eta^2) \tag{3.13}$$

where n is the quantum number of the harmonic oscillator Fock state $|n\rangle$, $n_<$ is the lesser of n and $n + m$, and $L_a^b(X)$ is the generalized Laguerre polynomial,

$$L_a^b(X) = \sum_{j=0}^{a} (-1)^j \binom{a+b}{a-j} \frac{X^j}{j!}. \tag{3.14}$$

These couplings at integer multiples of the trap frequency are known as sidebands. If m is positive, they are called blue sidebands as they require a blue detuning from the electronic resonance known at the carrier. Physically, they correspond to an absorption of a photon as well an an increase in the motional quantum number by m. Similarly, if m is negative, the transition is known as a red sideband by the same logic and corresponds to a reduction of the motional quantum number by $|m|$.

In most trapped ion systems, η is small (0.097 for a 1 MHz mode addressed by 729 nm light) and the ions are cold; therefore, it is natural to expand Equation 3.13 in $\eta(a_i + a_i^\dagger)$. It can now be written as

$$\Omega_{n,n+m} = \Omega_0 |\langle n+m|e^{i\eta_i(a+a^\dagger)}|n\rangle| \approx \Omega_0 |\langle n+m|(1 + i\eta_i(a_i + a_i^\dagger) - \frac{1}{2}\eta_i^2(a_i + a_i^\dagger)^2)|n\rangle|. \tag{3.15}$$

So to second order, the couplings to the sidebands are

$$\Omega_{n,n+m} = \Omega_0 \begin{cases} (1 - \eta^2 n), & \text{if m} = 0 \\ \eta\sqrt{n}, & \text{if m} = \text{-1} \\ \eta\sqrt{n+1}, & \text{if m} = 1 \end{cases} \tag{3.16}$$

Now we can understand how we can not only couple electronic modes to one another, but also motional levels. Each electronic level has a ladder of harmonic oscillator states on top of it for each motional mode of the crystal. Considering only one mode and a two level electronic system between one of the $S_{1/2}$ Zeeman sublevels and one of the $D_{5/2}$ sublevels, Fig. 3.3 shows how each of these levels can be coupled to one another individually by a laser field detuned from resonance by the trap frequency. Higher order red and blue sidebands also exist, but for a cold ion the coupling between these levels decreases dramatically by factors of $\sqrt{n}\eta$.

Because we can control the ions' motional excitation through laser addressing, we can exploit this to cool the atoms through a process known as resolved sideband cooling. As the trap frequency is much larger than the linewidth of the transitions (about 1 MHz vs. 140 mHz), we can selectively address the red sideband which removes one quantum of motion from the ion. Now in the excited electronic state, the ion can be repumped back into the ground state through the $P_{3/2}$ level which is short lived without changing the motional level (if η is small). This can then be repeated many times, removing quanta until the ion is in the ground state. At that point, from Equation 3.16, one can see the coupling to the laser goes to 0 and the ion remains in that state. In this way, sideband cooling is like optical pumping into the motional ground state. Fig. 3.4 illustrates how the lasers couple each electronic level to move the ions into the ground state, $n = 0$.
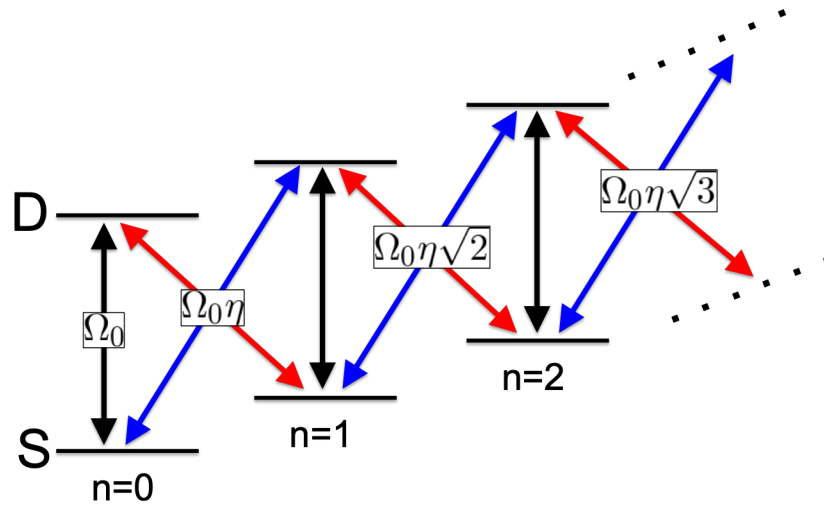
Figure 3.3: Couplings between electronic and motional levels in a calcium ion. Black arrows indicate couplings between transitions of $\Delta n = 0$, red arrows for red sidebands with $\Delta n = -1$, and blue arrows for blue sidebands with $\Delta n = 1$. The relative couplings for each transition are given.
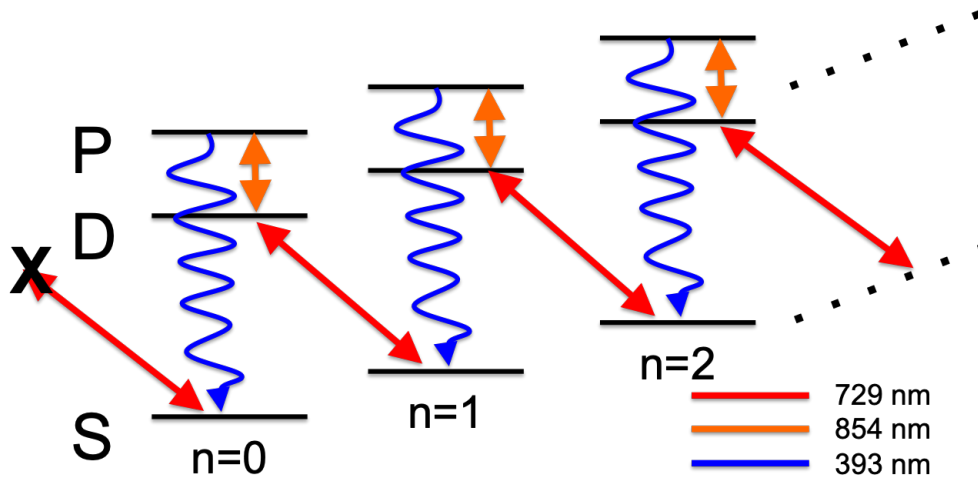
Figure 3.4: Transitions used in sideband cooling. 729 nm coupling laser (red), 854 nm coupling laser (orange) and 393 nm decay path (blue) shown.

When performing sideband cooling, it is important that the Rabi frequency of the 854 nm transition roughly matches that of the 729 nm transition. If the power is too high, the state will be constantly projected into the ground state so no D state population will accumulate. Conversely, if the 854 is too low, the population is not removed efficiently from the D state

without changing the motional state back to its original value.

Sideband cooling can cool one mode of an ion string at a time very near the ground state to temperatures of 10s of uK (here temperature is interpreted in the same way as in the section on Doppler cooling) in a few ms. The main limitation of sideband cooling is off-resonant scattering off the carrier which can remove atoms out of the $n = 0$ manifold though this can be mitigated by limiting the Rabi frequency of the 729 nm laser.

EIT Cooling

Sub-Doppler temperatures can also be achieved through electromagnetically induced transparency (EIT) cooling [15, 16]. EIT cooling in calcium utilizes a coherent superposition of the two Zeeman ground states and one Zeeman level in the $P_{1/2}$ state to create a very narrow feature in the absorption profile of the cooling laser in frequency space which can be used to do very fast, broadband, sub-Doppler cooling.

The relevant energy levels for EIT cooling are shown in Fig. 3.5. A strong, circularly polarized (σ_+) 397 nm beam couples the $S_{-1/2}$ electronic level to the $P_{+1/2}$ level. The linewidth of this transition is large enough that typically this beam would couple both $S_{1/2}$ Zeeman sub-levels to both $P_{1/2}$ Zeeman sub-levels; however, the polarization of the light field excludes transitions other than $\Delta m = 1$ where m is the magnetic quantum number. Therefore, only the two aforementioned levels are coupled. The $S_{1/2}$ sub-level is also coupled to the $P_{1/2}$ sub-level through a weak, linearly polarized (π) 397 nm beam. Like in Doppler cooling, an 866 nm beam is necessary to pump out of the $D_{3/2}$ state but isn't relevant for the EIT cooling dynamics.

The Hamiltonian for such a system can be broken down into two parts. The first is that of the atomic Hamiltonian:

$$H_0 = \begin{bmatrix} 0 & 0 & 0 \\ 0 & \omega_1 & 0 \\ 0 & 0 & \omega_2 \end{bmatrix} \tag{3.17}$$

where ω_i is the energy of the ith electronic energy level labeled in fig 3.5. H_0 has eigenstates

$$\begin{aligned} H_0|S_{-1/2}\rangle &= 0|S_{-1/2}\rangle, \\ H_0|S_{+1/2}\rangle &= \omega_1|S_{+1/2}\rangle, \\ H_0|P_{+1/2}\rangle &= \omega_2|P_{+1/2}\rangle. \end{aligned} \tag{3.18}$$

The second part of the Hamiltonian describes the coupling of the electronic levels to one another with a Rabi frequency Ω mediated by the laser couplings:

$$H_{int} = \frac{1}{2} \begin{bmatrix} 0 & 0 & \Omega_{\sigma_+}e^{i\omega_\sigma t} \\ 0 & 0 & \Omega_\pi e^{i\omega_\pi t} \\ \Omega_{\sigma_+}e^{i\omega_\sigma t} & \Omega_\pi e^{i\omega_\pi t} & 0 \end{bmatrix}. \tag{3.19}$$
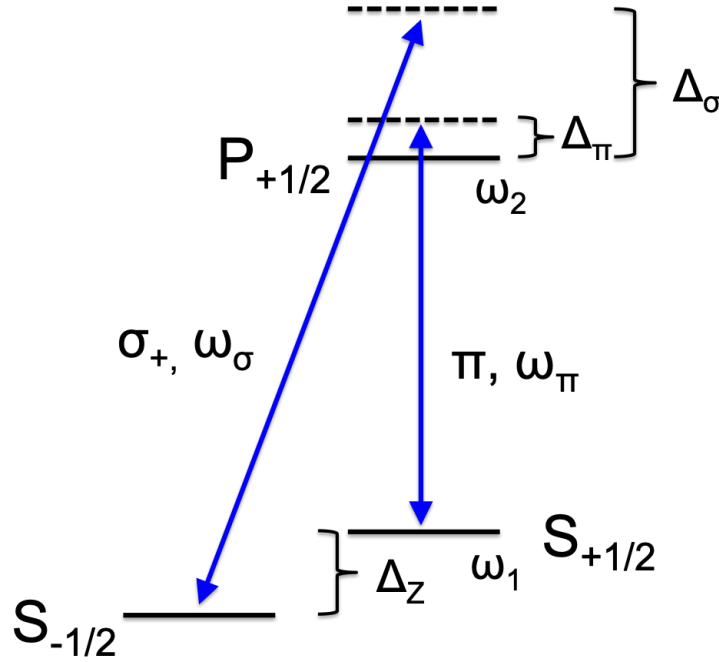
Figure 3.5: Atomic levels participating in EIT cooling with relevant detunings and frequencies labeled.

To transform into the frame of the laser fields, we use the operator

$$U(t) = e^{iH_0 t} = \begin{bmatrix} 1 & 0 & 0 \\ 0 & e^{i(\omega_\sigma - \omega_\pi)t} & 0 \\ 0 & 0 & e^{i\omega_\sigma t} \end{bmatrix}. \tag{3.20}$$

With this we can find the operator $H = H_0 + H_{int}$ in the interaction frame:

$$UHU^\dagger = \frac{1}{2} \begin{bmatrix} 0 & 0 & \Omega_{\sigma_+} \\ 0 & -2(\Delta_\sigma - \Delta_\pi) & \Omega_\pi \\ \Omega_{\sigma_+} & \Omega_\pi & -2\Delta_\sigma \end{bmatrix} \tag{3.21}$$

where $\Delta_\sigma = \omega_\sigma - \omega_2$ and $\Delta_\pi = \omega_\pi - \omega_1$ and is the detuning of each laser from resonance of the level it is coupling. Solving for the eigenfunctions and eigenvalues of this total Hamiltonian, we find

$$\begin{aligned} |a^0\rangle &= \cos\theta|1\rangle - \sin\theta|2\rangle, \\ |a^\pm\rangle &= \sin\theta\sin\phi|1\rangle + \cos\theta\sin\phi|2\rangle \pm \cos\phi|3\rangle, \\ \omega^0 &= 0, \omega^\pm = \frac{1}{2}(\Delta_\sigma \pm \sqrt{\Delta_\sigma^2 + \Omega_\sigma^2 + \Omega_\pi^2}) \end{aligned} \tag{3.22}$$

where θ and ϕ are known as mixing angles and defined as

$$\tan\theta = \frac{\Omega_\sigma}{\Omega_\pi}, \tan\phi = \frac{\sqrt{\Omega_\sigma^2 + \Omega_\pi^2}}{\sqrt{\Omega_\sigma^2 + \Omega_\pi^2 + \Delta_\sigma^2} + \Delta_\sigma}. \tag{3.23}$$

What is interesting about these eigenstates is that if $\Omega_\sigma \gg \Omega_\pi$, then $\theta \to \pi/2$ and $|a^0\rangle \to |2\rangle$. Since $|2\rangle$ and $|3\rangle$ are orthogonal, that means that

$$\langle 3|H|a^0\rangle \approx 0 \tag{3.24}$$

and that the ground state (mostly $S_{+1/2}$ with very little $S_{-1/2}$ character) no longer absorbs and scatters photons off the $P_{+1/2}$ level despite a coupling laser being on. It this way, $|a^0\rangle$ is known as a 'dark state' because it does not interact with the laser field.

We are concerned with this dark state because it is the coupling between $|a^0\rangle$ (which is mostly ground state character) and the excited state that determines the photon scattering rate that can be used for cooling. If there are no photons absorbed, there can be no cooling. If Δ_σ is fixed, we can map out the steady state population of the $P_{+1/2}$ level which is directly related to the scattering rate. This population is given in [17]

$$\rho_{ee} = 8(\Delta_\sigma - \Delta_\pi)^2 \Omega_\sigma^2 \Omega_\pi^2 \Gamma / Z \tag{3.25}$$

where

$$\begin{aligned} Z =& 16\Gamma(\Delta_\sigma - \Delta_\pi)^2 \Omega_\sigma^2 \Omega_\pi^2 + 16\Gamma^3(\Delta_\sigma - \Delta_\pi)^2(\Omega_\sigma^2 + \Omega_\pi^2) \\ &+ 8\Gamma(\Delta_\sigma - \Delta_\pi)^2(\Delta_\sigma^2\Omega_\pi^2 + \Delta_\pi^2\Omega_\sigma^2) - 8\Gamma(\Delta_\sigma - \Delta_\pi)(\Delta_\pi\Omega_\sigma^4 - \Delta_\sigma\Omega_\pi^4) \\ &+ \Gamma(\Omega_\sigma^2 + \Omega_\pi^2)^3 \end{aligned} \tag{3.26}$$

If Δ_σ is large relative to the natural linewidth of the excited state and blue detuned, the scattering rate exhibits a Fano-like resonance around the point where $\Delta_\sigma = \Delta_\pi$. Fig. 3.6 shows the excited state population as a function of the frequency of the linearly polarized 397 nm laser. One can see the broad atomic resonance around 0 detuning with the addition of a Fano-resonance at $\Delta_\sigma = \Delta_\pi$. The plot on the right zooms in on this resonance and shows the placement of the red and blue sidebands during EIT cooling.

For exactly $\Delta_\sigma = \Delta_\pi$, we have a dark resonance which would be experienced by an atom at rest, labeled by the black dashed line in Fig. 3.6 because of our two photon resonance condition. However, hot ions oscillate back and forth at the trap frequency ω_t which allow them to absorb and emit photons at $\pm\omega_t$, as already discussed. With this asymmetric scattering profile, absorption on the red sideband where energy is removed from the system is greatly enhanced while absorption on the carrier and blue sideband are suppressed. The positions of the sidebands for a 1 MHz mode are shown in Fig. 3.6. This imbalance leads to cooling not just at one frequency, but at any frequency where the red sideband is amplified over the blue. Optimal cooling occurs at the trap frequency equal to the induced stark shift from the σ_+ beams, $\delta = \frac{1}{2}(\sqrt{\Omega_\sigma^2 + \Delta_\sigma^2} - |\Delta_\sigma|)$ because it is at this point that transitions between dressed states are resonant when removing one quantum of energy. Additionally,
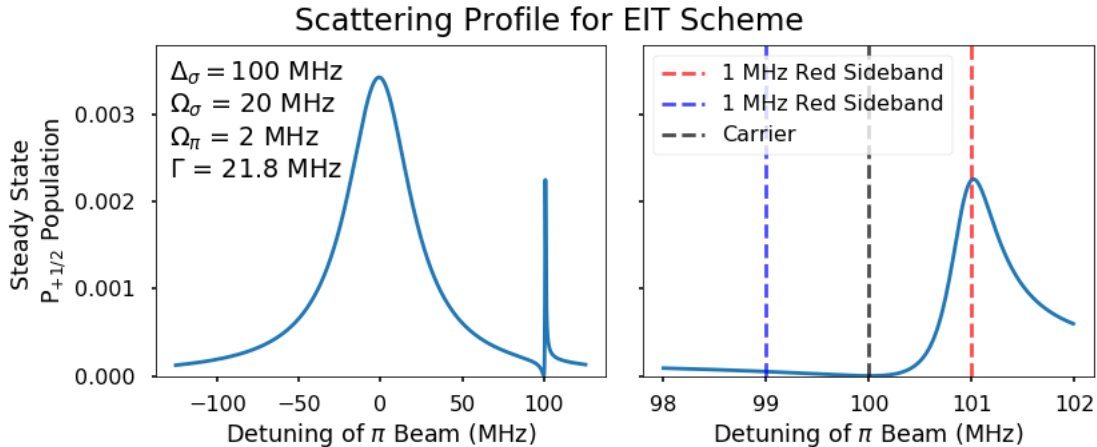
Figure 3.6: (Left: Simulation of $P_{+1/2}$ population as a function of the linear beam detuning for a circularly polarized beam blue detuned 100 MHz from resonance with a Rabi frequency of 20 MHz and a linearly polarized beam with a Rabi frequency of 2 MHz. Right: Enlarged view of the Fano resonance with the dashed lines indicating the placement of motional transitions during EIT cooling.

the rate of EIT cooling is determined by Ω_π which is very fast because of the strong coupling to the $P_{1/2}$ level, but also can go arbitrarily high as long as it is much less than Ω_σ. EIT has been demonstrated in calcium ions and used to cool the radial modes of an 18 ion string to the ground state in 1 ms [18].

Repump Doppler Cooling

As stated in Section 3.3, most trapped ion experiments Doppler cool with only one 397 nm beam propagating parallel to the surface of the trap. However, sometimes the symmetry of a trap necessarily creates a normal mode perpendicular to the surface of the trap. This is a problem because it has been observed that near UV light on surface traps can cause charging and huge fluctuations in the static electric fields at the trapping site [19]. In the experiments described in Chapter 7, we have this exact situation where the vertical mode is uncooled by the horizontal 397 nm laser. In order to perform initial cooling on this mode of motion we perform vertical Doppler cooling with the 866 nm repump laser. Near-IR light does not have the same charging effects as near-UV so it can illuminate the trap safely and since it is part of the same closed system as the 397 nm transition, no additional beams are required. The cooling rate is slower by a factor of about 30 due to the branching ratio and reduced recoil momentum of the 866 nm photons; however, we find this rate to be sufficient to achieve temperatures of a few mK.

When setting the parameters to cooling with a repump laser, one must be concerned with dark resonances described in the previous section. Typically this is not an issue with

Doppler cooling because in order to avoid this effect, the repump laser is blue-detuned from the resonance so as not to interfere with the red-detuned primary laser. However, if we wish to perform cooling with the repump beam, it must necessarily be red-detuned. More specifically, if one wants to achieve cooling with a laser beam, the derivative of the scattering state ($|P\rangle$) population with respect to the laser frequency must be positive [20]. For Doppler cooling in calcium with a repump laser like in our system, that is to say that at the given laser frequency, the derivative of steady state population in the $|P_{1/2}\rangle$ state must be positive with respect to the 397 nm (horizontal) *and* 866 nm (vertical) cooling beam frequencies in order to cool in their respective directions. The left plot in Fig. 3.7 shows the atomic levels and coupling lasers used in Doppler cooling and the detunings between the levels. The right figure shows the steady state population of the $|P_{1/2}\rangle$ state simulated using QuTiP [21, 22] for a range of values for δ_{397} and δ_{866}. One can see the expected dark resonance at $\delta_{397} = \delta_{866}$ across the diagonal of the plot.
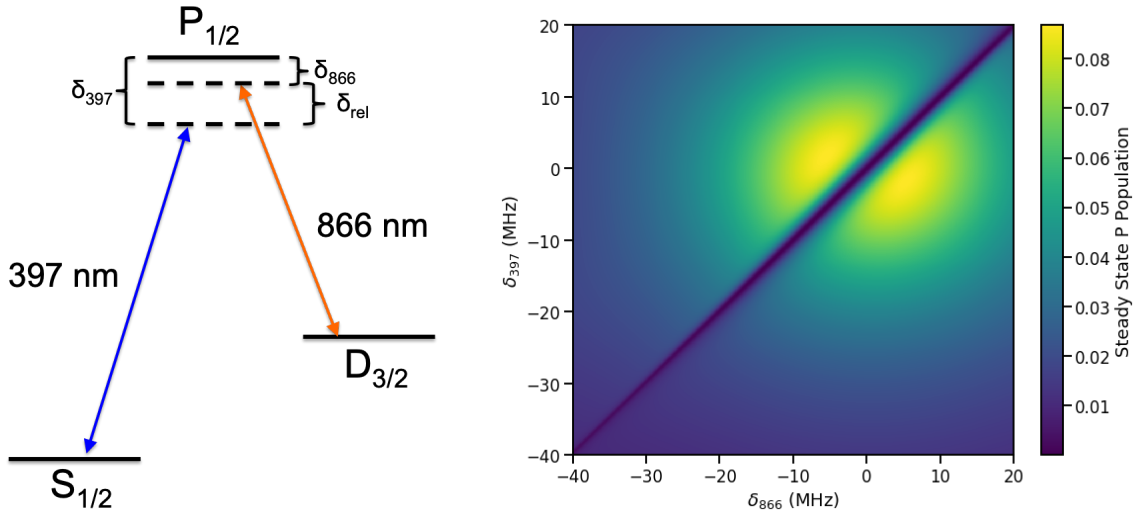
Figure 3.7: Left: Level diagram for repump cooling. Right: Heat map of steady state $|P\rangle$ state population. $\Omega_{397} = 2\pi \times 10$ MHz, $\Omega_{866} = 2\pi \times 3$ MHz.

We can differentiate the right plot of Fig. 3.7 with respect to the 866 nm beam frequency (x-axis) and the 397 nm beam frequency (y-axis) to extract the cooling in the direction of those two beams, vertical and horizontal respectively. The left plot of Fig. 3.8 shows the slope of the steady state $|P\rangle$ population as a function of repump frequency and the right plot the derivative of the excited state with respect to 397 nm beam frequency. Positive regions correspond to cooling and negative regions to heating. Notice along the main feature, which is the dark resonance, cooling properties of the two beams are totally anti-correlated. This is due to the fact that when $\delta_{\text{rel}} = \delta_{397} - \delta_{866}$ is small but non-zero, one laser is blue-detuned from the dark resonance such that it has a positive slope (cooling) and the other will necessarily be red-detuned and have a negative slope (heating). Therefore, as along as

δ_{rel} is smaller than the width of the dark resonance in frequency space, simultaneous cooling with both beams is impossible.
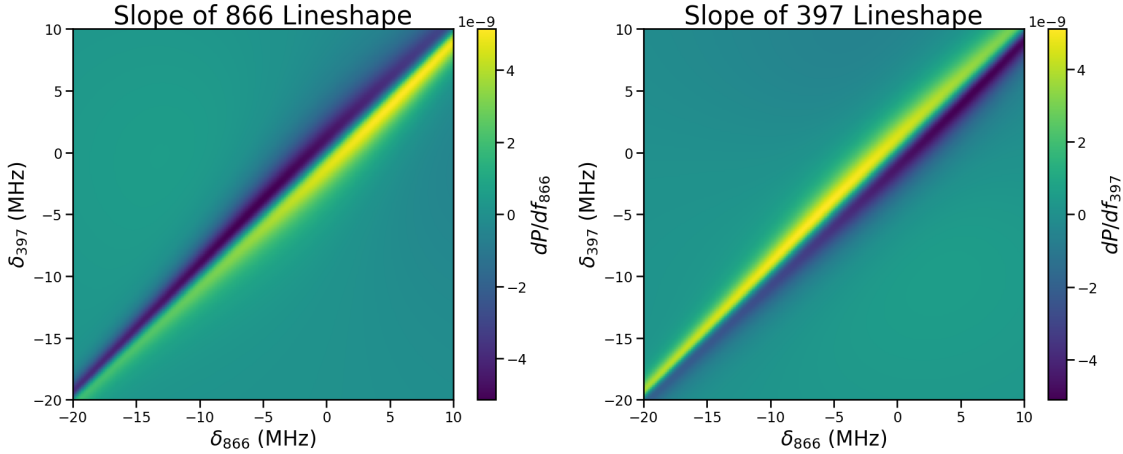
Figure 3.8: Left: Slope of the steady state $|P\rangle$ population as a function of 866 nm beam frequency. Right: Slope of the steady state $|P\rangle$ population as a function of 397 nm beam frequency. $\Omega_{397} = 2\pi \times 10$ MHz, $\Omega_{866} = 2\pi \times 3$ MHz.

In order to achieve cooling in both the vertical and horizontal directions, δ_{rel} must be larger than the size of the dark resonance feature which is related to the Rabi frequency of the two cooling lasers. By applying a mask to the plots in Fig. 3.8 where all points that are ≤ 0 on either plot are set to 0, we can see in Fig. 3.9 that if the the relative detuning of the two beams is large enough but both still overall red-detuned, there is a region where both beams are cooling. By avoiding the dark resonance, the frequency of both lasers sit on the natural lineshape of the transition which is cooling because we are overall red-detuned.

In the level scheme shown in the left of Fig. 3.7, I approximated calcium as a three level system. However, because we have a static magnetic field in our chamber of about 4 G, each atomic level is split into Zeeman sublevels separated by several MHz. Therefore, we have two ground states, two excited $|P\rangle$ states, and four $|D\rangle$ states which combine to give eight dark resonances separated from each other by only a few MHz. However, the intuition described above still holds. Therefore, in order to perform repump Doppler cooling, we must avoid all of these dark resonances. For this we require low power to achieve narrow dark resonances and very precise positioning of δ_{rel}. Fig. 3.10 shows an example of the lineshapes of the 397 nm and 866 nm beams where the two laser frequencies are positioned such that we can achieve cooling in both directions. The red dot indicates the locations at which we must judge the slope of the lineshape. In our system, we do indeed observe that the frequency of the repump beam must be accurately placed relative to the 397 nm beam frequency within 2 MHz but that moving the frequency of the two beams together does not affect the cooling quality.

It is important to note that these effects are present in all systems that implement Doppler cooling with a repump beam. However, the cooling rate from the 397 nm beam is so much
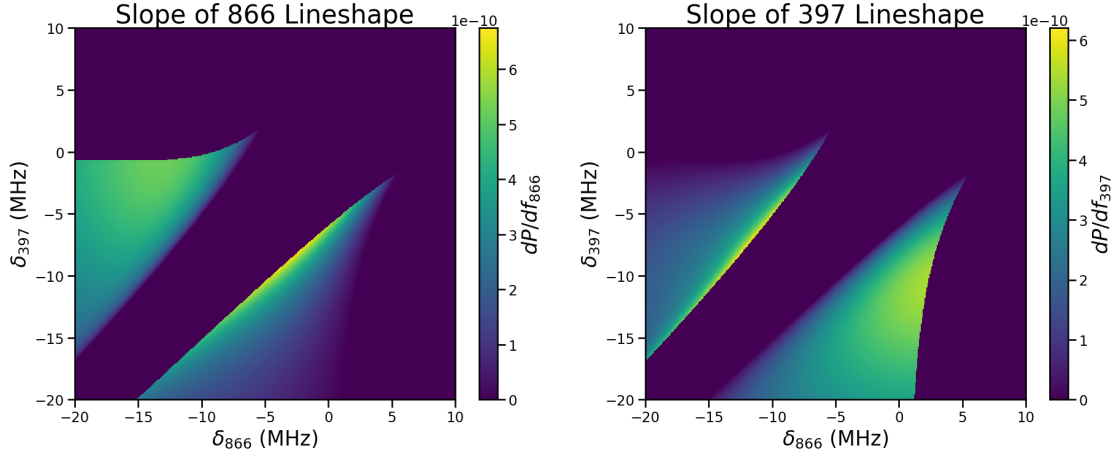
Figure 3.9: Left: Slope of the steady state $|P\rangle$ population as a function of 866 nm beam where only points that are positive in both graphs are non-zero. Right: Slope of the steady state $|P\rangle$ population as a function of 397 nm beam frequency where only points that are positive in both graphs are non-zero. $\Omega_{397} = 2\pi \times 10$ MHz, $\Omega_{866} = 2\pi \times 3$ MHz.
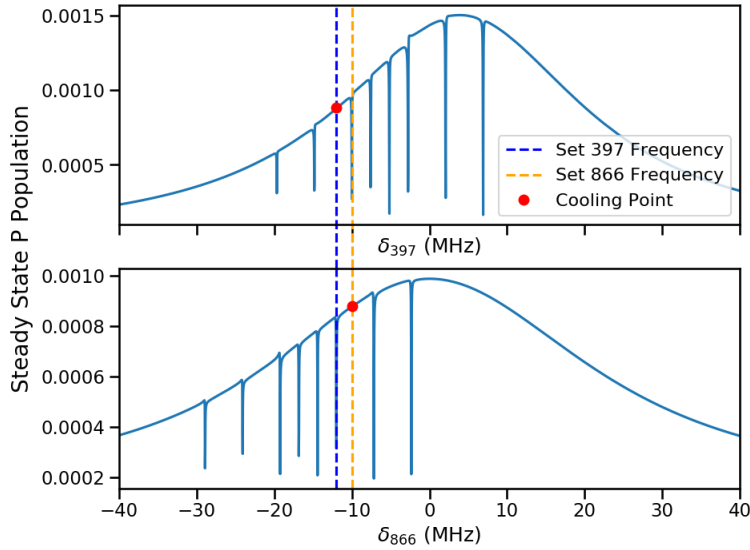
Figure 3.10: Lineshapes for both cooling beams including all eight Zeeman levels at low power. The Rabi frequency of the 397 nm and 866 nm beams are $2\pi \times 1$ MHz and $2\pi \times 0.3$ MHz respectively and detuned $2\pi \times -12$ MHz and $2\pi \times -10$ MHz respectively. The energy of the levels are set such that at zero detuning for both beams the $m_j = -1/2$ levels are all resonant. The red dot marks the point at which the slope determines the cooling limit.

larger than the rate from the 866 nm beam that so long as the 397 nm beam is cooling in the same direction as the repump beam, the effect of the repump will be negligable. It is only

when the 866 nm is the only cooling beam in a certain direction that these effects become relevant. Another important consideration is that because the atom only scatters one vertical 866 nm photon for every 15 horizontal 397 nm photons, the vertical mode will heat through the spontaneous emission of the 397 nm photons but receive no cooling. Therefore each scattered 866 nm photon must overcome the heating of 15 397 nm photons. This might also explain why our system is so sensitive to the precise optimization of the repump frequency.

3.4 State Detection and Qubit Manipulation

An important ability yet to be discussed is the ability to read out the state of the ion. In calcium, we use a technique known as electron shelving [3]. If an ion is in a superposition $\alpha|S\rangle + \beta|D\rangle$, we can collapse the state into one of the states by illuminating the ion with 397 nm light. If the ion is in the S state, it will appear bright, scattering many photons. If it is in the D state, it will remain dark as the D state is dark to 397 nm light as shown in the inset of Fig. 3.11. By collecting the fluorescence and applying a threshold, we can determine which state the ion collapsed to in a few ms as shown in Fig. 3.11. Running this protocol many times (typically 100), we can reconstruct $|\alpha|^2$ and $|\beta|^2$.
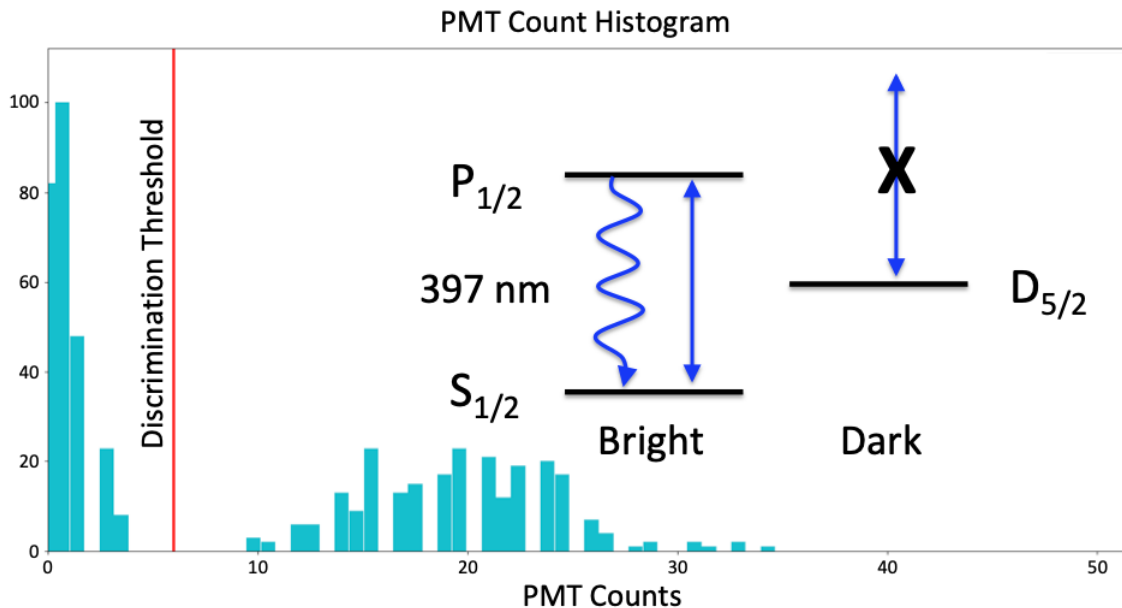
Figure 3.11: Example histogram used for state discrimination, 2 ms exposure time. Threshold shown in red. Inset shows electronic levels participating.

Now that we can projectively detect which state of the ion, we can think about coherent manipulation on the ion. By coupling two S and D Zeeman sub-levels together with a laser field, we can drive population oscillations between the two states known as Rabi

oscillations [23]. Applying this drive until full population transfer is achieved (known as a π pulse), we can coherently move the full population between S and D states. By driving the transition for intermediate times, we create a coherent superposition of the two states we are coupling.

Such oscillations can be used as thermometers on the ion. As shown in Equation 3.16, the Rabi frequency of the carrier depends on the quantum number of the Fock state. But as stated in Section 3.3, if an ion is cooled to a certain temperature, it is actually in a Fock state $|n\rangle$ with a probability determined by the Boltzmann distribution. In this way, when an ion is at a finite temperature, for each instance of the experiment, it has a different Rabi frequency. So, the excited population for a Rabi flop of an ion at finite temperature has the following form

$$P(|D\rangle) = \sum_n e^{-n\hbar\omega_t/k_BT} \sin^2\left(\Omega_0(1-\eta^2 n)t\right)/\sum_{n=0} e^{-n\hbar\omega_t/k_BT} \tag{3.27}$$

where k_B is Boltzmann's constant and T is the temperature of the ion. From this functional form, one can fit a carrier Rabi flop to extract the temperature of an ion.

Our state detection method can measure $|\alpha|^2$ and $|\beta|^2$; however, it cannot measure the phase between them. In order to do this, we must map the phase onto the population. This is realized through a Ramsey experiment. First, a $\pi/2$ pulse is applied to create an even superposition between two states, $\frac{1}{\sqrt{2}}(|S\rangle + e^{i\phi}|D\rangle)$. Letting this state evolve, ϕ increases at a rate determined by the energy difference between the states, $E_{S\to D}/\hbar = \omega_{\text{atom}}$. However, the optical laser light used to excite the qubit will also evolve phase at a similar rate, $E_{729}/\hbar = \omega_L$ where ω_L is the laser frequency. Therefore, after some wait time when a second $\pi/2$ is applied, the total phase acquired by the superposition is $\phi = (\omega_{\text{atom}} - \omega_L)t = \delta t$ where δ is the detuning of the laser from resonance of the optical transition. Given this detuning, δ, the final state of the ion will oscillate between $|S\rangle$ and $|D\rangle$ as a function of wait time with a frequency of δ. If there is any decoherence in the system, this will cause the contrast of the oscillations to decrease as a function time.

Chapter 4

The Ring Trap Platform

Parts of this chapter and the next follow closely a publication [24] co-first authored by myself and Hao-Kun Li of the Zhang group in the Mechanical Engineering department of UC Berkeley. Hao-Kun performed all trap fabrication work presented in these chapters and participated in much of the other work.

4.1 Introduction

Current, the vast majority of Paul traps are designed in linear configurations. Both 3D traps and surface traps are prototypically designed with linear electrodes which create a three dimensional harmonic trapping potential that is much weaker along one axis, creating a cigar shaped trapping region that traps a linear Coulomb crystal. While this design has proven to be a very fruitful testbed for experiments over the last few decades, it has several physical properties built into the system that are unideal for certain applications. Implementing a new trap geometry, such as that of a ring, changes many of these properties opening up likely new classes of experiments.

In this chapter I will begin by describing the new features of a symmetric ring ion trap. I will continue by addressing the primary challenges of creating such a trap in the context of past trap designs from other groups. I will then present our trap design and fabrication considerations. Finally, I will describe the experimental set-up used to trap and probe our new ion ring crystal.

4.2 Properties of an Ion Ring

In this section I will discuss the new properties of ring a trap compared to its linear counterparts as well as give a few examples of experiments where these new properties might be useful.

Ion Spacing

Linear ion chains have several intrinsic properties that make them ill suited for certain experiments. The first such property is the positioning of the ions within the ion string. Along the DC axis of confinement, all ions are pushed towards the center while the mutual repulsion of the coulomb crystal keeps them separated. For each ion, these two forces are balanced at the ion's equilibrium position as shown in Equation 2.2.

From this balance it turns out that ions towards the center of the crystal are more closely spaced than those on the edge. For 15 ions in a 1 MHz trap, Fig. 4.1 shows the equilibrium position of the ions and their relative spacing, smaller in the center and increasing towards the edges.
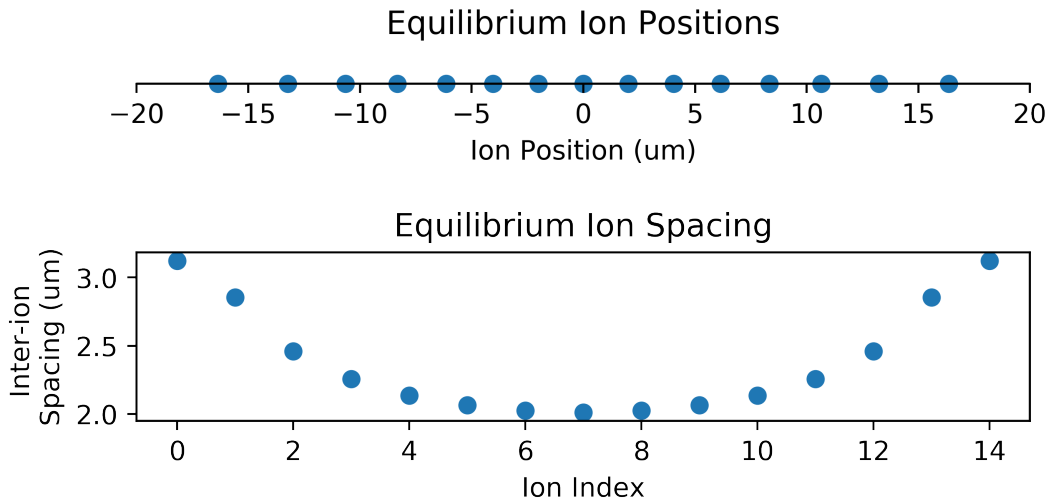
Figure 4.1: Top: Equilibrium ion positions for a linear 15 ion crystal in a Paul trap with an axial trap frequency of 1 MHz. Bottom: Average distance between an ion and its neighbors as a function of ion index for the same conditions.

This uneven spacing can have consequences in laser addressing. For example, current state of the art quantum computing infrastructure includes a multichannel acousto-optic modulator developed by the Monroe group that relies on even ion spacing in a linear ion chain [25]. In order to achieve this, either spectator ions must be loaded on the ends of the chain or segmented DC electrodes used to shape the potential [26].

An ion ring, however, this is achieved natively. Because the ions are held in a toroidal potential, there is no confining potential in the tangential direction and the ions are held in place by the fact that the toroid is a closed system. Therefore, the ions spread around the potential minimum, minimizing only their mutual coulomb repulsion in the absence of any external tangential force. Therefore, their positions are determined by the condition

$$\forall i, \sum_{j \neq i} \frac{e^2(\vec{r_i} - \vec{r_j})}{4\pi\epsilon_0 |\vec{r_i} - \vec{r_j}|^3} = 0. \tag{4.1}$$

For 15 ions in a 94 μm trap, each ion has the same relative spacing to its nearest neighbor as every other ion, as shown in Fig. 4.2. Note, this configuration is not the sole ground state. The ground state can be rotated by any arbitrary angle and still be the lowest energy configuration.
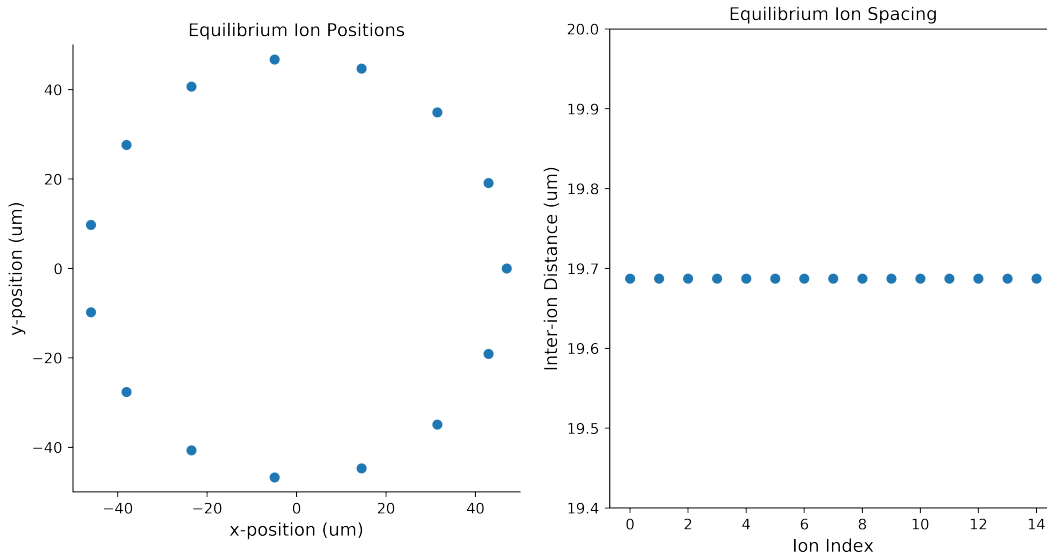
Figure 4.2: Left: One of the spatial ground state configurations for ions held in a toroidal potential. Right: Ion-ion distance in the spatial ground state of the ring.

An example of the application of this property is in experiments studying the Kibble-Zurek mechanism (KZM). The KZM is a model for the behavior observed in spontaneous symmetry-breaking second order phase transitions [27].

In ions, one can observe and study such phase transitions between spatial configurations that obey KZM spontaneous symmetry-breaking. When the axial confinement of a linear ion string is very weak relative to the radial confinement ions form a string on a single line. However, if they axial trap frequency is increased such that the local axial trap frequency (the frequency at which the ion oscillates if all other ions are fixed, dictated by the ion spacing) matches the radial trap frequency, the ions for a zig-zag phase where their spatial positions alternate on either size of the original axis [28, 29] as shown in Fig. 4.3. However, if the ion spacing is uneven, that means the phase transition is artificially broadened across the chain because each sections of the chain will have a different local axial trap frequency. This can obscure the fundamental physics. This issue can be overcome partially by traversing the phase transition very quickly. Even though different sections of the chain undergo the transition at different frequencies, if all points undergo the transition before different regions

of the chain become causally connected (dictated by the vibrational frequencies in the chain), the transition is effectively instantaneous. However, this places a lower speed limit on the experiment. In the ring trap, this is not a problem because the ions are evenly spaced and therefore, the transition occurs everywhere in the ion ring at the same time. Therefore, the transition can be traversed arbitrarily slowly. The allows one to study the homogeneous KZM and potentially quantum KZM transitions which are currently inaccessible in linear traps [29].
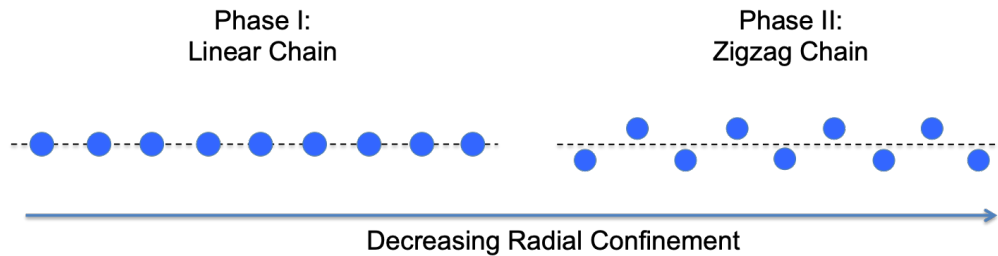
Figure 4.3: Linear chain to zig-zag chain phase transition in an ion string.

Finite System Size/Periodic Boundary Conditions

The second property of linear ion chains is that they are finite-size systems. This has several consequences. Firstly, in enforces a certain type of motional mode structure. As mentioned previously, motional modes are very important in ion chains because the ions' collective motion can be used to exchange information between ions and generate entanglement. As a consequence of the free-end boundary conditions of linear ion chains, each ion participates differently in the motional modes of the crystal. This can be a serious impediment to creating entanglement between two generic ions in long ion chains as one needs to select a motional mode in which both ions strongly participate [30]. Using classical motional mode analysis, we can solve for the motional frequencies of an ion string such as the one shown in Fig. 4.1. The left plot in Fig. 4.4 shows the participation of each ion in each motional mode and one can see that for each mode some ions clearly participate while others remain unaffected.

However, if we now consider a system that has equal ion spacing (such as the ring discussed in the previous subsection) and periodic boundary conditions, we find a different mode structure shown in the right plot of Fig. 4.4. Now, modes come in degenerate pairs and though they have nodes, each mode is shifted relative to its partner such that its nodes are its partners antinodes. Therefore, linear combinations of these pairs can be created such that any given pair of ions would participate equally in that mode. This is a consequence of the global tangential symmetry which allows us to choose any angular orientation around which to expand our motional basis. This pairing of degenerate modes is likely to present a challenge because they can easily hybridize with each other; however, the periodic mode structure could also potentially serve as a tool for experiments that need to generate entanglement across a large number of ions.
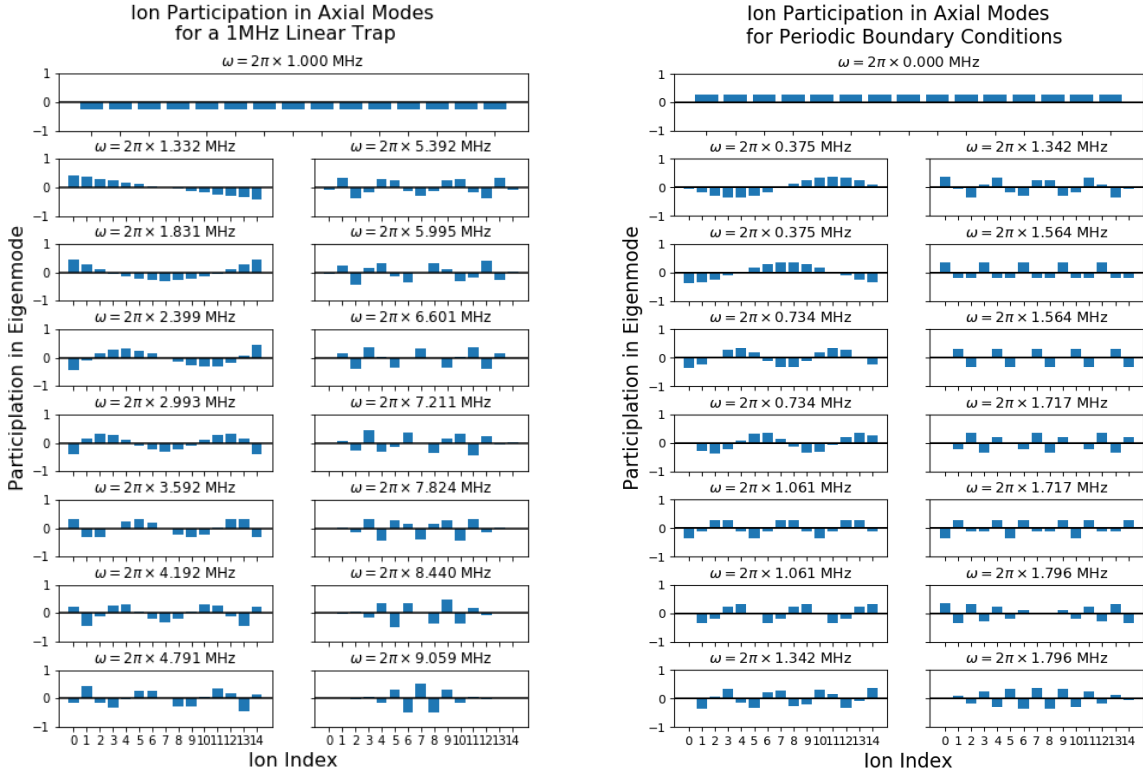
Figure 4.4: Left: Ion participation in the axial vibrational modes of a 15 ion crystal. Right: Ion participation in the axial vibrational modes of a ring trap.

The periodic boundary conditions are also very interesting because they create a closed system. Again in KZM experiments, the transition speed is often bounded from above by the fact that these excitations can escape the crystal structure at the ends of the ion chain [29]. However, in a closed, periodic system such excitations would be topologically trapped within the ion crystal. This would lead to higher fidelity detection but also open up the opportunity for the study of their dynamics in a unique system [31].

Crystal Rigidity

Finally, linear traps are very inflexible geometrically. Physical swap operations have been demonstrated [32], however the platform as a whole is very rigid. The low-frequency axis is almost always oriented in a single direction and ion order is preserved. For most experiments this is a good quality, however for others a more flexible platform would be beneficial.

A ring trap offers two major benefits at first glance. Firstly, the ion crystal is rotationally symmetric. That means it opens up the opportunity to investigate physics where rotations

play a large role such as experiments modeling rotational molecular dynamics [33]. Even more creative applications include using an ion ring trap to emulate an acoustic black hole [34]. In this experiment, one matches the rotational speed of the crystal to the local axial phonon speed. Then, by applying a very small electric field which spatially modulates the speed of sound, one can create an 'acoustic black hole' where phonons created in one region are always attracted to another region of the ring and cannot escape. The proposal suggests this might lead to insights into phenomena such as Hawking radiation.

Secondly, this translational invariance manifests in a 0 frequency mode. Therefore, with a slight perturbation to the ring potential one can imagine creating motional modes of arbitrarily low trap frequency. The trap frequency is often a key parameter in trapped ion experiments and an arbitrarily low trap frequency not limited by the pseudopotential stability criteria could be very useful. Take for example the 'push gate' [35, 36]. This gate relies on the physical displacement of an ion and therefore benefits from very low trap frequencies which enable large translations and subsequently much faster gate times.

4.3 Past Ring Traps

There have been two notable attempts at creating circular Paul traps in the past. The first was done at the University of Munich by Schätz et al. in 2001 [37]. The aim of this trap was to study accelerator beam phases and dynamics. It is made of 3D electrodes similar to a linear trap which are wrapped around into a circular configuration. The ion crystal was rotated at high energies of 1 eV; however, since the trap was aimed at studying ion beam phase transitions for applications in accelerator physics, its properties at typical ion cooling energies, μK-mK, were not explored.

The first attempt at a cold ion ring was done at Sandia National Laboratory by Tabakov et al. [38] in 2015. The trap was made by taking the standard linear surface trap design and extending it in an arc into a full circle and is shown in Fig. 4.5. It has a radius of 1.248 mm and a trapping height of 82 μm. The trapping theory is exactly the same as that of a typical linear surface trap except that there is no designed axial confining potential and instead the ions are held in the trap axially by the fact that it is a closed system. The trap is broken down into several regions that are imaged separately due to its size. The RF electrodes are surrounded by 88 compensation electrodes which are used to tune the local DC potential of the ions and compensate for stray electric fields.

In this trap, Tabakov et al. reported trapping 400 calcium ions. With their compensation electrodes they were able to tune the electric fields at the trapping site and achieve "near-unifrom spacing over 90% of the ring." A stitched image of their ion ring can be seen in the left image of Fig. 4.6 and a graph describing their inter-ion spacing in the right plot of Fig. 4.6, both taken from their publication [38]. The region labeled 'LH' without any ions in Fig. 4.6 is a gap where ions are initially loaded into the trap.

As the first ring trap operating at laser-cooled temperatures, this trap realized several achievements. Firstly, it created a functioning ring trap with microfabrication techniques.
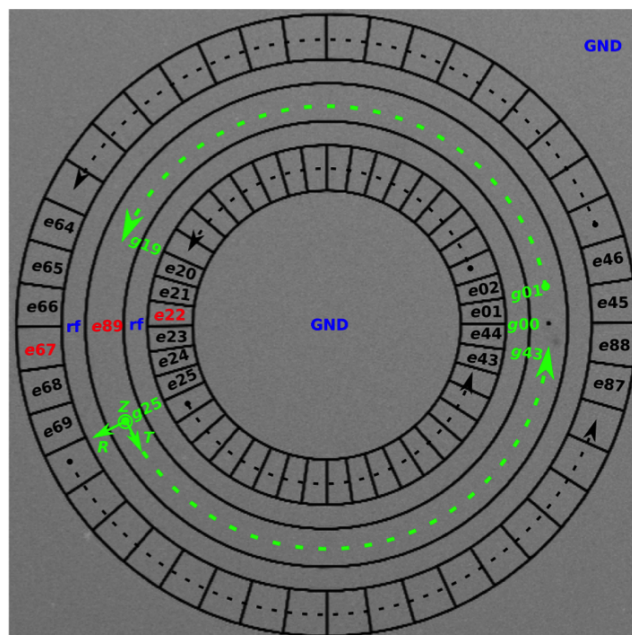
Figure 4.5: Image of the Sandia trap with electrodes labeled from their publication [38].
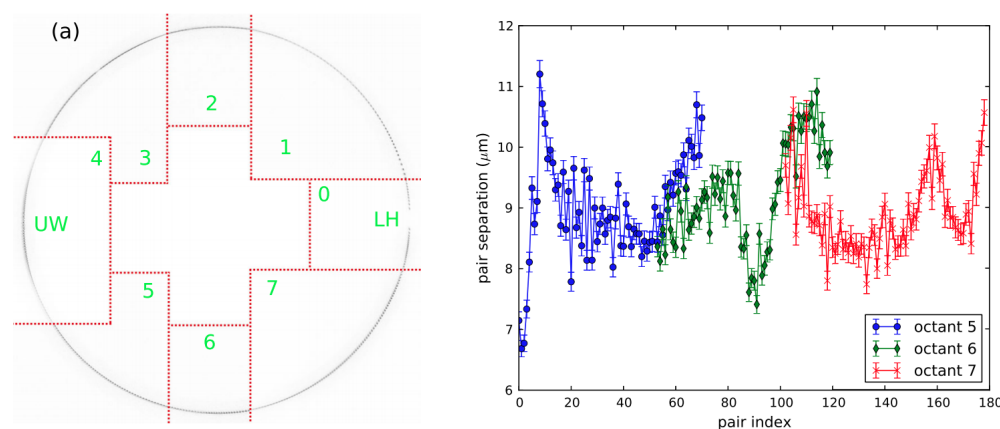
Figure 4.6: Left: Stitched image of the ions in the ring trap from Sandia. Right: Plot of their inter-ion spacing across a portion of the circumference of their ring. Figures from [38].

Secondly, it implemented that trap without the need for explicitly setting an axial confinement potential by making a closed cylindrical system. However, it also fell short of the main objectives for designing a ring trap. A true ring trap should have periodic boundary conditions and rotational invariance. This trap came close to the first property, however the absence of ions at the loading hole means the chain does not have periodic boundary conditions (see 'LH' section of Fig. 4.6). The normal modes of this system would be much closer to those of an extended, bent linear trap than that of a true ring trap as the loading

hole creates a start and end to the crystal. Secondly, the trap is clearly not rotationally invariant. The authors of this paper were able to make great strides towards restoring the symmetry of the trap that is distorted by stray electric fields, however, Fig. 4.6 shows that their efforts still fell short. Over just a small segment of their trap, ion-ion spacings vary from 7 μm to 11 μm. Additionally, though the trap does not have any explicit axial confinement, imperfections in the axial potential give it an effective confinement. This pins the ring into a given orientation, unlike an ideal ring trap which would have no preferred angular orientation.

4.4 Trap Design

The primary design problem of the Sandia trap was an issue of length scales. For a ring trap there are three primary length scales. The first is the inter-ion distance which is the smallest (a few microns). The second is the spatial extent of the ion crystal as a whole. For this we will consider the diameter of the ion crystal. The third is the distance from the ion crystal to the nearest electrodes, which for a surface trap is the trapping height. The ion-electrode distance is important because the closest source of any stray fields present at the trapping site is from voltage imperfections on the trap surface. Therefore, the shortest length scale over which these stray fields vary is on the order of the trap height.

For the Sandia trap, the trap height is smaller than the ring diameter. This means one would expect that they would need to correct for an entirely new set of fields every 82 microns around the trap's circumference to even begin compensation. In their paper, they show that they can make significant improvements to the symmetry of the trap by tuning the compensation electrodes; however, the residual difference in ion-ion spacing and gaps in the ion ring show that the complex set of electric fields produced by the trap over the full extent of the ring was too difficult to overcome.

The ion-electrode distance to diameter ratio for the Sandia trap was 15.2. Improving that ratio would go a long way towards achieving a true, symmetric ring trap, particularly if that aspect ratio could be brought below the critical threshold of one. In this section I will describe such a trap.

Trapping Theory

In order to avoid the complex set of stray fields that limited the Sandia trap, we implement a new trap design that uses interference of RF fields in order to significantly increase the aspect radio described in the previous section. Rather than having a large linear trap slowly bent into a circle, we use a more compact design that not only gives us a smaller ion ring radius, but also a much larger trapping height. A cartoon design (features exaggerated for visualization, not to scale) is shown in Fig. 4.7. Three concentric, circular electrodes are used to create the trapping potential. Such a trap design was first proposed by Clark in

2013 [39] though the authors intention was not to use this design to make ring traps but ideal multipole traps.
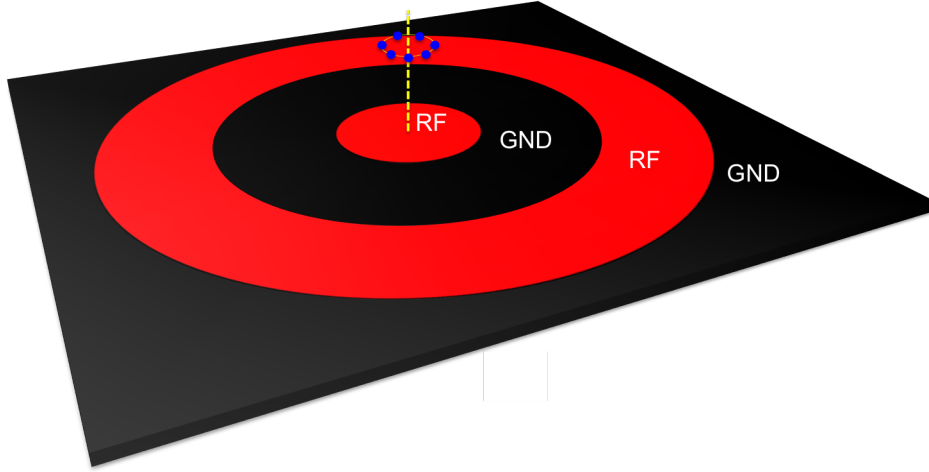
Figure 4.7: Concept for symmetric ring trap. RF electrodes are shown in red, ground in black. Ions trapped above the surface shown in blue.

The potential of such a system can be solved analytically due to its rotational symmetry. In [39], the authors calculate that for a single cylindrically symmetric 2D electrode, the potential it creates above the trapping surface can be written as:

$$\Phi(z, r) = \int_0^\infty J_0(kr)e^{-kz}A(k)\mathrm{d}k \tag{4.2}$$

where $\Phi(z, r)$ is the potential in cylindrical coordinates, J_0 is the Bessel function of zeroth order and $A(k) = V(aJ_1(ka) - bJ_1(kb))$ where V is the voltage applied to the electrode, a and b are the inner and outer radii of the electrode respectively, and J_1 is a Bessel function of first order. Summing this potential over all circular electrodes yields a potential which one can plug into the pseudopotential equations outlined in Section 2.1 and solve for the effective potential in which the ion moves.

In our design, the inner-most electrode is a circle of radius 125 μm. The next electrode has an outer radius of 600 μm and final electrode an outer radius of 1100 μm. The inner and outer most electrodes have an in-phase RF signal applied to them while the remaining electrode is grounded. By numerically solving the integral given in Equation 4.2, it is found that this design produces a pseudopotential with a toroidal RF null with a diameter of 94.6 μm above the trap surface at a height of 385 μm where the ions can be held [40]. This creates a ring diameter to ion-electrode distance ratio of 0.228, 66.8x better than that of Sandia. Fig. 4.8 shows how the cross-section of these two traps to compare to scale.

It is the compact nature of these trap electrodes gives the trapping potential its very low aspect ratio. Consider the instantaneous electric fields produced by this trap shown in a cross-section in Fig. 4.9. If this were a typical linear trap (or a trap bent so gently it was
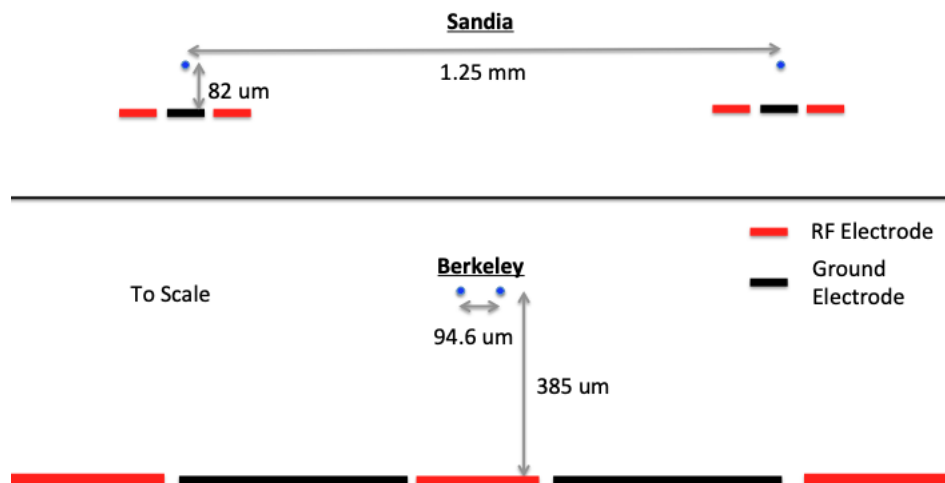
Figure 4.8: Cartoon, to-scale, cross-sections of the Sandia (top) and Berkeley (bottom) traps.

locally linear), the RF trapping field at the ion would be totally sourced by the potential on two RF electrodes on either side of a ground electrode, the right-most three electrodes in Fig. 4.9 for example. Such a configuration results in a trapping point labelled as point A in Fig. 4.9.
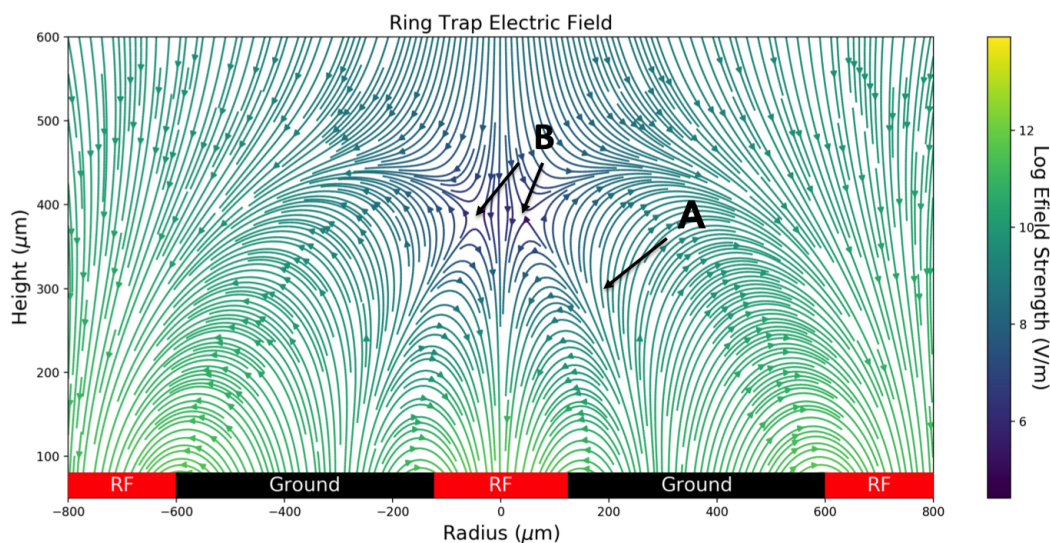
Figure 4.9: Cross-section of the instantaneous electric fields produced by the Berkeley ring trap with the electrodes labeled at the bottom. Point A labels the trapping point if one only considers linear extensions of the three right-most electrodes (The far right electrode extends off the plot to a radius of 1100 μm which is why point A is not centered over the ground electrode). Point B labels the trapping points when considering all electrodes.

However, when the center electrode is shrunk down and fields from opposite sides of the circle begin to influence the old trapping location, what was the original trapping location is no longer an RF null. Instead, the RF is formed at higher location with a much smaller radius, point B. The interference of the two sides of the trap create a very small ring at a very high trapping height, precisely what we were trying achieve with this design.

Typical parameters for trap operation is a 5.8 MHz drive signal applied at 200 V amplitude. These parameters are chosen in order to attain strong enough trap frequencies and trap depth in order to confine the ring. The toroidal potential creates relatively modest trap frequencies for a given amount of voltage because of the field interference and the partial cancelation of the RF fields. Fig. 4.10 shows a cross-section of the pseudopotential of the ring. On the bottom, a slice of the potential at the trapping height as a function of radius is plotted. One can see that for a 200 V applied RF signal, the height of the central bump in the potential which enforces the ring structure is only 0.7 meV. At these parameters, the ring has radial and vertical trap frequencies of 395 kHz. Table 4.1 shows the trap parameters our simulations predict for the given operating parameters.
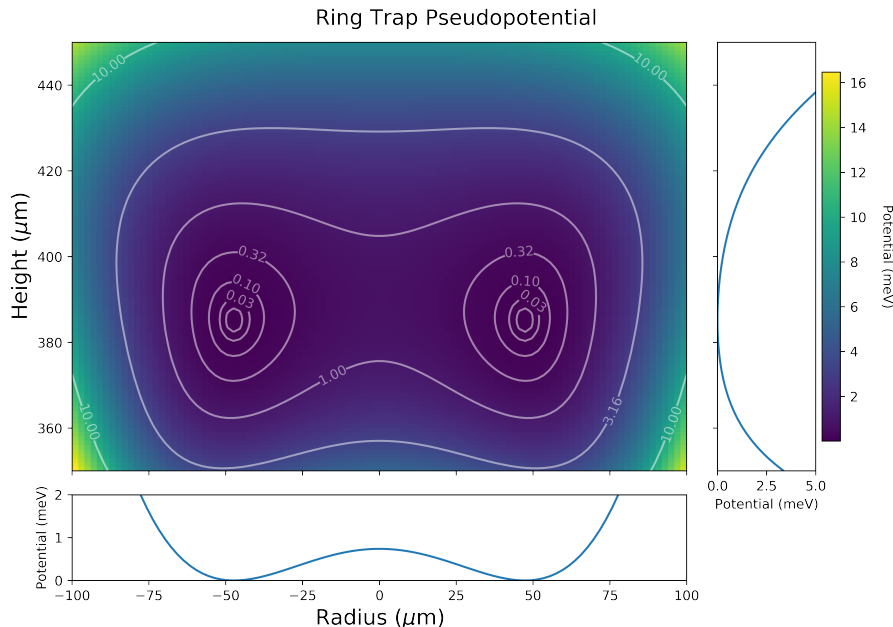
Figure 4.10: Pseudopotential created by applying 200 V to the RF electrodes of the ring trap at 5.8MHz. The plots on the edges show cross-sections of the potential at the trapping height and radius respectively.

The trap also consists of eight electrodes surrounding the outermost RF electrode to which static voltages can be applied to control electric fields at the trapping site. Each electrode takes up $\pi/4$ radians of angle and extends from a radius of 1100 μm to 3000 μm. With these dimensions, each electrode can supply a few V/m of electric field at the trapping site and all eight in conjunction give enough degrees of freedom to independently control all three

Property	Value
Drive Frequency	5.8 MHz
RF Voltage	200 V
Trap Depth	456 meV
Potential at $r = 0$	0.7 meV
Radial Trap Frequency	396 kHz
Trap Height	385 μm
Ring Radius	47.3 μm

Table 4.1: Table of experimental operating values.

electric field dipoles, E_x, E_y, and E_z along with the two in plane quadrupoles $U1$, (shape of $x^2 - y^2$), and $U3$, (xy). We cannot independently control the other three quadrupoles due to our cylindrical symmetry. In the future, more DC electrodes at a different radius would remedy this.

4.5   Trap Fabrication

Silicon Trap

The fabrication of the ring trap required many unique considerations. Firstly, because the trap would require relatively large voltages to achieve secular frequencies comparable to those found in other traps, we aimed to make it tolerate high voltages up to 1 kV. Secondly, the desire to have perfect cylindrical symmetry creates an issue of how to apply voltage to our electrodes. Typically, small wire bonds connect an electrical breakout board to small pad electrodes on the edge of the trap itself that are routed on the trap. This ensures that any fields created by the bonding wire are far away from the trapping site and therefore do not affect the trapping region. This is a problem for the ring trap on two fronts. Firstly, the concentric style of the electrodes means that the electrode cannot be extended far away from the trapping region in a simple 2D geometry. Secondly, any additional routing of the electrode would necessarily break the cylindrical symmetry which this trap is designed to possess.

For this reason, it was decided that the trap would be fabricated out of boron-doped silicon rather than our typical metal-coated glass. Silicon presents a number of advantages over metal coated glass. Silicon fabrication techniques are very advanced due to its use in the electronics industry [41]. Additionally, boron-doped silicon is conductive and allows us to make electrodes which have a structure that is not reliant on a substrate for support [42]. This is critical for applying the voltage to concentric electrodes.

In our trap, boron-doped silicon is anodically bonded to a borofloat glass substrate. A false color image of the surface trap is shown in Fig. 4.11. In reality the trap is black. The

gaps between the electrodes are formed using photolithography followed by deep dry etching of the silicon. The trenches are 25 µm wide with the exception of the innermost trench between the center electrode and the next which is only 15 µm. The trenches themselves are over 200 µm deep ensuring that the ion is effectively shielded from the non-conductive glass substrate. The full fabrication process is discussed in our publication [24].
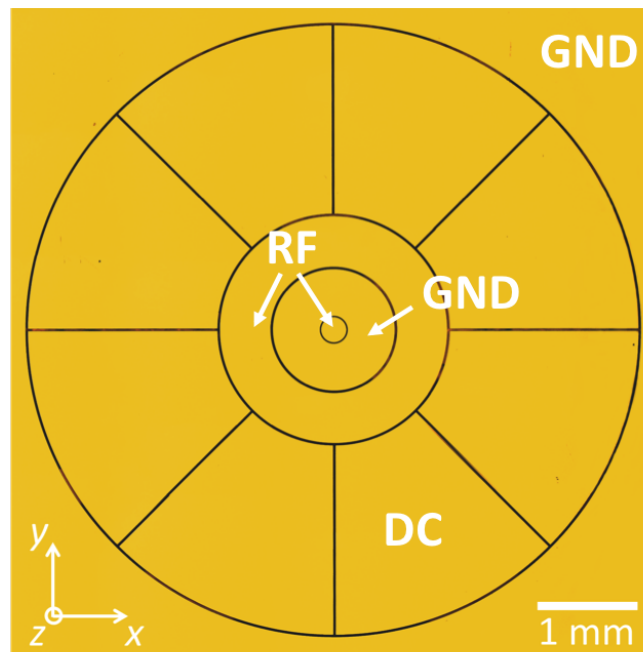
Figure 4.11: False color microscope image of the final trap. Electrodes are labeled by their function. Image adapted from figure in Li et al. [24]

Note: In our main publication [24] and the original fabrication, we had a thin silver layer on top of the silicon to help with potential noisy oxide layers on the surface of the silicon. In later instances of the trap, we found this layer to be unnecessary and it was not included.

High Voltage Tolerance

As stated above, one of the design objectives for this trap was high voltage tolerance. In order to run certain experiments, high frequency confinement is desirable [1, 40]. Unfortunately, in order to obtain a trap frequency of 2 MHz, we need over 1 kV of applied RF. This is of concern because surface traps are susceptible to arcing across the substrate, effectively shorting electrodes together [43]. For shorter path lengths across insulating material (not vacuum) between conducting electrodes, the breakdown voltage decreases. In typical surface traps fabricated with evaporated metal on glass slides, the path length is the gap size, typically 10 µm, plus twice the depth of the trenches between electrodes, typically 100 µm. However for the ring trap, the conducting electrodes extend all the way to a flat glass slide,

giving it a path length of only the gap size and a very short arc path across the surface of the glass substrate between electrodes. In order to overcome this problem, we do a Hydrofluoric acid etch through the trenches which eats away at the glass substrate and increases the path length for potential arcs [43]. Fig. 4.12 shows a cross-section of the fabricated trap where the trench separating the electrodes is visible along with the area etched out for high voltage tolerance.
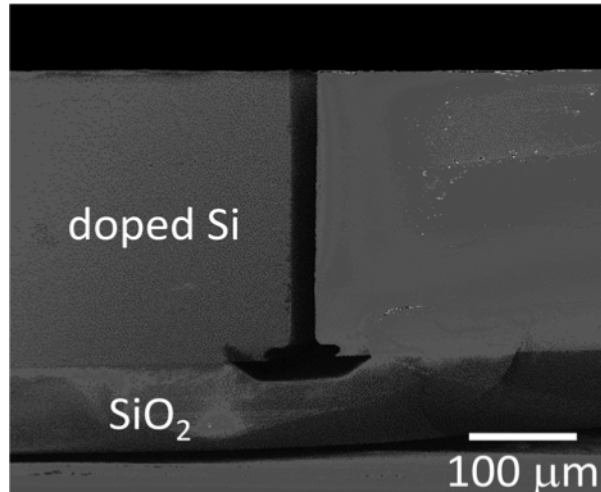
Figure 4.12: Cross-section of the fabricated trap. Image adapted from [24]

When installing the trap, we also performed high-voltage conditioning [44] by increasing the DC current in small steps and letting the trap sit at that voltage before increasing the voltage further. If instead we apply a large voltage immediately, we find the electrodes short to one another at only a few hundred volts. We measure the DC current flowing across the glass substrate by applying a voltage to the electrode then measuring in series the voltage drop over a 1 MΩ resistor. Modeling the gap between the electrodes as a very high impedance resistor, we monitor the resistance of the trap as we turn up the voltage by assuming $R_{\mathrm{trap}} = \frac{V_{\mathrm{meas}}}{V_{HV}} R_{\mathrm{meas}}$. As the voltage across the trap is increased, the voltage across the resistor increases as well; beginning around 250V applied, the measured voltage will begin to spike occasionally for a second or two to up to 10x the usual voltage. As the applied voltage continues to increase, the spikes increase in frequency. However, we find that if we leave DC on for several minutes, these spikes reduce in frequency substantially and eventually go away. Ultimately, after successive 50 V increases and $\approx$ 10 min cures, the trap was found to have 1.2 kV of DC tolerance.

Vias and Mounting

The final feature of our trap fabrication is the introduction of vias. As discussed above, we cannot apply voltages to our electrodes on the trap surface without disturbing the cylindrical

symmetry of the system. Therefore, in order to keep the potential above the trap unperturbed, we apply voltages to the trap electrodes from below utilizing vias [45]. Below each electrode, a hydrofluoric acid (HF) etch is performed on the underside of the glass substrate in a circular pattern. This creates a conical bore down to the silicon electrodes. The right plot in Fig. 4.13 shows an atomic force microscopy (AFM) scan over two vias. The sloped areas are indicative of the HF etch and the flat area at the center shows we have reached bare silicon. Once bare silicon is exposed, the whole via is coated with a layer of gold which extends to a pad structure on the back side of the trap. This is shown in the right image of Fig. 4.13. The large gold pads shown are the contacts which will attach to the chip carrier breakout boards. The black circles are the vias to each electrodes. Despite being black, they are coated in gold. Their appearance is due to the light not being reflected back into the microscope due to their sloped walls.
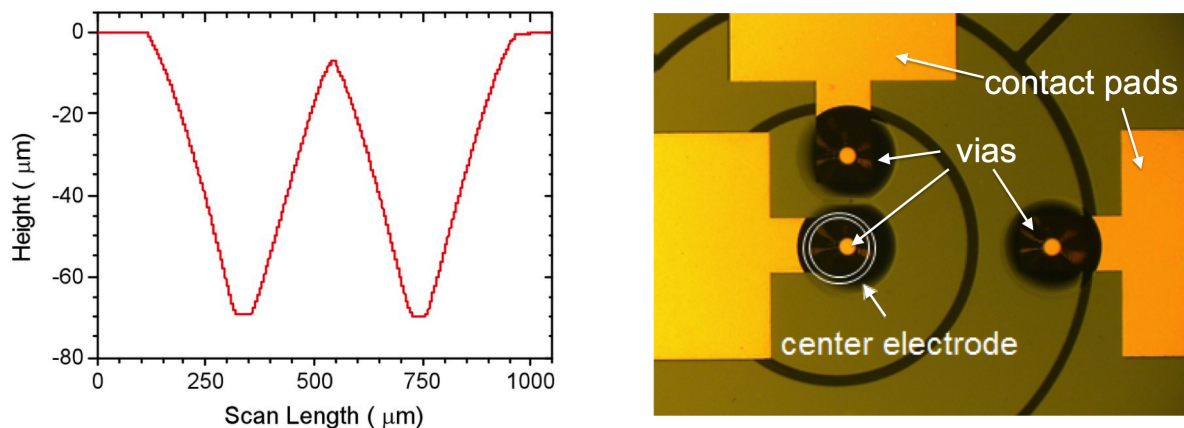
Figure 4.13: Left: AFM scan over two vias on the back side of the trap. Right: Optical image of the back side of the trap centered around the three RF electrodes.

Fig. 4.14 shows a cartoon cross-section of the trap which illustrates all of the layers of the trap and how they fit together.

Vias pose an additional problem when it comes to mounting the trap on a chip carrier. A solid electrical and mechanical connection needs to be made between the trap chip and the breakout board on the reverse side of the trap. We have made this connection in two ways both of which will be detailed here.

Solder Paste Connection

The original connection method was done by applying a small bead of UHV compatible, lead-free solder paste to the pad for each electrode on the backside of the trap then, resting it on top of the chip carrier. After heating to the manufacturer recommended temperature of 200 C for two minutes, the chip had mechanically bonded to the carrier.
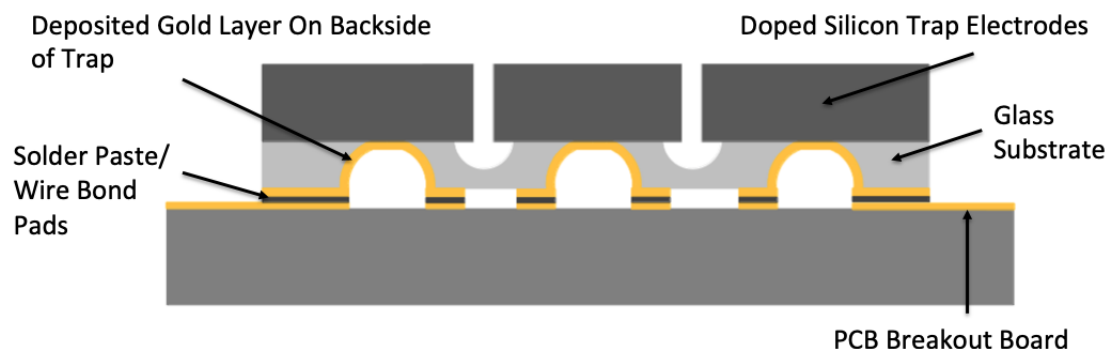
Figure 4.14: Cartoon cross-section of the trap construction.

The electrical connection was tested measuring the resistance between the breakout board and the top side of the trap. In order not to damage the top side of the trap, we made the connection by touching the surface of the trap with a small piece of bonding wire brushed over the surface. Silicon in atmosphere forms a small oxide layer which might give the impression that the electrodes were not connected on the backside; however, with about 24 V of potential across the oxide layer, it appears as a short. Therefore, ultimately we measure the voltage drop over a resistor placed in series with the electrode which is 0 if the trap is not connected but 24 V if the circuit is closed by our solder connection on the backside. By verifying this connection on all 11 electrodes, we confirm the trap is electrically connected.

This is how the trap mounting was done for all experiments through our 2017 publication [24]. However, shortly after collecting all the data, the trap began to behave erratically. After roughly 30 minutes of trapping, all ions would be lost and reloading would be impossible unless the RF was turned off for about 10 minutes. This problem worsened until about six months after original trapping after which we could not trap at all.

Upon inspection of the trap after removal, we found that the small solder beads present within the solder paste had never properly melted. Our mechanical connection was likely from the evaporation of the flux within the paste which had a slight adhesive property and the electrical connection was just a poor contact connection. After some time, it is possible that the connection worsened to the point where slight thermal stresses from applying RF would cause the trap to deform and disconnect electrodes that would reconnect as the trap re-equilibrated thermally.

When trying to install the same type of trap again, we found that the paste required 400 C for 4 min to fully melt. At that temperature the chip carrier and the points at which it was connected to the gold pads on the backside of the trap were burnt and destroyed (Fig. 4.15), making this an unviable method of mounting the trap.
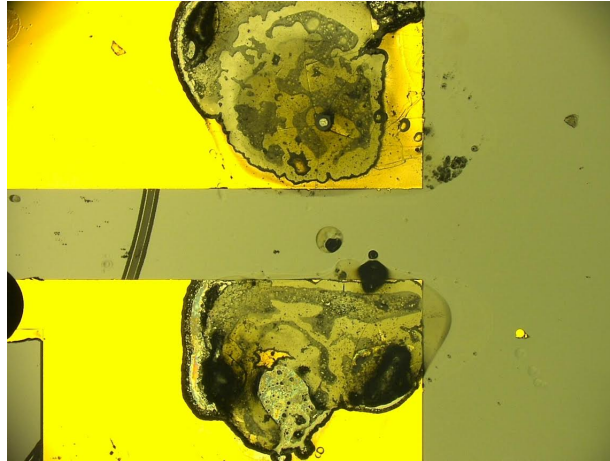
Figure 4.15: Optical image of the bonding pads on the back side of the trap after melting the solder paste.

Epoxy and Wire Bond Spring Pad

As a substitute for bonding with solder paste, the connection is now made with a wire bond spring pad. On each pad on the backside of the trap, five wire bonds are attached to the pad on both ends such that they have a slight bend. Then five more wires are attached perpendicularly in a criss-cross pattern to create a spring pad as shown if Fig. 4.16 that cannot lay flat. Each electrode has a wire-bond pad like the one shown attached to its corresponding pad on the back side of the trap. When pressure is applied to the trap, the pad is compressed as it makes contact with the chip carrier and forms a durable electrical connection. Initially this pressure is applied by the small homemade teflon piece shown in Fig. 4.17. The hole in the center allows us to pressure the trap without potentially damaging the sensitive electrodes. Additionally, the small cut outs expose the corners of the trap to which we apply vacuum safe epoxy (EPO-TEK 353ND) which holds the tension once the teflon is removed. The epoxy is heat cured and required 160 C for 1 hour to fully set. This configuration was used for all experiments mentioned in this thesis after Chapter 5 and currently has been stable for the last 2.5 years.

Through the course of developing this method, we found that occasionally the wire bond pad would not create a connection (though when a connection was made it was permanent). When this happened, we wanted to recover both the trap and the chip carrier as they are both very valuable pieces. In order to achieve this, we found that a 24 hour soak in dichloromethane was very effective at removing the trap from the chip carrier and did no visible damage to the trap. That being said, we never attempted to trap with a chip that had been treated but we have no reason to believe this would not work.
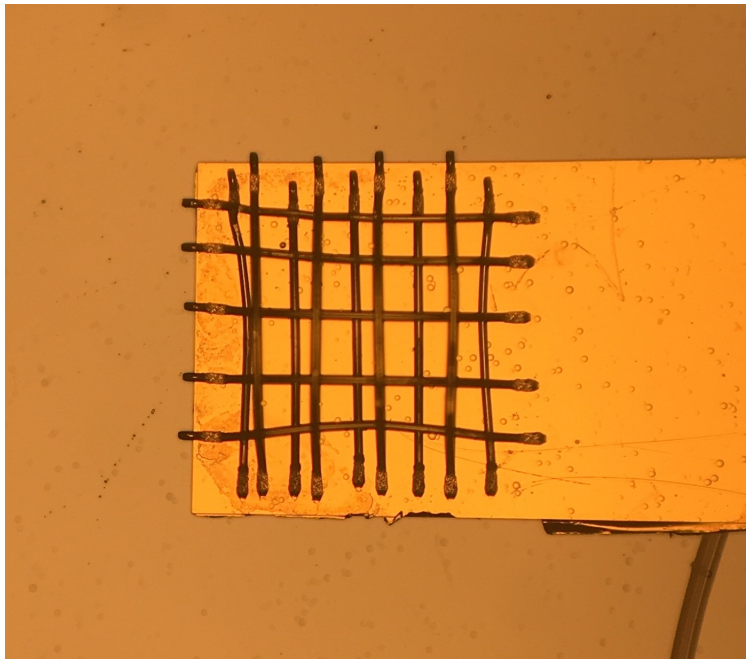
Figure 4.16: Wire bond pad used to create connection between the underside of the trap and the breakout board.
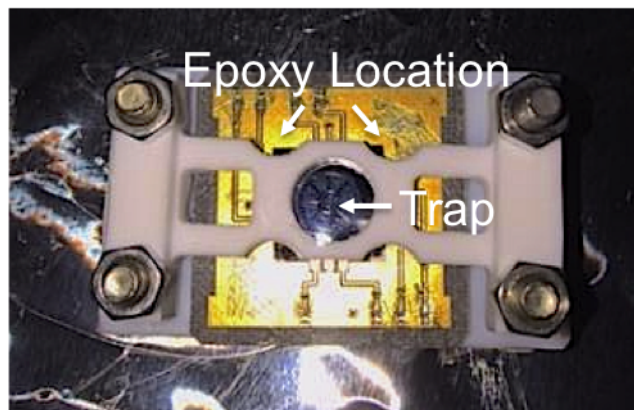
Figure 4.17: Teflon holder which applies pressure to the trap (black) while applying epoxy to the breakout board.

4.6   Experimental Setup

The trap is mounted by the methods discussed in the previous section upon a PCB of gold plated Rogers material printed by Beta Layout. This board is then attached to a socket to which both the RF and DC voltages are routed. The DC voltages are sourced by 14 bit digital-to-analog converters filtered by 100 kHz low pass RC filters at the chamber entrance. The PCB itself has a 10 nF capacitor connecting each electrode to ground directly before the

electrode in order to have filtering as close to the trap as possible. The PCB routes a single RF signal to both the the inner most circular electrode to the outermost circular electrode with the exact same path length in order to ensure that the two electrodes are driven with exactly the same phase of RF. Any mismatch would induce micromotion that we would be unable to compensate.

The RF is applied through a toroidal transformer placed in parallel with the capacitance of the trap to create a resonator that is impedance matched to the trap at 5.8 MHz. The toroidal transformer was chosen as opposed to our typical helical resonators because of our need for a very low drive frequency. The transformer is made from copper wire wrapped around a 2 inch diameter ferrite core with a single loop input and a 32 loop output. Placed in parallel with the 22 pF load present between the RF feedthrough and ground, this impedance matches well as a 50 ohm load at the resonant drive frequency. Fig. 4.18 shows the schematic of the resonator circuit. In order to apply 200 V to the trap, 100 mW forward power is delivered to the trap.
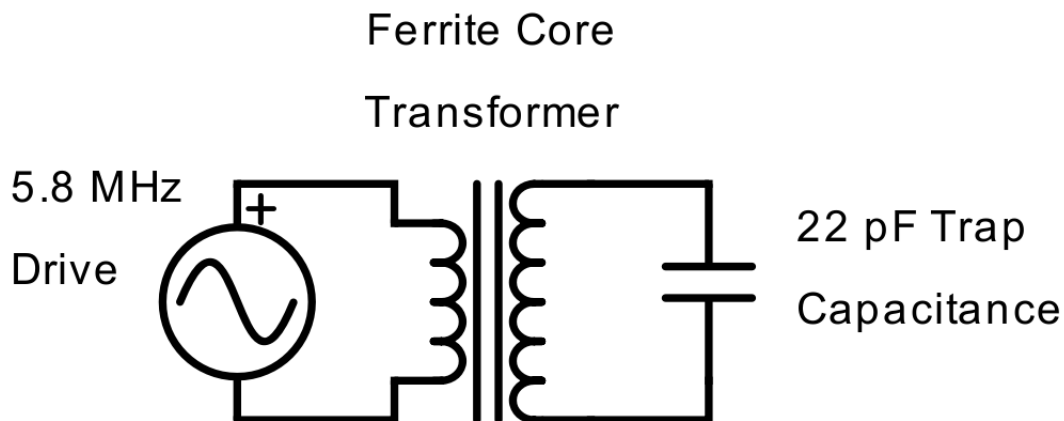
Figure 4.18: Schematic for the toroidal resonator used to drive the ring trap at 5.8 MHz.

Once trapped, the ions are manipulated by beams focused on the trapping region traveling parallel to the surface of the trap. The 397 nm and 866 nm beams are broadened such that they have a waist of about 70 μm such that they at least partially illuminate the entire ring. We must be careful to center the 397 nm beam in order to not apply a significant torque on the ions from the radiation pressure of the beam. 729 nm spectroscopy requires more power and thus the laser is focused down to illuminate only a portion of the ring. Additionally, focusing on only a portion of the ring makes the spectrum easier to interpret. Fig. 4.19 shows the positioning of the lasers on the trap.

Fluorescence from the ions is collected through a custom, home-built objective oriented perpendicular to the ring plane so as to resolve the full trapping region. The objective was designed within the lab based on a paper that describes how to make custom objectives based on stock parts [46]. The objective is 2 inches in diameter and optimized to gather
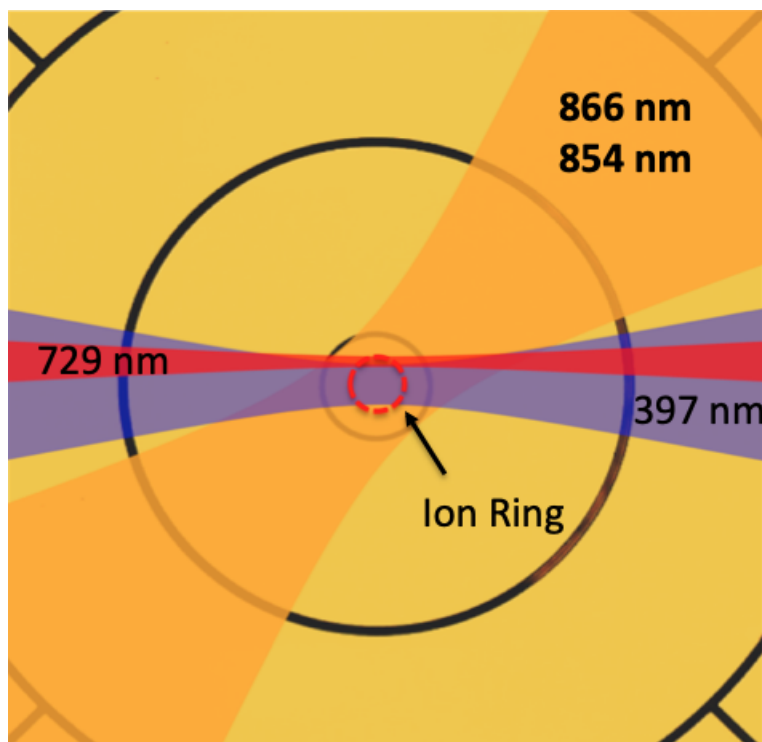
Figure 4.19: Laser configuration used to manipulate the ion ring.

397 nm light at a working distance of 6 cm to be focused on a plane at 70 cm. The objective has a numerical aperture of 0.25. Optimization was done with Zeemax software and the final design and lenses chosen are shown in Fig. 4.20. The lenses were spaced using machined plastic rings that contacted the lenses 2 mm from the edge radius. The spacing quoted in Fig. 4.20 is the spacing at the contact point. The final cost of all lenses was less than $200. The viewport through which the ions are imaged is coated with Indium Tin Oxide, a coating that is conductive and grounded to the viewport itself. This is to ensure the charges that might gather on the surface of the insulating glass are efficiently dispersed.

After collection through the objective, the fluorescence is imaged on a focal plane 70 cm away. A slit at the focal plane allowed for readout of only portions of the ring if required. The beam was then allowed to re-expand for a few centimeters until it was refocused and then split equally into a Andor Luca EMCCD camera and a PMT, both located at the second focal plane. Fig. 4.21 shows a schematic of the full system.
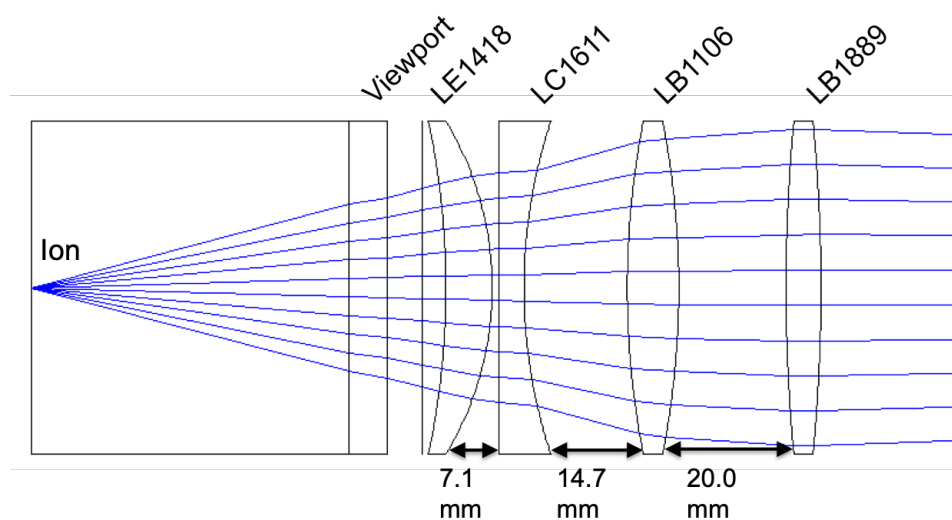
Figure 4.20: Homemade objective used in this work. All lenses are stock Thorlabs lenses. The objective was designed to have a tight focus for 397 nm light at a working distance of 6 cm.
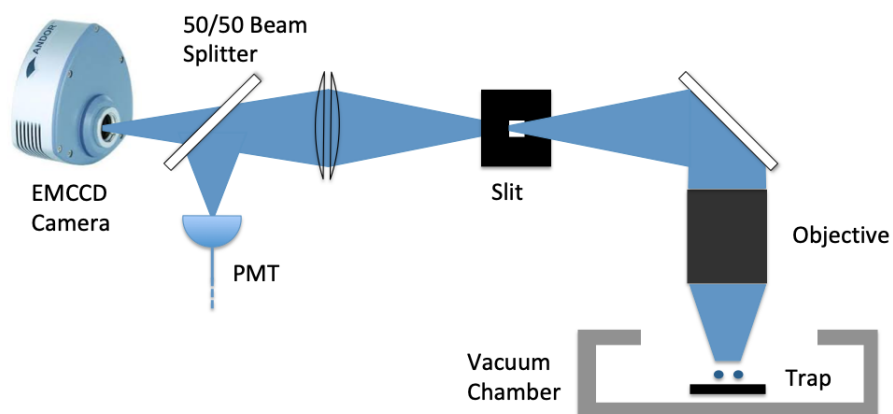
Figure 4.21: Fluorescence gathering schematic.

Chapter 5

Characterizing the Symmetry of the Ring

In this chapter I present the characterization of the ion ring once loaded into the trap. I begin by defining how we can quantify symmetry in the context of a ring trap. Then I argue how we could expect symmetry-breaking fields to impact our ion ring and continue to describe how we can measure if that expectation if valid. Finally, I discuss the behavior of the ion ring when its symmetry has been restored to the best of our ability.

5.1   Quantifying the Symmetry of the Ring

As argued in the Section 4.4, because of the large trapping height to radius ratio, we expect this trap design to posses a higher degree of symmetry than previous realizations of ring traps. Specifically, one expects the smallest length scales at which the fields above a surface can vary goes as the distance from the surface. By that token, it is expected that the fields sourced from any point on this trap surface will change on a length scale of about 400 μm at the trap height while the ring itself is only 94 μm in diameter. Therefore, it is expected that one can describe the electric fields present across the entirety of the trapping region in a single multipole expansion around the center of the ring. With the eight DC electrodes on the trap, one can correct for both stray dipole and stray quadrupole fields present at the trapping site. If our multipole expansion is sufficient to describe the fields across the extent of the ring, we should be able to correct for those fields and restore the symmetry of the ring.

In order to quantify the symmetry of the ring, we introduce a quantity with energy unit we will call the rotational energy barrier, V_B. This quantity is inspired by the idea that a perfectly symmetric trap is rotationally invariant and has no preferred angular orientation. Another way of stating this is that one can smoothly shift each ion in a crystal to its neighbor's location without ever passing through a higher energy configuration. Therefore, if the symmetry is broken by some perturbation to the otherwise smooth energy landscape, the

distance from a symmetric system could be quantified by the size of that energy perturbation shifting the ions over one lattice site. Consider Fig. 5.1 where we analyze 10 ions confined in a ring. An electric field in the -y direction is breaking the symmetry and creating a lowest energy configuration where the ions prefer to sit a the bottom of the potential (a). If all of the ions were to be moved to the location of their neighbor in the counter clockwise direction, the lowest energy way of doing it would be for the ion labeled red to move over the highest potential point while all other ions relax into their lowest energy configuration given the red ion's fixed location (b). Fig. 5.1d shows how the energy of the system changes as a function of the angular position of the red ion. There is an increase in energy as the position of the red ion is changed and restores to the original value when the ion reaches the previous position of its counterclockwise neighbor (c) and the original configuration of the ring restored. The difference between the lowest energy configuration and the peak of the curve labeled in Fig. 5.1d is the definition of the rotational energy barrier. It is the smallest amount of energy required for the ion crystal to shift the location of its constituent ions, i.e. rotate.
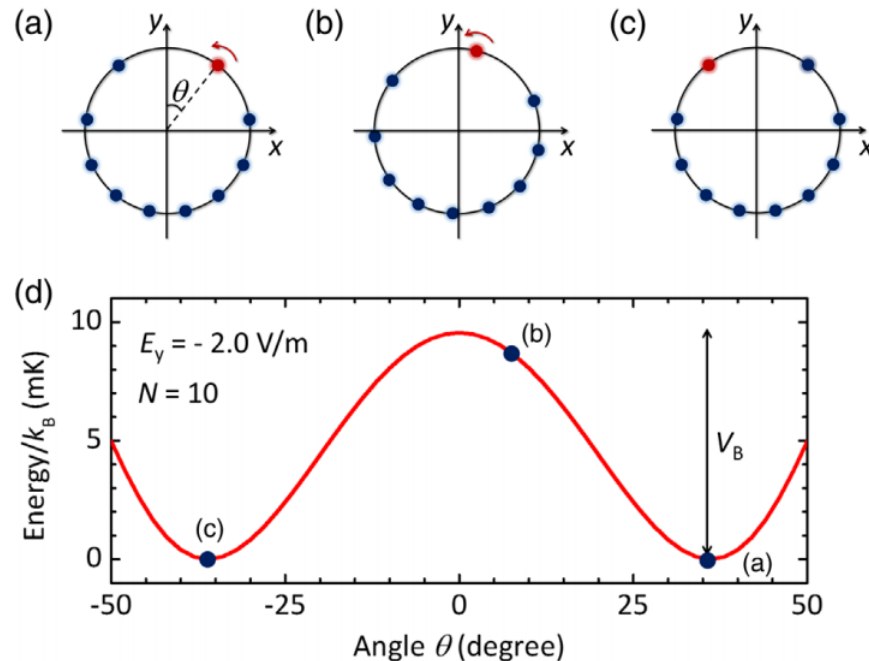
Figure 5.1: Energy barrier as a function of angular orientation. Figure from [24]. Part (a) shows the ground state configuration of an ion ring pinned by a symmetry-breaking electric field in the -y direction. The energy of the system is displayed in part (d). Part (b) shows how the state of the system constraining only the position of the red ion to different angle. This increases the energy of the system again shown in (d). In (c), the system returns to the original energy but all ions have been shifted one location. The height of the curve traced out by (d), labeled V_B is the energy barrier of this system.

Solving for the rotational energy barrier requires an understanding of the fields across the trapping location. As stated above, we expect that these fields are well-described by a multipole expansion and should be correctable with our DC electrodes. Therefore, the plan for making the ring symmetric and quantifying how successful we were at doing so is as follows:

1. Remove any stray fields being sourced from either the trap of the chamber to the best of our ability.

2. Apply what we assume to be an additional dipole field and prove that the behavior of the ion ring is consistent with the fields we expect to be present at the trapping site.

3. Use those fields to calculate the rotational energy barrier and study how symmetry is restored as the fields at the trapping site go to zero.

5.2 Trapping in a Ring and Compensation of Stray Electric Fields

Upon initial trapping in the ring potential, we first seek to confirm our initial simulations. By imaging the surface of the trap on the camera, we can calibrate the magnification of our imaging system by counting the pixels that span the radius of the inner most electrode, a known distance. With a known magnification, we analyze an image of the ion ring and find it to have a radius of 45 μm. The height can be approximated by imaging a laser beam mounted on a translation stage that is set up to graze the surface of the trap. Then we record the change on a micrometer screw between that point and the point at which the ion fluorescence is maximized. This yields a height of 390 ± 10 μm. This is consistent with our simulations for the trapping potential. When ions are first trapped in the ring potential, they are strongly pinned to one side of the ring. This is due to the presence of stray electric fields in the trapping region. The left figure in Fig. 5.2 shows what an ideal trapping potential would look like in the radial direction for the ring trap. All ions spread evenly across the extent of the ring because there is no preferred orientation. The right figure shows how this potential would perturb in the presence of a homogenous electric field. The potential tips in one direction causing the ions to localize in the direction of the electric field.

Assuming a multipole expansion of the fields, we can write down the energy of the system of ions to first order in the fields as,

$$V = -\sum_i \frac{1}{2} E_y ed \cos\theta_i + \sum_{i<j} e^2/(4\pi\epsilon_0 d \sin|\frac{\theta_i - \theta_j}{2}|) + \sum_i \frac{1}{2} m\omega^2 (r_i - d)^2 \tag{5.1}$$

where i, j indexes the ions, d denotes the ring diameter, r_i and θ_i are the radial and angular positions of the ith ion respectively, e is the elementary charge, E_y is the dipole component
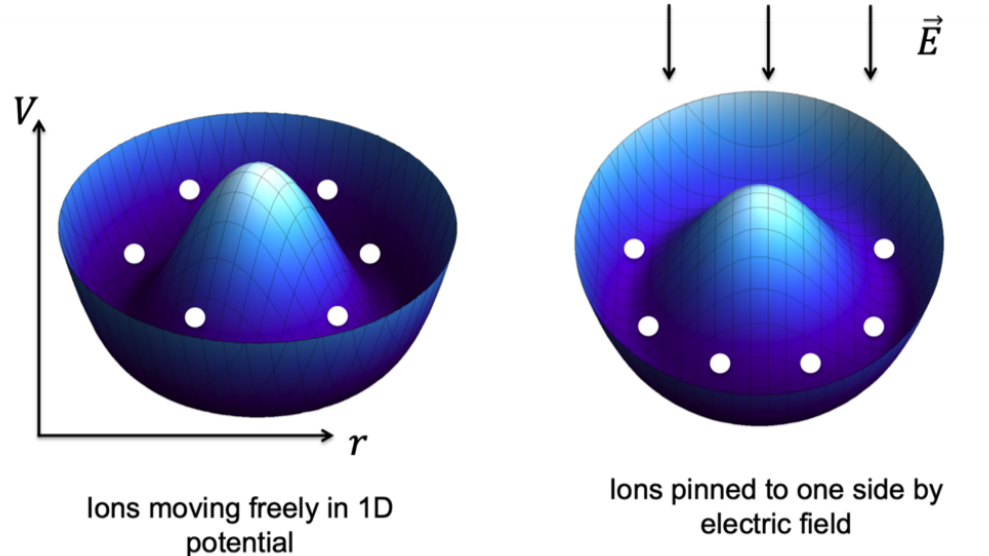
Figure 5.2: Isometric view of the potential experienced by the ions in the x-y plane when the fields are compensated (left) and when an external field is applied (right).

of the electric field in the pinning direction, ϵ_0 is the vacuum permittivity, m is the mass of calcium, and ω is the radial trap frequency. We can take an image of the ions, extract their positions using image recognition, and with equation 5.1 fit for E_y as the only unmeasured parameter such that the potential energy is minimized. Fig. 5.3 shows the original image of the pinned ions, their extracted positions, and how the fit locations and the true locations align. Measuring the fields in the way we find that the in-plane stray fields at the trapping location are 2.5 V/m. Discrepancies between the image and predicted positions could in principle be used to measure higher order multipoles; however, the precision of the original image itself is likely a significant source of uncertainty that would need to be removed in order to extract more precise information from this image analysis in the future.

Using the eight DC electrodes we can independently control the three dipole fields at the center of the trapping region and manipulate the position of the ions. Fig. 5.4 shows the combination of voltages that produce each field. By applying a dipole field opposing that of the stray field observed in the chamber, we can begin to restore the symmetry of the ring. As the stray field is compensated, the ions spread more evenly around the circumference of the ring as shown in Fig. 5.5. At a certain point, the ion crystal delocalizes and the ring unpins. The ions are still crystalized and have a well defined order; however, they no longer have a well defined global orientation. During a single camera exposure (100 ms) the Doppler cooled ions move through all potential orientations. It should be noted that the ring is illuminated by a Gaussian beams incident parallel to the surface of the trap with a waist of about 70 µm; therefore, the edges of the of the of the ring are illuminated with less power than the center yielding less fluorescence on the edges of the ring. The same dimming is observed if the ions are pinned to that side of the ring. This should not be confused with
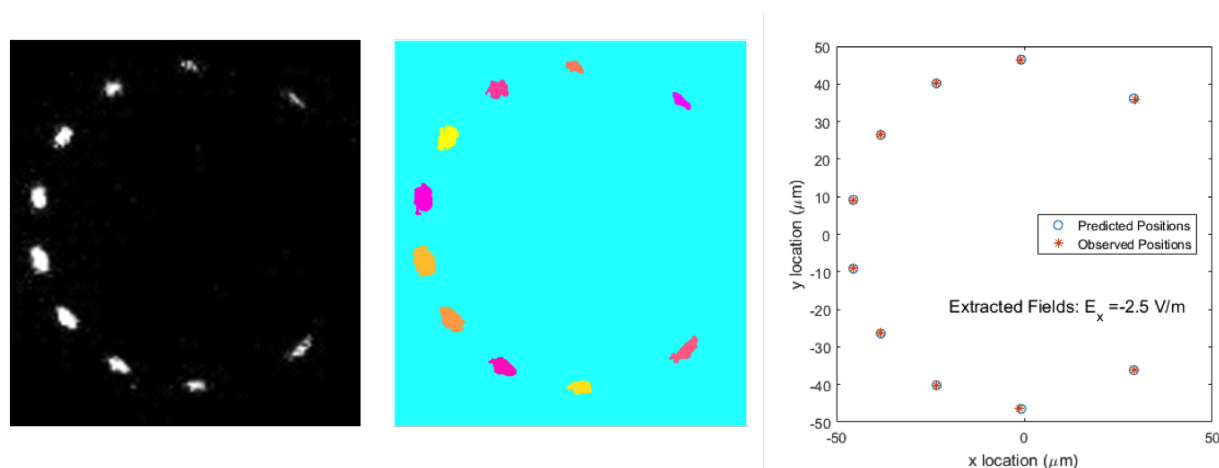
Figure 5.3: Left: 10 ions pinned by a field applied in the negative x direction. Center: Extracted ion positions using image recognition. Right: Agreement between the ion positions returned by the fit and the observed positions.

the ions have a smaller probability of being positioned at that location.
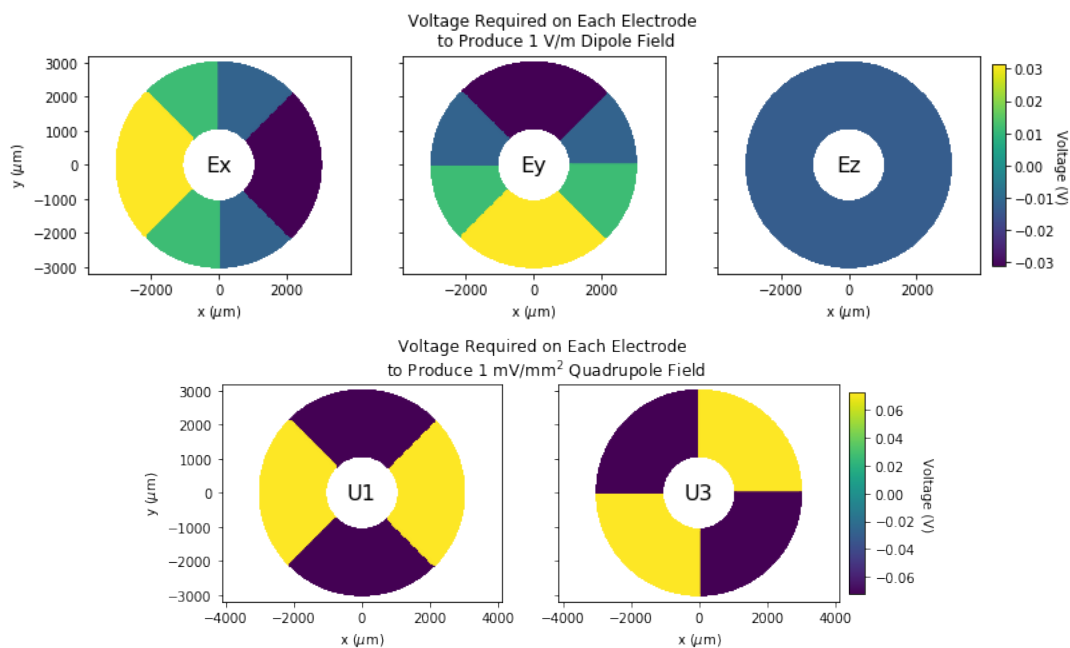
Figure 5.4: Voltages required to apply to the DC electrodes in order to produce various electric field multipoles at 1 V/m for dipole fields and 1 mV/mm^2 for quadrupole fields.

Delocalization necessarily occurs if one has a symmetric trap with a flat tangential potential; therefore, by observing delocalization we know we have already made a large step
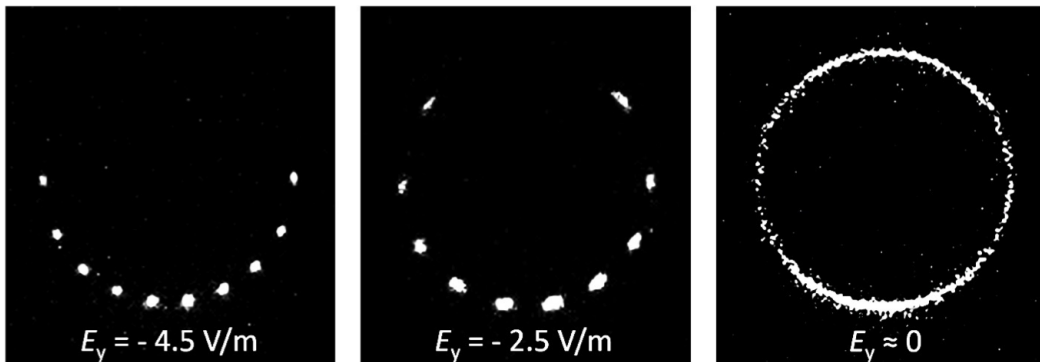
Figure 5.5: This figure is adapted from our publication [24]. Images of 10 ions pinned by a fields in the -y direction of strength 4.5 V/m, 2.5 V/m and 0 V/m respectively. Exposure time of 100ms.

towards having the most symmetric ring trap ever produced. The transition from pinned to delocalized is clearly important when assessing the symmetry of the ring. Fig. 5.6 shows the images collected on a CCD camera as the field pinning the ion ring is ramped from -5.6 V/m to 5.6 V/m. As we reduce the fields at the trapping field, the ions spread around the extent of the ring until at some non-zero field the crystal delocalizes. It then remains delocalized as we pass through zero field and turn up the field in the opposite direction. Once the field in the opposite direction is strong enough, the ring will recrystalize into a pinned configuration. There is a slight hysteresis associated with the recrystallization attributed to differences between the cooling of the localized and delocalized ions.

When running these experiments, it is helpful and sometimes necessary to know what the zero field point is, i.e. at what applied fields are the fields at the ion location fully compensated. In order to find that point, we apply the following procedure. First, we apply a strong field in the $+\hat{x}$ direction. Then, by adjusting E_y to make the ion crystal symmetric about the x-axis we find the field necessary to compensate fields in the y direction, E_{y0}. Similarly we can find E_{x0} by applying a strong E_y and making the crystal symmetric about the x axis. We also compensate in-plane quadrupoles which have spatial forms $U_1 = (x^2 - y^2)/2$ and $U_3 = xy$. With E_x and E_y compensated, the crystal can then be pinned with a quadrupole moment that is some combination of U_1 and U_3. We begin by compensating the quadrupoles such that the crystal delocalizes. Then, in order to compensate more precisely, we sweep U_1 and U_3 upward individually from a large negative value until the ring delocalizes. We then do the same thing sweeping down from a large positive value noting the delocalization field. The average of these two points is our quadrupole compensation field. We find typical dipole compensation fields of 2.5 V/m and quadrupole fields of 10 mV/mm^2 which are stable over many days.

When investigating the delocalization transition it is important to recognize the role the 397 nm laser illumination plays. If the laser is not illuminating both sides of the ring equally,
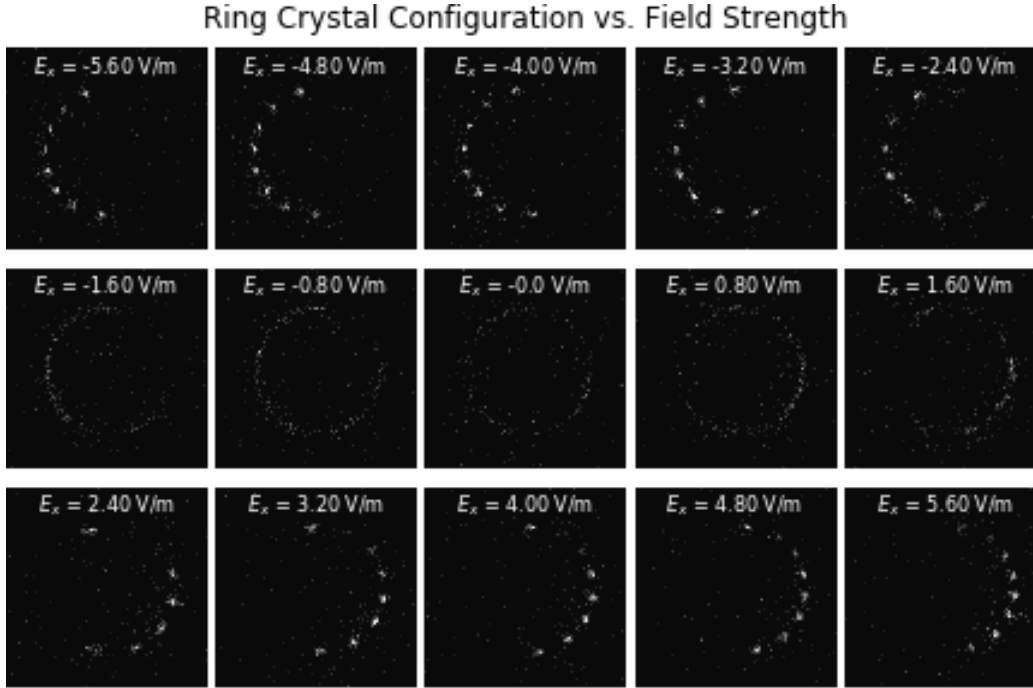
Figure 5.6: Image series of the delocalization transformation for 8 ions with the strength of the electric field in the x direction labeled at the top of each image.

the ring will experience an imbalance in radiation pressure. This imbalance exerts a torque on the ring which can push it over whatever rotational energy barrier remains causing an early onset of delocalization. Fig. 5.7 shows how the transition field depends on the 397 nm beam alignment. At 35 μm displacement, the field at which the transition occurs saturates. This is because the 397 nm beam has a width of 70 μm; therefore, at 35 μm displacement, the radiation pressure is maximally asymmetric and further displacement would not cause delocalization to be induced any earlier.

With the fields appropriately compensated, we can now intentionally apply a known electric field and study more precisely how the symmetry of the ring is restored as a function of field compensation.

5.3   Characterization of Symmetry-Breaking Fields

With the fields appropriately compensated, we are now poised to make a statement about the fields that break our symmetry. As argued before, we believe that the fields over the extent of the ring should be well-described by a multipole expansion and that compensating the dipole fields and in-plane quadrupole fields will restore the ring to a symmetric state. With the fields now nominally compensated, we can evaluate this claim.

By applying a homogenous electric field with our DC electrodes in the $-\hat{y}$ direction, we
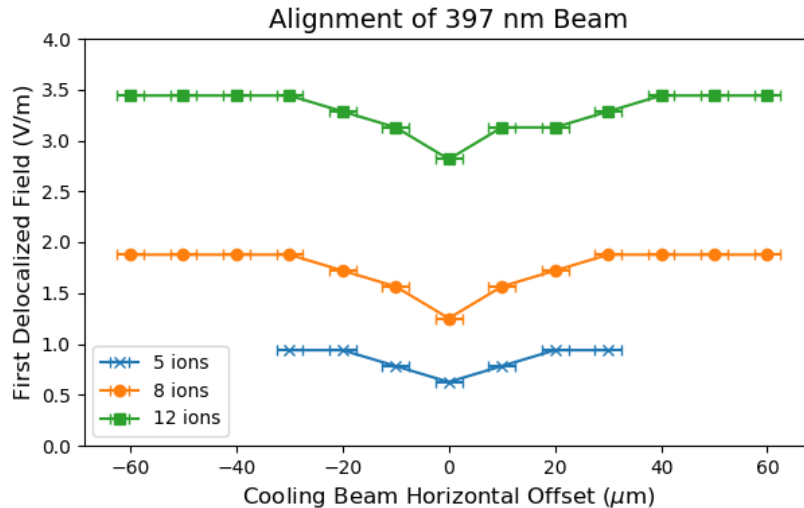
Figure 5.7: Delocalization field of ion rings as a function of the horizontal 397 nm beam alignment. Vertical resolution is 0.15 V/m, and the horizontal uncertainty is due to micrometer precision.

express the energy of the system as in Equation 5.1. With this potential, we can find the motional normal modes present in this crystal as outlined in Section 2.2. Specifically, we are interested in predicting the frequency at which the ions oscillate collectively in the direction tangential to the ring radius because this frequency is experimentally accessible. If the theoretically computed frequency (assuming only a dipole field) matches the experimentally measured frequency (which is influenced by the fields across the full extent of the ion ring), we can say that the fields over the entire trapping region are well modeled by our assumed fields and we have therefore achieved our goal of creating a system whose symmetry can be restored by a single set of compensation fields.

The common mode tangential mode frequency is measured through a method known as 'tickling'. While sweeping the frequency of a very small sinusoidal signal (10 mVpp) applied to one of the DC electrodes, the ions are monitored on the camera. As the frequency comes into resonance with one of the trap frequencies, the ions will become motionally excited and blur slightly on the camera. Fig. 5.8 sketches how this measurement is performed. Fig. 5.9 shows the measured trap frequencies as a function of both ion number and trapping field, which is measured by fitting the ion positions as mentioned previously. The trap frequencies cannot be measured through this method at very low frequencies because the crystal delocalizes even without a tickle. The theoretical line through the data is calculated assuming the energy given in Equation 5.1 and has no free parameters. The calculation fits the data through the full range. This suggests that at these energies we can fully model the fields at the trap as a single intentionally applied homogenous field which we compensate appropriately.
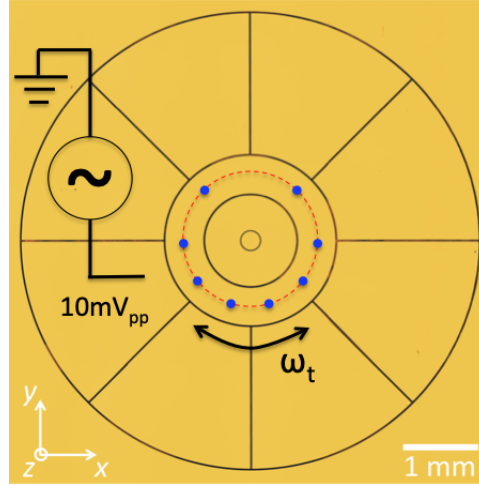
Figure 5.8: Circuit used to tickle the ions. The choice of electrode is to provide a common mode force along the tangential direction, labeled in the figure, at the trap frequency, ω_t.
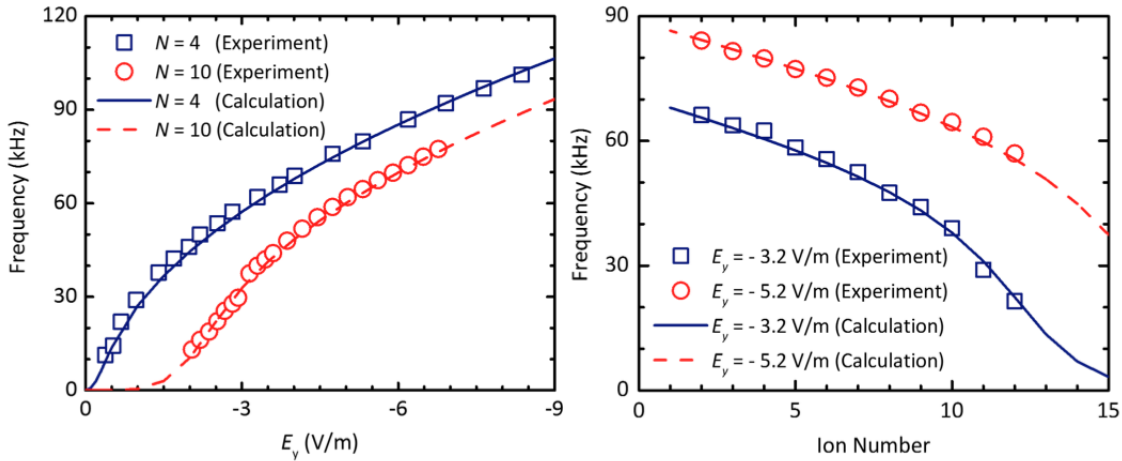
Figure 5.9: Fig. from [24]. Both figures show the common mode tangential frequency as a function of applied dipole field (left) and ion number (right). A zero parameter calculation for the trap frequency for the ion number and measured field strength is superimposed as a line through the data.

5.4 Delocalization Transition

Now that we understand the fields present at the trapping location, we can confidently calculate the energy barrier for our system. As stated earlier, the rotational energy barrier is found assuming an applied field and numerically solving the minimum energy needed to move all the ions over one position. Fig. 5.10 shows how the energy barrier depends on the strength of the dipole field and the number of ions. One can see that as the fields get small,

the energy barrier drops drastically. Additionally, as we increase the number of atoms, the energy barrier drops quickly as well. This occurs due to the fact that more ions means a stronger Coulomb repulsion which makes the ions spread more evenly across the ring despite a given symmetry-breaking field. At the current control limits of the system, we predict homogenous fields can be corrected for 10 ions down to the level of 10^{-12} Kelvin though at this temperature other effects such as higher order symmetry-breaking fields will surely set in.
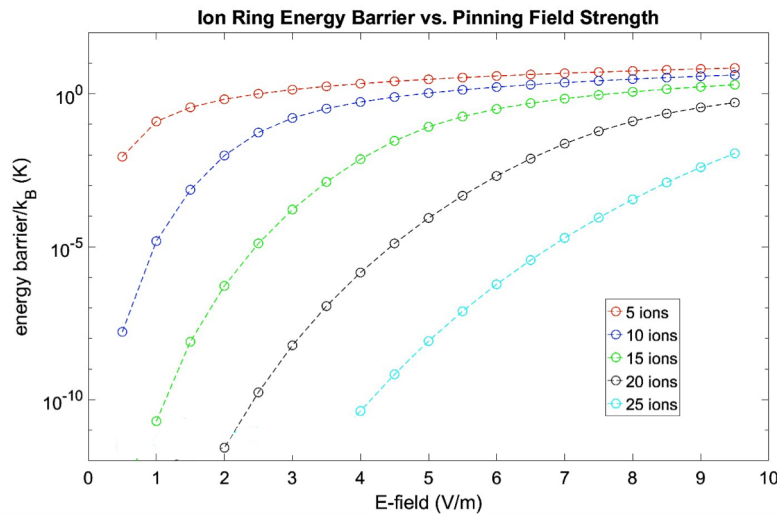
Figure 5.10: Calculated energy barrier in temperature units as a function of the size of a homogenous electric field for various numbers of ions.

By calculating the energy barrier at the field at which the ion crystal delocalizes, we can learn something about the cause of delocalization itself. The left plot of Fig. 5.11 maps out the transition field between localized and delocalized states as a function of the number of ions. The field at which the ring delocalizes increases as the number of ions increases suggesting with more ions it is easier to restore the symmetry. This is consistent with the simulations presented in Fig. 5.10. In the right plot of Fig. 5.11 we convert the y-axis into the energy barrier at the delocalization field. Now it is clear that the energy barrier with which the ion chain delocalizes is independent of the ion number.

The constant energy barrier suggests a transition dependent on a specific energy scale we presume to be the temperature of the ion chain. We perform a temperature measurement on the ion ring using 729 nm spectroscopy. Due to the dense packing of motional modes for large numbers of ions with very low-frequency modes, motional transitions within the ion crystal are not resolved spectroscopically. This is discussed more thoroughly in the next chapter. With these unresolved transitions, we can measure the temperature of the ion by measuring the width of the $S_{-1/2} \rightarrow D_{-5/2}$ transition and fitting a thermally broadened line. For an ion at temperature T, the Doppler-broadened width of a transition is a Gaussian of width
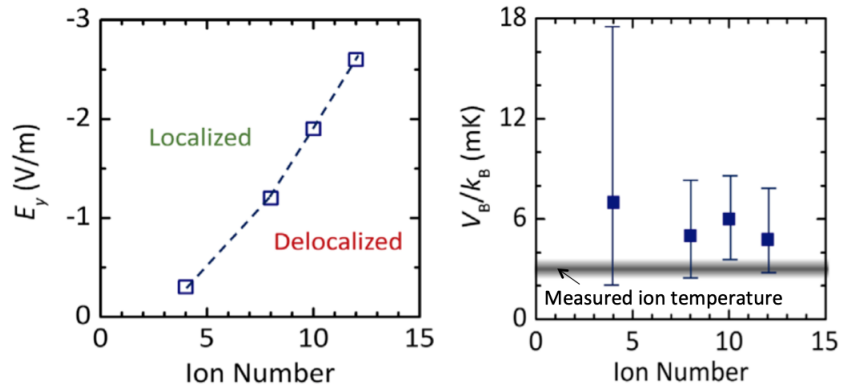
Figure 5.11: Left: Field at which delocalization occurs as a function of the ions number with the state of the ring labeled. Right: Energy barrier at the delocalization field vs ion number. Measured ion temperature shown as a grey bar with uncertainty.

$$\sigma_f = \sqrt{\frac{k_B T}{mc^2}} f_0 \tag{5.2}$$

where σ_f is the standard deviation of the broadened line, m is the mass of Calcium, k_B is Boltzmann's constant, c is the speed of light, and f_0 is the frequency of the transition (729 nm) [47]. Fitting this function to the electronic transition observed in the ring is shown in Fig. 5.12. We find the temperature to be about 3 mK. This is above the Doppler limit for the $^{40}Ca^+$ S$\rightarrow$P transition. Degenerate radial trap frequencies or lack of cooling in the vertical direction could be explanations for the discrepancy.

Fig. 5.11 shows the measured temperature of the ion on the same plot as the delocalization transition energy barrier. The transition occurs when the rotational energy barrier is reduced to near the temperature of the ions. This is consistent with the picture that when the ion delocalizes, the thermal energy of the ions is now enough to overcome any asymmetries in present in the tangential direction.

We can further confirm this model by simulating the transition from localized to delocalized using Langevin dynamics [48]. The ions' interaction with the Doppler cooling beam is modeled as a stochastic process which changes the velocity of each ion. Given these dynamics, we can bin the ion location at different angles as the system stochastically evolves in time and we can produce a histogram that corresponds to a fluorescence map integrated over a long time. Fig. 5.13 shows the agreement between the ion location histogram from the Langevin simulations and the images of the ring around the transition point. This further confirms our understanding of the delocalization occurring when the thermal energy of the ions overcomes any residual energy barriers.

Collectively, these measurements show that this trap design was successful in creating a ring trap whose symmetry can easily be restored. Stray fields present at the trapping location are easily compensated to the point where we experimentally reduce asymmetries
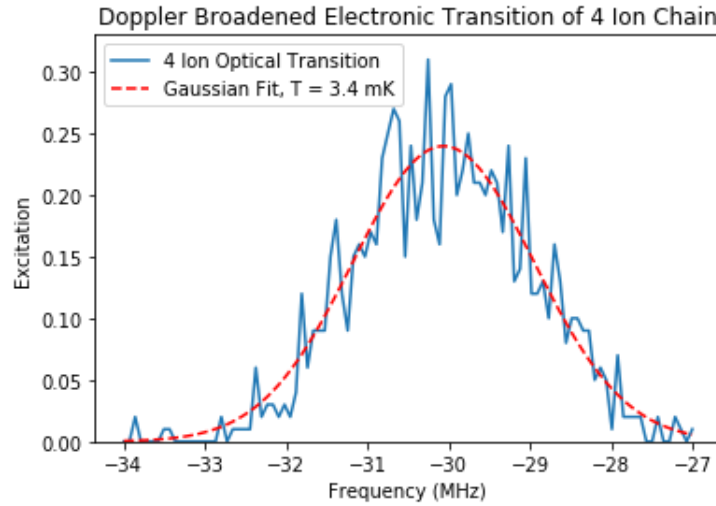
Figure 5.12: Electronic excitation on the $S_{-1/2} \rightarrow D_{-5/2}$ line for a four ion crystal, Doppler-broadened by temperature in the tangential direction (blue). A Gaussian fit of the data yields (dashed red).
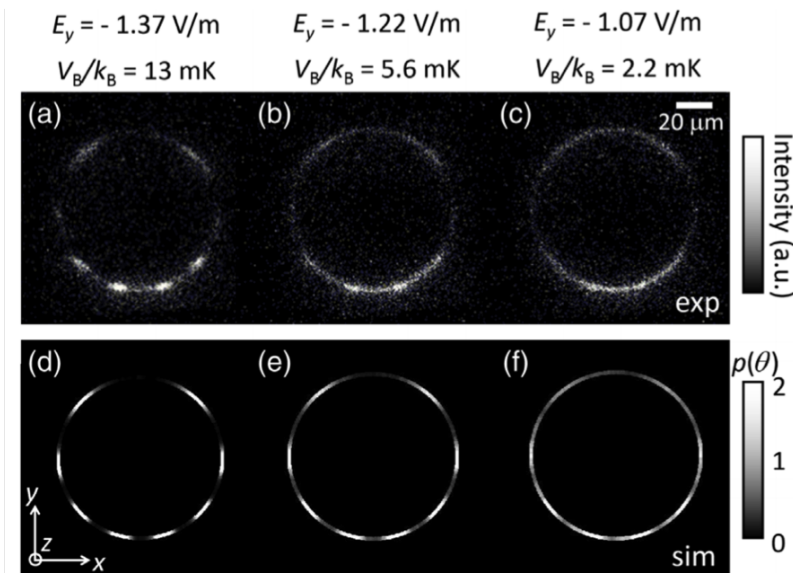
Figure 5.13: Figure from [24]. Top: Images of the ring undergoing the delocalization transition for various fields and energy barrier labeled above the image. Bottom: Histogram of location of the ions in a simulation where the ion dynamics are modeled by the Langevin equation taking into account stochastic movement at 3 mK. Simulation performed by Hao-Kun Li.

below the thermal temperature of the ions. Delocalization indicates symmetry restored at laser cooling temperatures, a much higher degree of symmetry than ever previously achieved.

Current estimates for the achievable rotational energy barrier are $< 10^{-12}$ K for dipole fields and 10^{-5} K for quadrupole fields though in order to experimentally probe this, sub-Doppler cooling of the ion chain would be necessary.

Chapter 6

Control of the Ring Trap

With the ring measured to be symmetric as expected, controlling and exploiting its unique properties is our next goal. Control of the ring possess three significant challenges that are not present in typical ion strings. The first is how to perform spectroscopy of the motional modes of the ring. Because the modes on which the laser has projection changes as a function of the point on the ring that is being addressed, spectroscopy is not straightforward. Additionally, the large number of low-frequency modes present makes resolving motional transitions very difficult. This ties into the second problem which is achieving sub-Doppler temperatures of the tangential modes of the ring. Because the tangential trap frequencies of the ring are so low, the motional modes are optically unresolved as shown previously in Fig. 5.12. This complicates typical cooling methods. The final challenge is controlling the tangential degree of freedom when the ring is compensated. Because the potential is smooth, there is no angular confinement of the crystal which means it moves freely, a property that does not exist in typical ion chains. Creating and controlling rotational states associated with the free motion would be a very useful tool. Progress and future prospects for ring spectroscopy, sub-Doppler cooling, and rotational control will be presented in this chapter.

6.1   Spectroscopy of the Ring

Typically, interactions between ions in Coulomb crystals are mediated by their shared motional modes. In calcium, these modes are manipulated optically by driving resolved transitions that selectively remove or add motional quanta to a specific mode (see equation 3.16). In a ring of ions, observing these transitions has a few challenges. In this section, I will now detail how we can spectroscopically observe the pinned, tangential motional transitions in this system and the challenges presented by the ring configuration.

In order to observe motional sidebands on the spectrum of the ion, the motion of the ion must modulate the frequency of the spectroscopy laser (729 nm). This is true for linear ion strings and the ring; however, with the ring we can change the projection of the motion in the direction of the laser by changing the ion position. In one configuration, such as the one

shown in the inset of the left panel of Fig. 6.1, the 729 nm laser addresses the tangential modes where the ions oscillate along the circumference of the ring. However, if the ion is rotated 90 degrees and the 729 nm beam shifted down, then the radial modes are addressed (inset of right panel in Fig. 6.1). Fig. 6.1 shows how the spectrum of a single ion can change with ion position. With tangential projection (left), one can see peaks every 105 kHz corresponding the tangential trap frequency created by the pinning fields (8.32 V/m). With a radial projection (right), the peaks are spaced by 390 kHz, the frequency of the radial mode created by the RF confinement.
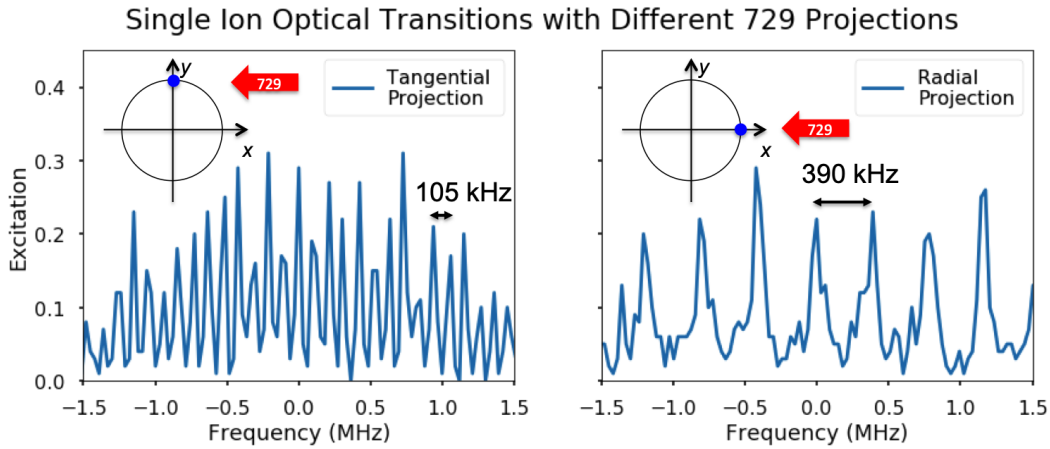
Figure 6.1: Spectrum of a single ion with a projection on the tangential modes (left) or the radial modes (right). The configuration with which the spectrum is taken is shown in the inset.

With the 729 nm laser projected on the tangential modes, we can achieve the spectrum shown in Fig. 6.2 on the blue curve for 8.32 V/m pinning. One can see clear peaks repeated every 105 kHz corresponding to the tangential mode of the ion. However, if a second ion is loaded, even when pinned strongly and cooled close to the Doppler limit, individual motional sidebands in the ring are no longer resolvable. The tangential spectrum for two ions is shown in Fig. 6.2 in the orange curve. The transition now looks like a continuous, Doppler-broadened peak spread over several MHz.

Motional sidebands become unresolved when there is more than one ion in the trap due to the fact in an N ion chain, there are N tangential modes which all have a very low frequency, even with strong pinning. Fig. 6.3 shows the mode frequencies for five ions at different pinning strengths. Notice that all tangential modes are under 250 kHz. The problem with many low-frequency modes is two-fold. Firstly, because their frequency is so low, they have a very large Lambe-Dicke factor and high $\bar{n}$ at the Doppler limit. This means that the typical expansion for the coupling to each sideband (expanded in factors of $\eta\sqrt{n+1}$, Equation 3.16) that produces a large suppression of coupling to higher-order sidebands is no longer valid. For a typical mode at 100 kHz, $\eta\sqrt{\bar{n}+1} = 4.5$ at the ring temperature (3 mK); therefore, each mode creates many orders of sidebands corresponding to roughly the width
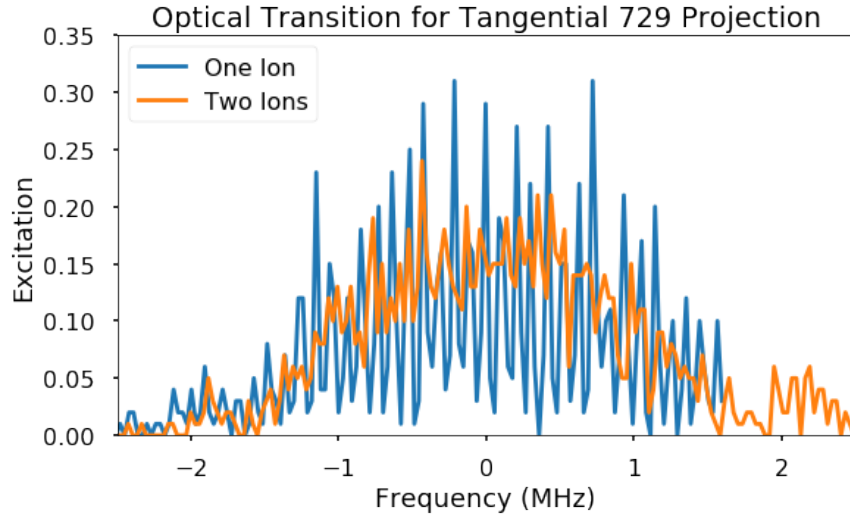
Figure 6.2: Spectrum of single ion (blue) and two ions (orange) with the laser addressing tangential modes, 8.32 V/m pinning.

of the width of the Doppler broadened peak (equation 5.2) divided by the trap frequency. Secondly, the density of the motional transitions does not scale linearly with the number of sidebands for each mode. For N ions with tangential motional sidebands out to m^{th} order for each sideband, there are m^N possible tangential sideband frequencies because a transition can add or subtract any number of quanta from any mode as long as the total change of quanta across all modes is less than m.
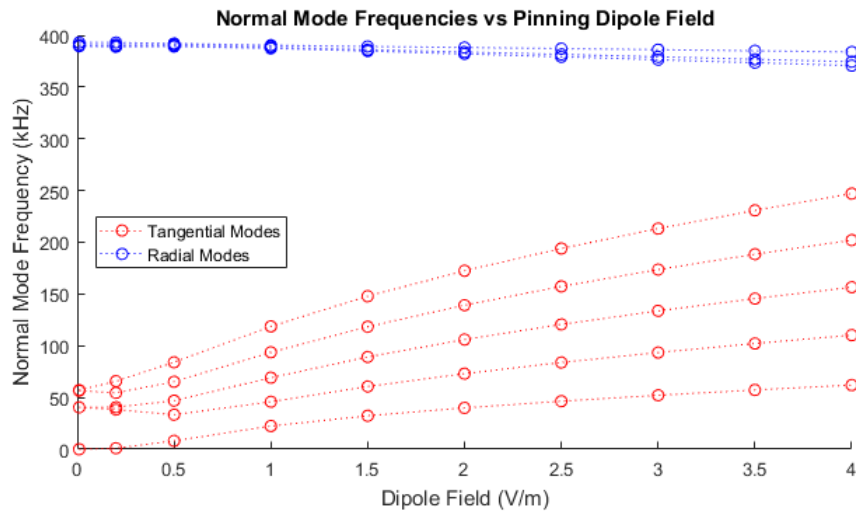
Figure 6.3: In-plane normal modes for a 5-ion, 47-µm radius, ring crystal as a function of dipole field strength. Modes are labeled as being either tangential or radial based on the direction of their oscillation.

In order to assess how significant this problem is, we calculate the full matrix element for each motional sideband using Equation 3.13 for all sideband combinations at a given temperature. Fig. 6.4 shows the relative strength of each tangential motional transition and the frequency at which it occurs for two ions at 3 mK pinned strongly with a field of 8.0 V/m. Even with ideal Doppler cooling (T = 0.5 mK), strong pinning (and therefore relatively large trap frequencies) and only a few ions (two), the motional spectrum quickly becomes an unresolvable forest of lines. Additionally, the width of the excitation as a whole matches what we expect for a Doppler-broadened line at the same temperature.
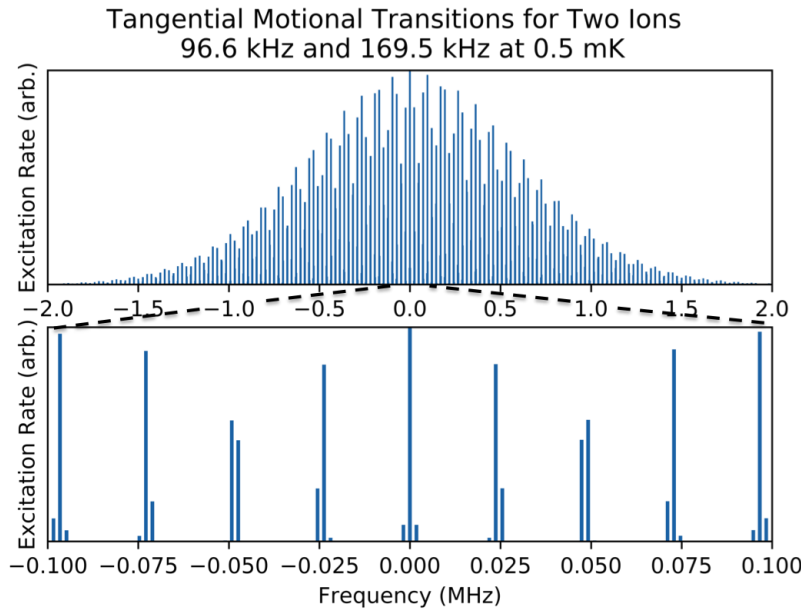
Figure 6.4: Coupling rates to each motional transition for two modes at 96.6 kHz and 169.5 kHz (typical 2 ion tangential frequencies) at 0.5 mK at 8.0 V/m pinning. The lower plot is a zoomed-in plot of the top plot.

6.2   Sub-Doppler Cooling

Sideband Cooling of the Ring

One method of resolving these transitions is through sideband cooling. Although the lines are unresolved, broadly addressing the ions on the red-detuned side of the peak amounts to a type of Doppler cooling with the 729/854 nm lasers. Red motional sidebands are preferentially driven and all modes are cooled. We perform this experiment with the 729 nm laser detuned about 0.5 MHz from resonance. The top two plots of Fig. 6.5 show the calculated spectrum at two different temperatures for motional modes of 62 kHz and 290 kHz respectively. The bottom plots are experimentally measured spectra where the same frequencies

are present. For two ions, unresolved sideband cooling works well enough that the individual transitions can begin to be resolved. Matching this spectrum to our simulations we can get an approximate temperature of 100 μK. Further increasing the number of ions, we no longer observed resolved lines even when sideband cooled, but the chain is clearly colder as evidenced by the narrowing of the Doppler-broadened transition. As the number of ions increases, the effectiveness of the unresolved sideband cooling decreases due to the increased density of motional modes. The final temperature extracted from a Gaussian fit as a function of the number of ions is shown in Fig. 6.6 along with an example of the narrowed line.
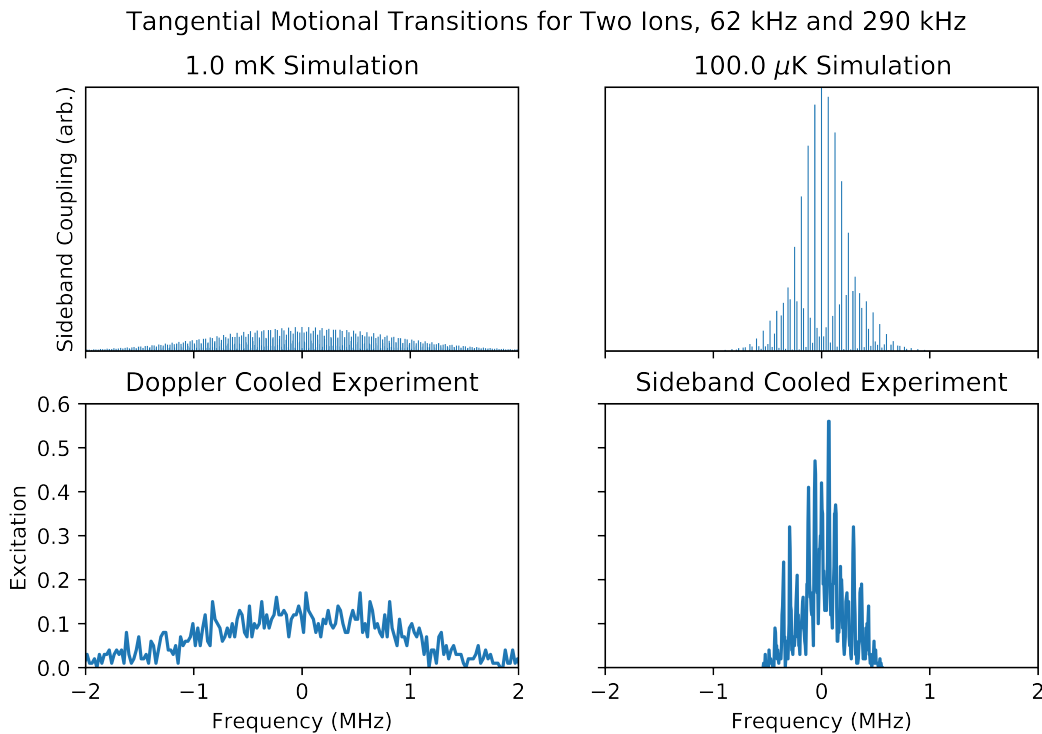
Figure 6.5: Top: Calculations of the sideband coupling for a two ion ring the lowest tangential and radial mode at 62 kHz and 290 kHz respectively, normalized to the largest peak on the right at 1 mK and 100 μK respectively. Bottom: Experimental spectra of a two ion crystal after Doppler cooling (left) and after sideband cooling (right).

This method is useful for a few, strongly pinned ions. The sideband cooling rate is constant (set by the 729 nm and 854 nm beam powers) and the density of sidebands is exponential in the number of modes; therefore, this method quickly becomes unpractical.

EIT

A more suitable cooling scheme for such a large number of unresolved degrees of freedom is known as Electromagnetically Induced Transparency (EIT) cooling. EIT cooling uses
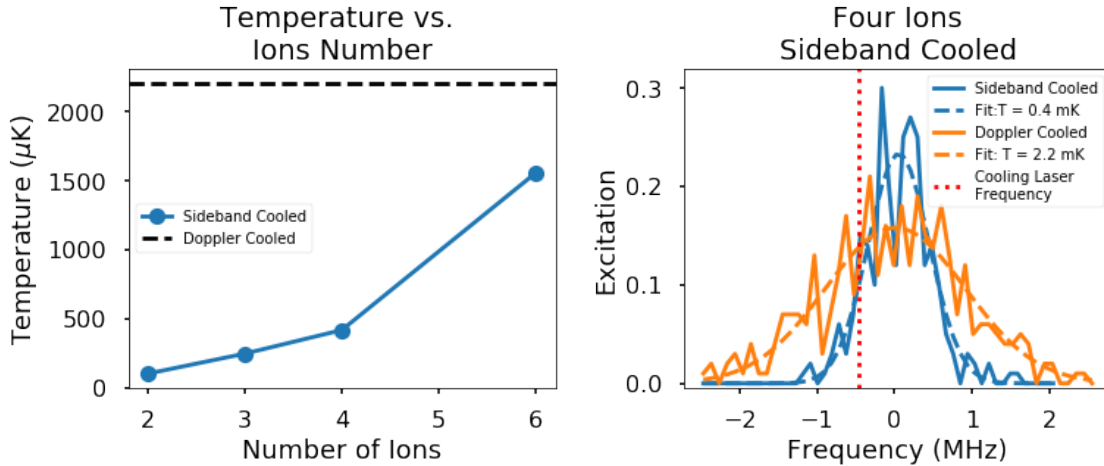
Figure 6.6: Left: Temperature of the ion after sideband cooling extracted by width of the Doppler-broadened transition as a function of ion number. Right: Example of temperature extraction before and after sideband cooling for four ions. The orange trace is a Doppler cooled spectrum and the blue is after sideband cooling. The respective Gaussian fits are shown in dashed lines and the red dotted line shows the sideband cooling frequency.

dressed atomic states to create very narrow atomic resonances. With the appropriate choice of atomic transitions, such features can be used to do fast, frequency-insensitive cooling of many modes simultaneously as discussed in Section 3.3. Lechner et al. have already demonstrated such cooling of 18 modes in a linear ion string of ^{40}Ca$^+$ and this source was heavily relied upon for realizing EIT cooling in our lab [18].

Our first realization of EIT was done with a single ion in a point trap where the trap is operated to produce a single RF null rather than a ring potential (see Section 7.2 for more details) for two reasons. Firstly, EIT cooling requires producing a Stark shift on the $P_{1/2}$ level on the order of the motional frequencies. This requires high laser intensity at the ion. Achieving these intensities necessary is easier if the system is small and the laser beams can be focused tightly. Secondly, the easiest way to see the cooling of multiple modes is by measuring sideband asymmetries (see Section 3.3) and as explained in the previous section, observing individual sidebands is very difficult in the ring system. However, for a single ion in a point trap, there are only three motional modes all of which are easily observable.

As stated in Section 3.3, EIT in calcium requires circularly (σ) and linearly (π) polarized light. In order to achieve this, the magnetic field must be precisely oriented along the propagation axis of the π polarized beam. In our experiment, we have 3D control of our magnetic field through current carrying coils positioned in all 3 directions around our vacuum chamber. For each one, we can zero the field at the ion by applying a small field with the other two coils (< 1 Gauss) and tuning the current such that the ion fluorescence is minimized. This occurs because as the field enforcing the quantization axis goes to zero, the ion's two ground states become degenerate and mix to form a dark state, thereby reducing

the fluorescence of the ion. Once the fields are zeroed, we can calibrate the field produced by each coil as a function of the current by measuring the field experienced by the ion. With this information, we can set the fields such that they are pointing toward the π light as in necessary. Fine tuning is done by measuring and minimizing the fluorescence of the σ^+ polarized beam because if the magnetic field is truly parallel to the circularly polarized beam, the atom should scatter about one photon before it is optically pumped into the ground state that is dark to the σ^+ beam. Fig. 6.7 shows the configuration of the lasers and B-field while running EIT.
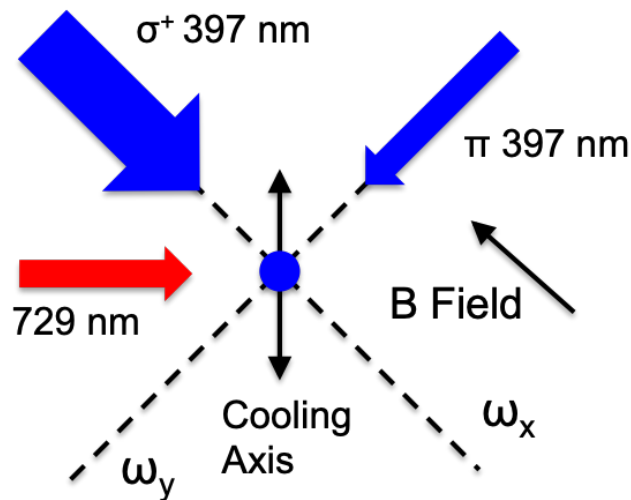
Figure 6.7: Top view of trap showing the orientation of the laser beams, B-field, and principle axes of motion, and cooling axis.

In order to cool modes at a frequency of about 1 MHz, the coupling laser must induce a Stark shift, δ, on the scattering transition of the same order. The method for measuring the Stark shift induced by the coupling laser is taken directly from [18] and their figure showing the relevant atomic levels is shown in Fig. 6.8. As a first measurement, the frequency of the transition between $S_{+1/2}$ and any D level is probed with no power in the coupling 397 nm beam for reference. For the second measurement, the ion is first moved to the D state with a π pulse. Then, with the high power 397 nm σ^+ polarized beam on, the same transition frequency is measured again. In this case, the frequency will be shifted by $\delta/2$ due to the dressing of the $S_{+1/2}$ state with the coupling beam. Because the coupling of the P level is strong, the transition to the D level is wide and must be driven very hard in order get significant excitation and overcome the quantum Zeno effect. The right plot of Fig. 6.8 shows how the line shifts with the dressing from the coupling beam in our experiment.

With this configuration, we achieve the characteristic Fano lineshape in the scattering rate need for EIT cooling, shown in Fig. 6.9. Placing the π beam frequency at the minimum of the Fano resonance, we achieve simultaneous ground state cooling of both radial modes
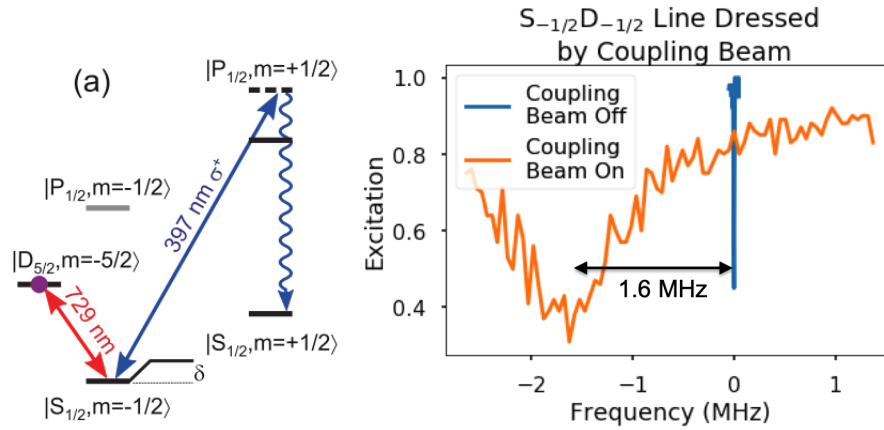
Figure 6.8: Left: (taken from [18]) Atomic levels participating in the Stark shift measurement and how they are modified by the coupling beam. Right: Our measurement of this shift.

of a single ion in 1 ms. Compared to sideband cooling, this would typically take 2 cycles of 6 ms each.
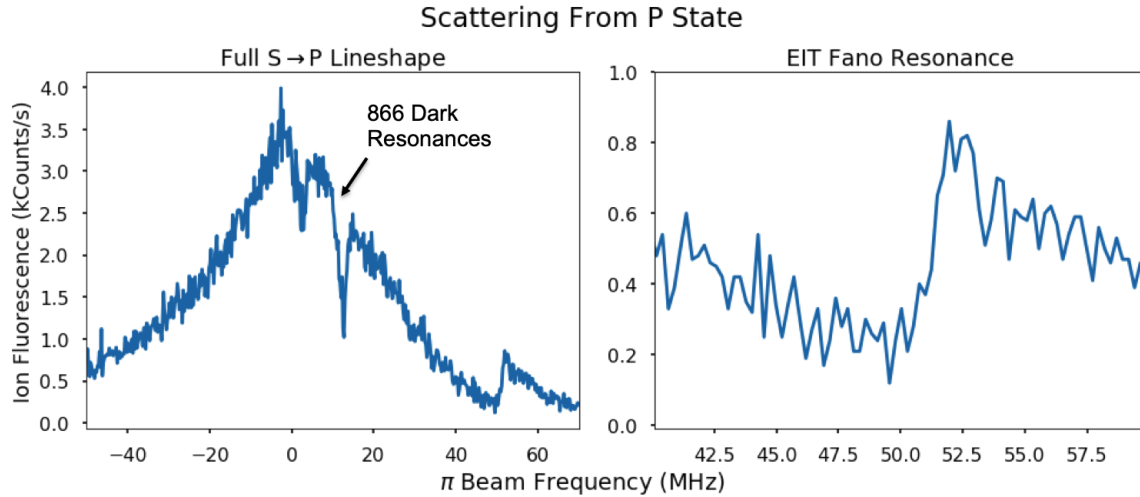
Figure 6.9: Scattering from the P state with coupling laser on detuned 50 MHz. The resonances around 15 MHz are due to the 866 nm beam coupling the P State with the $D_{3/2}$ level and is not used for EIT. The feature at 50 MHz is the resonance used for EIT cooling.

Using the point trap, we next attempted EIT cooling of two ions. For the same calibration, cooling was not achieved. We attribute this to the presence of micromotion. Since a point trap has only a single RF null, a two ion crystal will necessarily have micromotion as both ions will be pushed out of the null. As laid out in Section 3.3, EIT can cool because of the asymmetry in the absorption of the carrier, blue sideband, and red sideband. If the ion has large micromotion, one gets copies of the spectrum at $\pm\Omega_{\mathrm{RF}}$. If the RF drive frequency

is comparable to the beam detuning, this means that the micromotion lines will scatter off the main transition peak, increasing the final temperature after EIT cooling and potentially actively heating the ion. Fig. 6.10 shows the location of absorption lines in the presence of micromotion as they relate to the scattering rate. One can see that with our detuning of 50 MHz and micromotion at ± 25 MHz, the micromotion lines are on the downward slope of the main absorption peak, creating a large heating mechanism in our system.
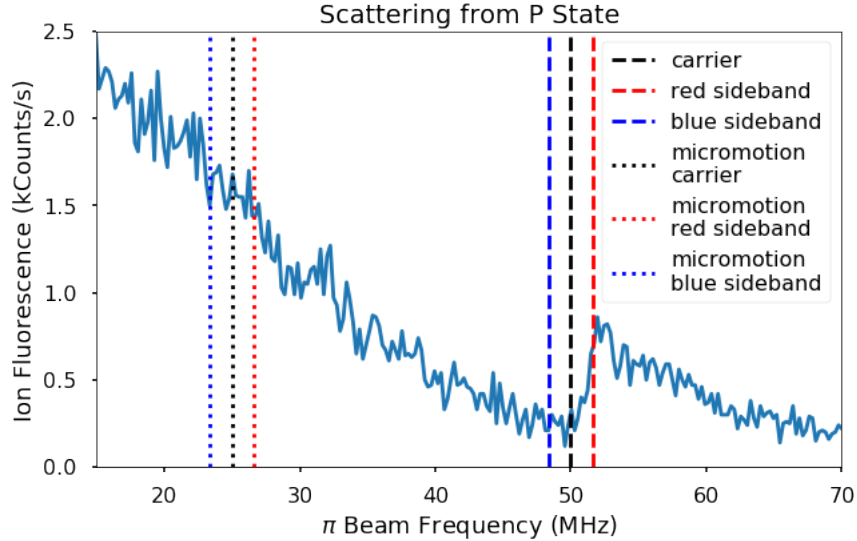
Figure 6.10: Scattering from P state and motional lines for a trap frequency of 1.62 MHz and a RF drive frequency of 25 MHz.

While EIT cooling for ion chains will not work in a point trap configuration, it is still a valid approach for the ring trap in which the micromotion can be compensated. The challenge for the ring remains to get a large, homogenous Stark shift on multiple ions to achieve efficient cooling of all modes. Focusing in the plane of the ring with a cylindrical lens and identifying which ions participate most strongly in relevant modes would reduce the amount of power needed to achieve the necessary Stark shift and cooling rate in a ring.

6.3 Rotation

One of the most unique features of the symmetric ring trap is the ability of the ions to rotate freely. In order to capitalize on the potential opportunities presented by this property, we consider two methods for controlling this degree of freedom: rotation due to an imbalance in radiation pressure and rotation induced by a rotating asymmetry.

Radiation Pressure

In Fig. 5.7, it was already shown that an imbalance in radiation pressure can cause the ion ring to delocalize prematurely. This is due to the fact that if more 397 nm light is illuminating one side of the ring than the other, that side will scatter more photons and experience a torque. The torque not only effectively reduces the energy barrier, but it causes a rotational bias in the free movement in the rotational degree of freedom.

In order to study how large of an effect this is, we start by spectroscopically addressing the S to D transition when the ion ring is delocalized and the 397 nm beam is balanced. Because the ring is delocalized, rather than measuring the excitation of a single ion directly, we measure the full fluorescence of all ions in the ring. When the ions are excited, the fluorescence drops. In the blue in Fig. 6.11, the Doppler-broadened transition can be seen. If the 397 nm laser is then displaced 5 µm downward as shown in configuration 1, in orange one can see the transition is shifted to the blue by 4 MHz if the 729 nm beam is focused on the other side of the ring. This is because the Doppler shift experienced by the ions is $\Delta f = \omega_{\rm rot} r f / c$ where Δf is the frequency shift, $\omega_{\rm rot}$ is the rotational speed, r is the ring radius, f is the transition frequency, and c is the speed of light. Therefore, a shift of 4 MHz corresponds to a rotation frequency of approximately $2\pi \times 5$ kHz. In green it can be seen that the direction of the shift changes when the 397 nm laser is moved to the same side of the ring as the 729 nm laser.
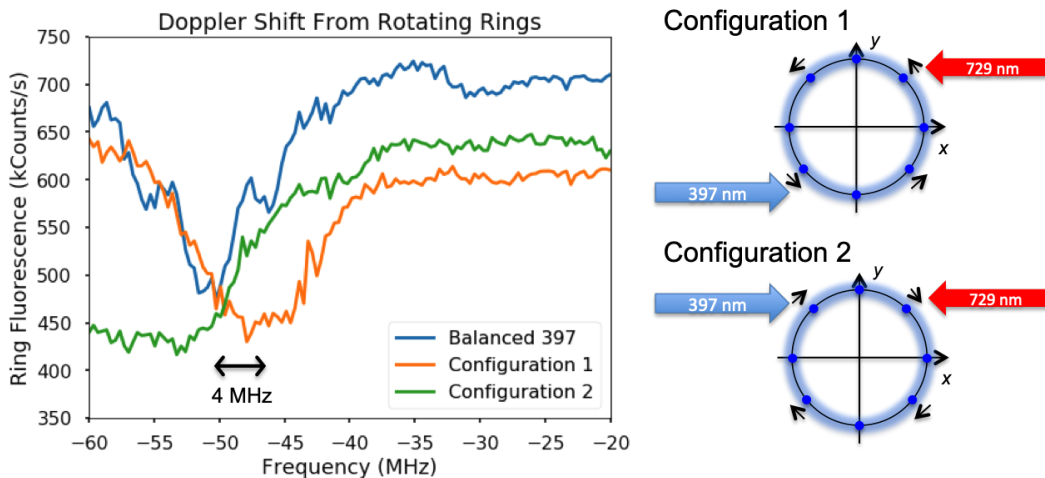
Figure 6.11: Fluorescence of the fully compensated ring with the 729 nm beam addressing only one side of the ring and the 397 nm beam in various locations. The blue trace has the 397 nm beam balanced, the orange and green has the 397 nm beam intentionally misbalanced in the configurations shown on the right.

The shift of the atomic transition is evidence of rotation; however, the rotation frequency from this method of rotation is difficult to control as it depends on the precise alignment and beam profile of the 397 nm beam. Potentially, this could be stabilized by having two

counter-propagating 397 nm beams with slightly different detunings to enforce a specific rotation speed. As the radiation pressure from one beam spins up the ring, it goes out of resonance and therefore applies less torque. At the same time, the counter propagating beam comes more on resonance and applies a larger torque in the opposite direction. By adjusting the beams relative detuning, one could imagine controlling the precise speed at which the crystal rotates. This has yet to be explored experimentally.

Rotating Asymmetry

Another method of rotational control can be achieved through applying a rotating asymmetry. As shown in the previous section, a stray field can cause the ion crystal to have a preferred orientation. If the angle or the asymmetric field itself were rotated at a certain frequency, the ion ring would track that motion. Then upon reaching a target speed, the asymmetry could be released and the ions left to rotate freely in a smooth potential. This method will be discussed at length in the next chapter in the context of the point trap, but has yet to be attempted in the ring trap though the method and technical control would be identical.

Chapter 7

Coherent Control of Rotational States

Many of the derivations and simulations presented in this chapter and the next were done in conjunction with Neil Glikin, also from the Haeffner lab, whose help and insights were invaluable to this project.

7.1   Introduction

As discussed in Section 2.2, the motion of ion crystals is described through collective modes of oscillation. Manipulating this motion is the primary method through which sub-Doppler cooling and entanglement are achieved in ion strings [49, 50, 51, 52]. With the creation of a symmetric ion ring as demonstrated in the previous chapters, we now can consider the uses of a new type of collective motion within an ion string. Because the ring in not confined in the azimuthal direction, the frequency of the common mode motion goes to zero and becomes like a rotor rather than a harmonic oscillator.

Control of this new rotational of degree of freedom could give us a new handle quantum experiments. As a closed system with periodic boundary conditions, rotational states have numerous potential applications. The closed current loop they form are potentially useful for detecting magnetic fields and studying Arharonov-Bohm style physics [53, 54]. The periodic boundary conditions enable fundamentally new operations such as the deterministic coherent exchange of the ions' wave functions [55] and the ability to create interferometry geometries new to ions [56, 57]. Rotating ion rings have even been proposed as a method for studying Hawking radiation in acoustic analogs of black holes [34, 58]. Additionally, the Hamiltonian describing the rotation of ion strings is same as the one describing the rotation of trapped molecules, potentially allowing for the future simulation of molecular dynamics in a synthetic ion rotor [59, 60, 61]. Finally, the wave functions of rotating ion strings are very large (of order the ring radius, many microns) and spatially symmetric in contrast to harmonic oscillator states which are typically only a few tens of nm wide and have a preferred orientation along the oscillation eigenvector. The extended size and symmetry of rotor states changes the way the ions interact with decoherence sources such as noisy electric fields and are therefore have

applications in sensing and metrology [62, 63, 64, 65, 66].

For these reasons, we set out to establish quantum control of the rotational motion of an ion ring. This means we want the ability to put the ring in superposition of rotational states and control the phase and population of that superposition. In this chapter, I will describe a protocol for doing just this. We will utilize a slightly different operational configuration of the trap presented in the previous chapters though it will still be an ion ring. I will begin the chapter by describing this new configuration and the dynamics of ions trapped within its potential. I will then describe how we can create rotational superpositions by using classical rotation to create optically addressable motional sidebands. Finally, I will present Rabi oscillations between rotational states and Ramsey experiments demonstrating the expected behavior of the rotational superpositions.

7.2 Two Ions in a Point Trap and a Rotor Hamiltonian

Two Ions in a Point Trap

The experiments performed in this and the following chapter are done with two ions loaded into a Paul trap with RF confinement in all three dimensions and a single RF null, i.e. a point trap. This is done in the same trap described in Chapter 4 operated in a different configuration. For the point trap, RF is applied to the second circular electrode while the other two remain grounded as labeled in Fig. 7.1. This creates a system in which a single ion experiences an external potential which can be described by three harmonic oscillators, one for each of the x, y, and z directions, where z is normal to the trap surface. These oscillator frequencies will be referred to as ω_x, ω_y, and ω_z. Applying a sinusoidal voltage with a frequency of 21 MHz and an amplitude of 57 V yields trap frequencies of $\omega_x = \omega_y = \frac{1}{2}\omega_z = 2\pi \times 842$ kHz at a height of 181 μm above the trap surface.

Let us consider the system of two ions in a point trap and analyze their collective wave functions. The Hamiltonian of the 2-ion system in our 3D harmonic trap is

$$
\begin{aligned}
H = \frac{\mathbf{p}_1^2}{2m} + \frac{\mathbf{p}_2^2}{2m} + &\frac{1}{2}m\omega_x^2 x_1^2 + \frac{1}{2}m\omega_x^2 x_2^2 \\
&+ \frac{1}{2}m\omega_y^2 y_1^2 + \frac{1}{2}m\omega_y^2 y_2^2 \\
&+ \frac{1}{2}m\omega_z^2 z_1^2 + \frac{1}{2}m\omega_z^2 z_2^2 + V_{\text{Coul}}(\mathbf{r}_1 - \mathbf{r}_2).
\end{aligned}
\tag{7.1}
$$

where V_{Coul} is the potential produced by the ions' mutual Coulomb repulsion. We can rewrite the coordinates $\mathbf{r}_1$ and $\mathbf{r}_2$ in terms of center-of-mass and relative coordinates $\mathbf{R}$ and $\mathbf{r}$:

$$
\begin{aligned}
\mathbf{R} &= \tfrac{\mathbf{r}_1 + \mathbf{r}_2}{2}, \\
\mathbf{r} &= \mathbf{r}_1 - \mathbf{r}_2
\end{aligned}
\quad\Longrightarrow\quad
\begin{aligned}
\mathbf{r}_1 &= \mathbf{R} + \tfrac{1}{2}\mathbf{r}, \\
\mathbf{r}_2 &= \mathbf{R} - \tfrac{1}{2}\mathbf{r}
\end{aligned}
\tag{7.2}
$$
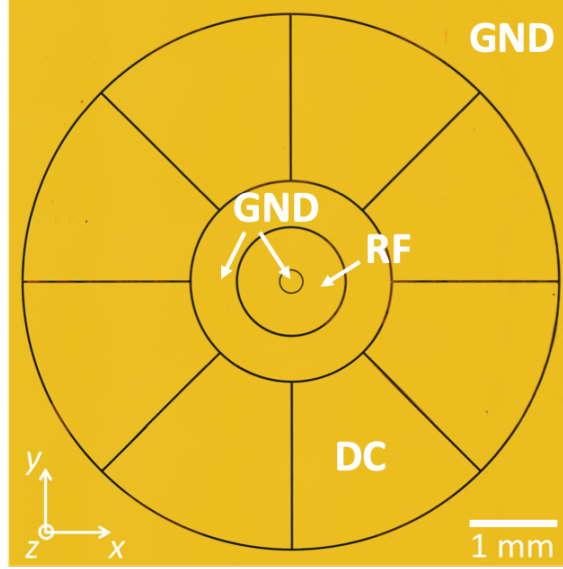
Figure 7.1: Image of the trap with electrode assignments for the point trap configuration labeled.

So, isolating one dimension, the expression $x_1^2 + x_2^2$ becomes

$$x_1^2 + x_2^2 = \left(X + \frac{1}{2}x\right)^2 + \left(X - \frac{1}{2}x\right)^2 = 2X^2 + \frac{1}{2}x^2, \tag{7.3}$$

where X and x are the x-components of $\mathbf{R}$ and $\mathbf{r}$. The corresponding conjugate momenta are

$$\begin{aligned}\mathbf{P} &= \mathbf{p}_1 + \mathbf{p}_2, \\ \mathbf{p} &= \frac{\mathbf{p}_1 - \mathbf{p}_2}{2}\end{aligned} \qquad \implies \qquad \begin{aligned}\mathbf{p}_1 &= \tfrac{1}{2}\mathbf{P} + \mathbf{p}, \\ \mathbf{p}_2 &= \tfrac{1}{2}\mathbf{P} - \mathbf{p}\end{aligned} \tag{7.4}$$

Now the momentum terms are written as

$$\frac{\mathbf{p}_1^2}{2m} + \frac{\mathbf{p}_2^2}{2m} = \frac{1}{2m}\left[\left(\frac{1}{2}\mathbf{P} + \mathbf{p}\right)^2 + \left(\frac{1}{2}\mathbf{P} - \mathbf{p}\right)^2\right] = \frac{\mathbf{P}^2}{2M} + \frac{\mathbf{p}^2}{2\mu}, \tag{7.5}$$

where $M = 2m$ is the total mass and $\mu = m/2$ is the reduced mass. Making these substitutions into the full Hamiltonian, it can be written

$$\begin{aligned}H = \frac{\mathbf{P}^2}{2M} + \frac{\mathbf{p}^2}{2\mu} &+ \frac{1}{2}M(\omega_x^2 X^2 + \omega_y^2 Y^2 + \omega_z^2 Z^2) \\ &+ \frac{1}{2}\mu(\omega_x^2 x^2 + \omega_y^2 y^2 + \omega_z^2 z^2) + V_{\text{Coul}}(\mathbf{r}).\end{aligned} \tag{7.6}$$

Writing the Hamiltonian in such a way shows that it can be separated in the center-of-mass and relative coordinates:

$$H = H_{\text{COM}} + H_{\text{rel}}, \tag{7.7}$$

where

$$
\begin{aligned}
H_{\text{COM}} &= \frac{\mathbf{P}^2}{2M} + \frac{1}{2}M(\omega_x^2 X^2 + \omega_y^2 Y^2 + \omega_z^2 Z^2), \\
H_{\text{rel}} &= \frac{\mathbf{p}^2}{2\mu} + \frac{1}{2}\mu(\omega_x^2 x^2 + \omega_y^2 y^2 + \omega_z^2 z^2) + V_{\text{Coul}}(\mathbf{r}).
\end{aligned}
\tag{7.8}
$$

Eigenstates of this Hamiltonian can therefore be written as product states of "COM states" and "relative states". The COM Hamiltonian is an ordinary 3D harmonic oscillator for a particle with mass M, so its eigenstates can be written as harmonic oscillator Fock states, e.g. $|N_x\rangle |N_y\rangle |N_z\rangle$, with the frequencies in the 3 directions being ω_x, ω_y, and ω_z. The relative Hamiltonian exhibits a potential which is a Coulomb potential in addition to a Harmonic oscillator potential:

$$
\begin{aligned}
H_{\text{rel}} &= \frac{\mathbf{p}^2}{2\mu} + V(\mathbf{r}), \\
V(\mathbf{r}) &= \frac{1}{2}\mu(\omega_x^2 x^2 + \omega_y^2 y^2 + \omega_z^2 z^2) + V_{\text{Coul}}(\mathbf{r}) \\
&= \frac{1}{2}\mu(\omega_x^2 x^2 + \omega_y^2 y^2 + \omega_z^2 z^2) + \frac{e^2}{4\pi\epsilon_0} \frac{1}{\sqrt{x^2 + y^2 + z^2}}
\end{aligned}
\tag{7.9}
$$

There are two cases here which merit separate analysis. Firstly, the more familiar scenario for ion trap experiments when $\omega_x \neq \omega_y$ and secondly, the more complicated scenario where $\omega_x = \omega_y$:

1. $\omega_x \neq \omega_y$
   This is the case when we have pinned ions. Let us choose the convention $\omega_x < \omega_y < \omega_z$. In this case, the equilibrium position of the ion crystal will be oriented along the x-axis separated by $d = \left[\frac{e^2}{4\pi\epsilon_0} \frac{1}{\mu\omega_x^2}\right]^{1/3}$. If we are interested only in states which are close to the ground state then we may expand the Coulomb term about this equilibrium point and we find for the Coulomb potential:

$$
\begin{aligned}
\frac{e^2}{4\pi\epsilon_0} \frac{1}{\sqrt{x^2 + y^2 + z^2}} &\approx \frac{e^2}{4\pi\epsilon_0} \left(\frac{1}{d} - \frac{x-d}{d^2} + \frac{(x-d)^2}{d^3} - \frac{y^2}{2d^3} - \frac{z^2}{2d^3} \right) \\
&= \underbrace{\frac{e^2}{4\pi\epsilon_0} \frac{1}{d^3}}_{\mu\omega_x^2} \left[(x^2 - 3dx + 3d^2) - \frac{1}{2}y^2 - \frac{1}{2}z^2 \right].
\end{aligned}
\tag{7.10}
$$

With this substitution, the full potential is

$$
\begin{aligned}
V(\mathbf{r}) &\approx \frac{1}{2}\mu\omega_x^2 x^2 + \frac{1}{2}\mu\omega_y^2 y^2 + \frac{1}{2}\mu\omega_z^2 z^2 + \mu\omega_x^2\left[(x^2 - 3dx + 3d^2) - \frac{1}{2}y^2 - \frac{1}{2}z^2\right] \\
&= \frac{3}{2}\mu\omega_x^2\left[(x-d)^2 + d^2\right] + \frac{1}{2}\mu(\omega_y^2 - \omega_x^2)y^2 + \frac{1}{2}\mu(\omega_z^2 - \omega_x^2)z^2 \qquad (7.11) \\
&= \frac{3}{2}\mu\omega_x^2(x-d)^2 + \frac{1}{2}\mu(\omega_y^2 - \omega_x^2)y^2 + \frac{1}{2}\mu(\omega_z^2 - \omega_x^2)z^2 + \text{const.}
\end{aligned}
$$

This is a 3D harmonic oscillator in the coordinates $(x-d, y, z)$, with frequencies $\sqrt{3}\omega_x$, $\sqrt{\omega_y^2 - \omega_x^2}$, and $\sqrt{\omega_z^2 - \omega_x^2}$. These will be referred to as the stretch mode, in-plane tilt mode, and vertical tilt modes, respectively.

2. $\omega_x = \omega_y$ $(\equiv \omega_\rho)$

   Ultimately, this is the rotationally symmetric system we hope to achieve. In this case there is no pinning; the ions have no preferred direction within the horizontal plane. Here it makes sense to move into cylindrical coordinates (ρ, θ, z) where $x = \rho\cos\theta$, $y = \rho\sin\theta$. Now

$$
V(\mathbf{r}) = \frac{1}{2}\mu\omega_\rho^2\rho^2 + \frac{1}{2}\mu\omega_z^2 z^2 + \frac{e^2}{4\pi\epsilon_0}\frac{1}{\sqrt{\rho^2 + z^2}} \qquad (7.12)
$$

As similar treatment to above leads to the approximation

$$
V(\mathbf{r}) \approx \frac{3}{2}\mu\omega_\rho^2(\rho - d)^2 + \frac{1}{2}\mu(\omega_z^2 - \omega_\rho^2)z^2 + \text{const.} \qquad (7.13)
$$

The full Hamiltonian can be separated into "horizontal" and "vertical" terms:

$$
H = \left[\frac{p_x^2}{2\mu} + \frac{p_y^2}{2\mu} + \frac{3}{2}\mu\omega_\rho^2(\rho - d)^2\right] + \left[\frac{p_z^2}{2\mu} + \frac{1}{2}\mu(\omega_z^2 - \omega_\rho^2)z^2\right] \qquad (7.14)
$$

In the vertical direction we have a harmonic oscillator with frequency $\sqrt{\omega_z^2 - \omega_\rho^2}$. In the horizontal direction, we have what looks like a trapped diatomic molecule confined to two dimensions. The "molecular" potential is formed by the balancing of the Coulomb repulsion and the trap confinement, resulting in a potential which is dependent on the inter-ion distance (yielding a minimum at some distance d) but independent of ion crystal angle.

In both cases, we can separate out the vertical and horizontal directions (with the vertical direction always in the form of a harmonic oscillator), so generically an eigenstate state of the relative coordinates will look like $|\chi\rangle\,|n_z\rangle$, with $|\chi\rangle$ describing the horizontal state. If $\omega_x \neq \omega_y$, then as we found, $|\chi\rangle$ will look like $|n_x\rangle\,|n_y\rangle$ (with n_x and n_y describing the occupation of the stretch and in-plane tilt modes). If $\omega_x = \omega_y$, $|\chi\rangle$ will be a 2D semirigid rotor and discussed thoroughly in the following subsection.

The 2D Semirigid Rotor

Now we will explore more thoroughly the special case when $\omega_x = \omega_y$. As written in Equation 7.14, the Hamiltonian for the horizontal modes of the rotor (i.e. the 2-ion system with no pinning) is

$$H = \frac{p_x^2}{2\mu} + \frac{p_y^2}{2\mu} + \frac{3}{2}\mu\omega_\rho^2(\rho - d)^2, \tag{7.15}$$

with $\rho = \sqrt{x^2 + y^2}$.

If we convert to position space and cylindrical coordinates, the momentum terms are now

$$\frac{p_x^2}{2\mu} + \frac{p_y^2}{2\mu} = -\frac{\hbar^2}{2\mu}\left(\frac{\partial^2}{\partial x^2} + \frac{\partial^2}{\partial y^2}\right) = -\frac{\hbar^2}{2\mu}\left(\frac{\partial^2}{\partial \rho^2} + \frac{1}{\rho}\frac{\partial}{\partial \rho} + \frac{1}{\rho^2}\frac{\partial^2}{\partial \theta^2}\right). \tag{7.16}$$

Writing the solution $\psi(\rho, \theta)$ as a separable product $R(\rho)Y(\theta)$, the Schrödinger equation then becomes

$$H\psi = E\psi$$
$$-\frac{\hbar^2}{2\mu}\left(\frac{\partial^2}{\partial \rho^2} + \frac{1}{\rho}\frac{\partial}{\partial \rho} + \frac{1}{\rho^2}\frac{\partial^2}{\partial \theta^2}\right)R(\rho)Y(\theta) + \frac{3}{2}\mu\omega_\rho^2(\rho - d)^2R(\rho)Y(\theta) = ER(\rho)Y(\theta) \tag{7.17}$$

Grouping like terms,

$$\underbrace{\left[\frac{\rho^2}{R}\frac{d^2R}{d\rho^2} + \frac{\rho}{R}\frac{dR}{d\rho} - \frac{2\mu\rho^2}{\hbar^2}\left(\frac{3}{2}\mu\omega_\rho^2(\rho - d)^2 - E\right)R\right]}_{\ell^2} + \underbrace{\left[\frac{1}{Y}\frac{d^2Y}{d\theta^2}\right]}_{-\ell^2} = 0 \tag{7.18}$$

The coordinates ρ and θ have now been separated into the two bracketed terms. They must each be equal to the same constant; therefore, we can set the first term in brackets equal to a constant called ℓ^2 (where ℓ ends up being the angular momentum quantum number) and the second term equal to $-\ell^2$. For Y, this gives

$$Y(\theta) = \frac{1}{\sqrt{2\pi}}e^{i\ell\theta}, \tag{7.19}$$

which are precisely the 2D rotor eigenstates with angular momentum $\hbar\ell$. Solving for R, it is useful to first define

$$u(r) \equiv \sqrt{\rho}R(r) \implies R = \rho^{-1/2}u. \tag{7.20}$$

Inserting this substitution, we obtain

$$-\frac{\hbar^2}{2\mu}\frac{d^2u}{d\rho^2} + \left[\frac{3}{2}\mu\omega_\rho^2(\rho - d)^2 + \frac{\hbar^2}{2\mu}\frac{\ell^2 - \frac{1}{4}}{\rho^2}\right]u = Eu. \tag{7.21}$$

This is a 1D Schrödinger equation in the coordinate ρ, with the original potential modified by the addition of an extra term that indicates a centrifugal potential, which depends on the angular momentum quantum number ℓ. This shows how the radial and angular coordinate coupling manifests: the state of the rotational mode sets ℓ, which in turn modifies the potential for the stretch mode. It is important to note that E in this equation is still the energy of the full horizontal wave function, not just the radial component.

We can gain an intuition for this coupling by expanding around the equilibrium of the radial coordinate. We define our new coordinate $\epsilon = \rho - d$ which is the radial distance from equilibrium. For a well-cooled two ion crystal, the distance the ions move from equilibrium, $\epsilon \approx 30\ nm$ and $d \approx 3\ \mu$m. Therefore, the results of this expansion hold for our crystal. We now expand the Schrödinger equation to first order in ϵ assuming $\epsilon/d \ll 1$:

$$
\begin{aligned}
Eu &= -\frac{\hbar^2}{2\mu}\frac{d^2u}{d\rho^2} + \left[\frac{3}{2}\mu\omega_\rho^2(\rho - d)^2 + \frac{\hbar^2}{2\mu}\frac{\ell^2 - \frac{1}{4}}{\rho^2}\right]u \\
&\approx -\frac{\hbar^2}{2\mu}\frac{d^2u}{d\epsilon^2} + \left[\frac{3}{2}\mu\omega_\rho^2\epsilon^2 + \frac{\hbar^2}{2\mu}\frac{\ell^2 - \frac{1}{4}}{d^2}\left(1 - \frac{2\epsilon}{d}\right)\right]u.
\end{aligned}
\tag{7.22}
$$

Terms with no coordinate dependence are constant energy offsets and can be ignored. Therefore, we redefine

$$
E'_\ell = \frac{\hbar^2(\ell^2 - \frac{1}{4})}{2\mu d^2}.
\tag{7.23}
$$

Substituting this term and regrouping terms,

$$
Eu \approx -\frac{\hbar^2}{2\mu}\frac{d^2u}{d\epsilon^2} + \left[\frac{3}{2}\mu\omega_\rho^2\left(\epsilon^2 - \frac{4E'_\ell}{3\mu\omega_\rho^2 d}\epsilon\right) + E'_\ell\right]u.
\tag{7.24}
$$

Completing the square in ϵ, we finally find that

$$
Eu \approx -\frac{\hbar^2}{2\mu}\frac{d^2u}{d\epsilon^2} + \left[\frac{3}{2}\mu\omega_\rho^2\left(\epsilon - \frac{2E'_\ell}{3\mu\omega_\rho^2 d}\right)^2 + E'_\ell - \frac{2E'^2_\ell}{3\mu\omega^2 d^2}\right]u.
\tag{7.25}
$$

In this we see the Schrödinger of a harmonic oscillator with frequency ω_ρ with an equilibrium diameter that is slightly modified by the rotational state. This is what we expect from a centrifugal force. As ℓ increases, the equilibrium radius of the crystal also increases slightly. Let us call this shift distance $\Delta r_\ell = \frac{2E'_\ell}{3\mu\omega_\rho^2 d}$. Rewriting the equation we have

$$
Eu \approx -\frac{\hbar^2}{2\mu}\frac{d^2u}{d\epsilon^2} + \left[\frac{3}{2}\mu\omega_\rho^2\left(\epsilon - \Delta r_\ell\right)^2 + E'_\ell\left(1 - \frac{\Delta r_\ell}{d}\right)\right]u.
\tag{7.26}
$$

Now we see that the last term in this equation is a constant relative to the coordinates and therefore just offset the energy of the radial wave function by a value which is dependent on ℓ. In this way, we find the energy of the horizontal wave function to be

$$E_{n_\rho,\ell} = n_\rho \hbar \sqrt{3} \omega_\rho + \frac{\hbar^2 \ell^2}{2\mu d^2} \left(1 - \frac{\Delta r_\ell}{d} \right), \tag{7.27}$$

where we drop the 1/4 term from equation 7.23 because it is just a global energy offset. Notice that here we have two separated quantities. A harmonic term that depends on the quantum number n_ρ and another that only depends on the quantum number ℓ. We now attribute these energies to the radial and rotational modes respectively.

7.3 Creating a Rotational Superposition

The goal of our experiment is to be able to create superpositions of rotational states, that is to be able to coherently drive population between rotational states $|\ell\rangle$ and $|\ell + \Delta\ell\rangle$ where $\Delta\ell$ is the change in rotational quantum number. In order to achieve this using our typical S→D optical transitions, we must be able to selectively address specific $\Delta\ell$ optical transitions. In this section, I will describe how we reach this goal.

Optically Resolving Rotational Transitions

From Equation 7.27, we now know the energy of the rotational states is $E_\ell = \frac{\hbar^2 \ell^2}{4mr_e^2} = \hbar\omega_r \ell^2$ where the substitutions $m = 2\mu$ and $r_e = d/2$ have been made and m is the mass of a single calcium atom, r_e is the equilibrium radius of the ion crystal, and ω_r is the fundamental frequency scale of of rotor. This ignores the Δr_ℓ term which is smaller than 10^{-3} for typical experimental parameters. For the experiments in this chapter, $\omega_x = 2\pi \times 845$ kHz, $r_e = 3.13$ μm, and $\omega_r = 2\pi \times 6.43$ Hz. Because our goal is to drive transitions from $|\ell\rangle$ to $|\ell + \Delta\ell\rangle$, we are concerned with the energy difference between these two states which is

$$\Delta E_\ell = E_{\ell + \Delta\ell} - E_\ell = 2\hbar\omega_r \ell \Delta\ell + \hbar\omega_r \Delta\ell^2 \approx 2\hbar\omega_r \ell \Delta\ell. \tag{7.28}$$

The above approximation holds true if $\ell \gg \Delta\ell$ which will be the case in our experiments; $\ell \sim 8000, \Delta\ell \sim 4$.

In a Doppler cooled, non-rotating, thermal state, all rotational transitions are overlapped with each other, independent of the transition order $\Delta\ell$. This is due to the fact that the center of the ℓ distribution, ℓ_0, is 0. In this case, the spectrum is comprised of many lines spaced by only a few Hz ($2\omega_r$, functionally unresolved) and centered around the carrier for all $\Delta\ell$ orders. One can see the overlapping transition in the left panel of Fig. 7.2 which shows the transitions $\Delta\ell = \{0, \pm 1, \pm 2\}$ for a rigid rotor assuming the original occupation of rotational states is a thermal distribution characterized by the Doppler limit of ^{40}Ca$^+$, 0.52 K. This occupation can also be written as a Gaussian where occupation of the initial

state is $P\ e^{\frac{(\ell-\ell_0)^2}{2\sigma_\ell^2}}$ where σ_ℓ is the standard deviation of the distribution and is equal to 920 at the Doppler limit.
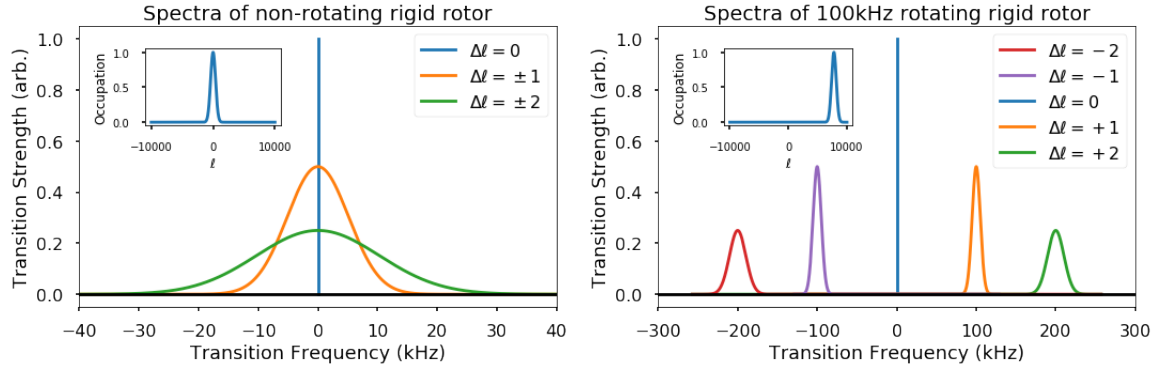
Figure 7.2: Left: Spectrum for a rigid rotor at the Doppler limit in the laboratory frame with an ℓ distribution described as a Gaussian with width $\sigma_\ell = 920$. Right: Spectrum for a state distribution with the same width but spun at $\omega_r = 2\pi \times 100$ kHz. The smaller amplitudes of the higher order transitions is meant to reflect the decrease in density of the spectral lines as the order increases. The amplitude of the line within a given order transition reflects the original ℓ state distribution, shown in insets.

In order to resolve the different rotational transition orders, we created a biased occupation of angular momentum states. If we apply a bias to the initial rotational state so that the ℓ distribution is centered around some larger number $\ell_0 > \sigma_\ell$, we find that that transitions separate according to their order in $\Delta\ell$. Again, this is due to the fact that the transition energy is dependent on the initial state (equation 7.28). We can see this effect in the right panel of Fig. 7.2 which shows the same transitions as its counterpart on the left, but with the crystal rotating at 100 kHz which increases ℓ_0 to 7780. With many ℓ states populated, each individual transition remains unresolved; however, they are now grouped by the order of their transition, $\Delta\ell$. ℓ_0 is calculated by setting the angular momentum from the rotational bias, $I\omega_{rot}$, to the angular momentum of the center rotational state, $\hbar\ell_0$, where ω_{rot} is the angular velocity with which the crystal is rotating.

$$I\omega_{rot} = 2m_{\text{Ca}}r^2\omega_{rot} = \hbar\ell_0 \tag{7.29}$$

$$\ell_0 = \omega_{rot}/2\omega_r \tag{7.30}$$

Intuitively, we can understand the spectral separation of these rotational transitions from the perspective of motional transitions in a harmonic oscillator. We are able to address motional sideband of harmonic oscillators because the oscillation of the particle modulates the frequency of the coupling laser. For a stationary rotor, there is no modulation of the coupling laser. However, if the ring spins with frequency ω_{rot}, the laser frequency will be

modulated at the same frequency thereby generating sidebands at ω_{rot}. If $\omega_{rot} \gg 4\sigma_\ell \omega_r \Delta \ell$, then these sidebands are narrower than the spacing between them, allowing us to resolved and address them individually.

Preparing a Rotating Ion Crystal

In order to achieve the resolved rotational transitions described in the previous subsection, we must first make the in-plane potential rotationally symmetric and then create an ion crystal that has a well-defined rotation in that potential.

Rotational symmetry is broken in our system by stray in-plane quadrupoles. One can compensate these using the eight DC electrodes on the trap. We do this by minimizing the frequency of the in-plane tilt mode which has a frequency of $\sqrt{\omega_y^2 - \omega_x^2}$. If the quadrupoles are compensated, $\omega_x = \omega_y$ and the in-plane tilt mode becomes the zero frequency rotational mode. Using the DC electrodes, we can reduce the frequency of the in-plane tilt mode to < 10 kHz which means that any residual potential is much less than the rotational energy of the ring at rotating at 100 kHz, our typical operating parameter.

With the potential compensated, we now must prepare a rotating ion crystal. State preparation of ions in traps with degenerate trap frequencies can be challenging because motional modes can become orthogonal to cooling lasers. Thus we begin our experiments by intentionally breaking the symmetry with a static in-plane quadrupole. In order to do this, voltages $V_0 \cos(\phi_0 + \phi_i)$ are applied to each electrode where ϕ_i shifts by $\pi/4$ relative to its counterclockwise neighboring electrode as shown in Fig. 7.3. For $V_0 = 5$ V, the ion crystal is pinned with a in-plane tilt mode of 280 kHz and whose orientation which is tunable via ϕ_0. In this configuration, state preparation sequences such as Doppler cooling and sideband cooling are done in the same way that they are done for typical ion crystals.

With the ions pinned and cooled, the phase of the in-plane quadrupole, ϕ_0, is ramped in such a way that the angular orientation of the quadrupole is accelerated to an angular velocity of 100 kHz in 50 μs. The rotating orientation of the quadrupole causes the ions to accelerate and rotate along with it. Fig. 7.3 shows how the quadrupole changes with the applied voltages. The spin up time of 50 μs is near the adiabaticity limit imposed by the requirement that we do not want the ion wave function to become significantly displaced from its equilibrium position as compared to the size of the ground state wave function a_0. From this we find the adiabaticity condition $\dot{\omega}_{\text{rot}} \ll \omega_x^2 a_0 / 2 r_e$ where r_e is the radius of the ring. After reaching the target angular velocity, the quadrupole continues to rotate at the final speed and the amplitude is reduced to zero over a time span of 1 ms. When the rotating quadrupole is totally turned off, conservation of angular momentum keeps the ions spinning but they now do so in the desired symmetric potential. From numerical calculations, we find that the release time of 1 ms is not adiabatic as the in-plane tilt mode maps into the zero frequency rotational mode and adiabaticity is lost close to the release point. The release time of 1 ms is chosen as an experimentally convenient time scale when the release is still mostly adiabatic. A small amount of diabatic release just before free rotation will give us a slightly larger value for σ_ℓ though it should only change by factors of order unity.
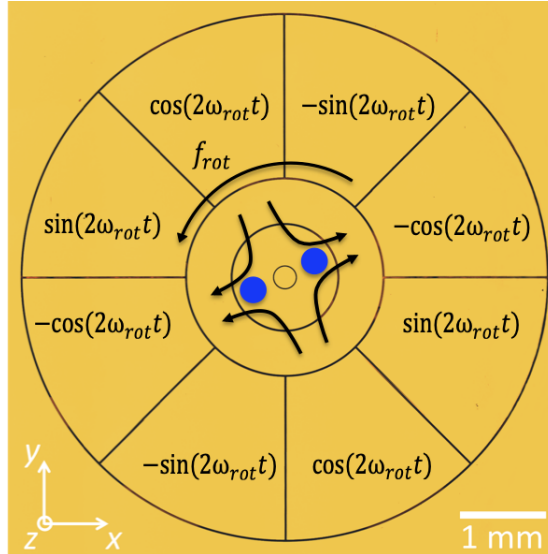
Figure 7.3: Image of the trap with the voltages used to create the rotating quadrupole labeled on the DC electrodes. The quadrupole they create and the ions' orientation relative to that quadrupole are also shown.

The Rotation Circuit

In this subsection, I will describe the circuit we use to generate the required rotation of the electric quadrupole potential.

The voltages are first sourced by a Keysight 33500B arbitrary waveform generator (AWG). Before the experiment, the AWG is programmed with a waveform that includes an initial phase, ϕ_0, a frequency ramp, and an amplitude ramp. Then, at the start of each experiment, the AWG is triggered. The amplitude starts high with phase ϕ_0 and stationary (Stage 1, Fig. 7.4). After state preparation, the frequency ramps to the final frequency during the spin-up interval (Stage 2), then the amplitude ramps down to zero during the release interval (Stage 3) and remains there until triggered again (Stage 4). This sequence is shown in Fig. 7.4.

We need a circuit that can produce four pairs of phase coherent voltages shifted relative to one another by 90°. To achieve this we use two outputs of the AWG phase shifted relative to one another by 90°. These two channels are then each fed into unity gain inverters which shift the signal by 180°. Precision 10 kΩ resistors are used to make sure the gain is precisely unity for both inverters. In this way the two original signals and the two inverted signals give us our required outputs. These four signals can be split again to produce the pairs of voltages that are applied to the electrodes. Fig. 7.5 shows the schematic of the inverter circuit used.

The inverter circuit generates the voltages necessary to create the rotating quadrupole; however, we still want to be able to apply compensation voltages to the DC electrodes to correct for any stray fields present at the trapping location. Therefore, for each channel we
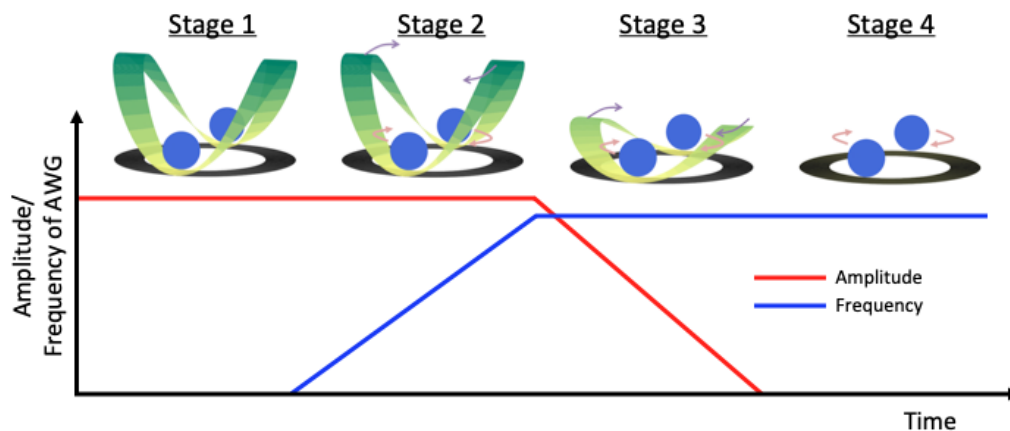
Figure 7.4: Frequency and amplitude of the signal produced by the AWG throughout rotation preparation and a cartoon of the behavior it creates in the ion crystal at each stage.
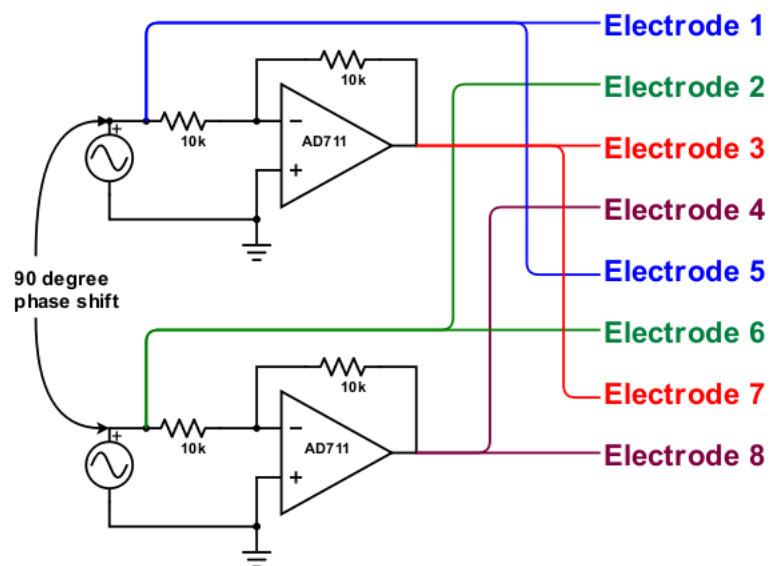
Figure 7.5: Schematic of the inverter circuit which takes the AWG outputs and produces the eight voltages going to the electrodes.

need to add the signal from the inverter circuit to the compensation voltage from the DAC which is used to compensate stray fields. In order to do this, the DAC voltage is first fed through a buffer which makes the circuit insensitive to the output impedance of the DAC. Then both voltages are fed into a op-amp which is configured to add the voltages together and pass them onto the next stage of the circuit. Fig. 7.6 shows the schematic for one of the eight channels adder channels.
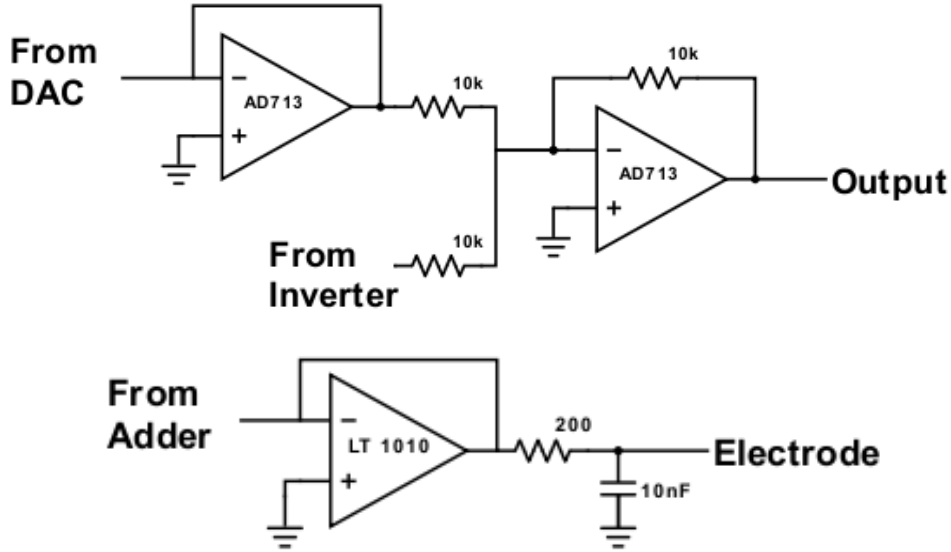
Figure 7.6: Top: Schematic of one channel of the adder circuit which takes signal from the inverter and adds it to the signal from the DAC. Bottom: Schematic of one channel of the buffer circuit which amplifies the current from the rotation circuit and outputs a voltages that goes directly to the electrodes.

The final stage of the rotation circuit is a set of high-current buffers for each channel. In order to reduce noise on the compensation electrodes, there are large 10 nF capacitors in vacuum next to the electrodes. We aim to apply 5 V at 200 kHz (twice $\omega_{\rm rot}$) to these electrodes. At that frequency, the in-vacuum capacitors have an impedance of 80 Ω, so the circuit needs to be able to drive about 100 mA. In order to achieve this, each channel is fed through a high current buffer (LT 1010) that copies the voltage output by the adder circuit but can source up to 150 mA of current. For filtering purposes, we also have 200 Ω resistors forming a low pass filter with the in vacuum capacitors. This gives us a cutoff frequency around our rotation frequency such that we can still apply the rotation voltages but noise above the frequency is attenuated. Fig. 7.6 shows the high current buffer circuit schematic.

7.4   Observing Rotational Transitions

In order to observe a three micron radius crystal rotating at 100 kHz with a laser propagating parallel to the rotation plane we need to overcome the fact that the laser has significant coupling with many different $\Delta\ell$ transitions. In order to see exactly why this is and how we might overcome it, consider the coupling between the states $|\ell\rangle$ and $|\ell + \Delta\ell\rangle$:

$$
\begin{aligned}
\langle \ell + \Delta\ell | e^{ik_x x} | \ell \rangle &= \langle \ell + \Delta\ell | e^{ik_x r_e \cos\phi} | \ell \rangle \\
&= \frac{1}{2\pi} \int_0^{2\pi} d\phi \; e^{-i(\ell+\Delta\ell)\phi} e^{ik_x r_e \cos\phi} e^{i\ell\phi} \\
&= \frac{1}{2\pi} \int_0^{2\pi} d\phi \; e^{i(k_x r_e \cos\phi - \Delta\ell\phi)} \\
&= J_{\Delta\ell}(k_x r_e)
\end{aligned}
\tag{7.31}
$$

where k_x is the projection of the wavevector of the laser in the x direction in the plane of the rotor, ϕ is the angle the laser makes with the x axis, θ is the polar angle made with the axis normal to the rotor plane, and $J_{\Delta\ell}$ is a Bessel function of the first kind. If $\theta = \pi$, i.e. a parallel beam, the transition strength is spread from $\Delta\ell = -30$ to 30, as shown in the left plot of Fig. 7.7. This coupling distribution can be understood classically as the maximum Doppler shift of an ion at a radius of 3 µm rotating at 100 kHz is about 2.6 MHz, the frequency of the 26th order sideband. If many ℓ states are occupied, characterized by a standard deviation σ_ℓ, the standard deviation of each line in frequency space is $2\omega_r \Delta\ell\sigma_\ell$. This means that eventually the high order transitions are no longer resolved. For a rotational mode cooled to the Doppler limit, the modes are unresolved after 4th order. Finally, with Doppler shifts on the order of a few MHz, one runs the risk of addressing other motional and optical transitions present in $^{40}\text{Ca}^+$ which are also spread over several MHz. This issue can be solved by addressing the ring from a steeper angle. At 10° from vertical, the laser couples to many fewer lines making them much easier to address individually as shown in the right panel of Fig. 7.7.
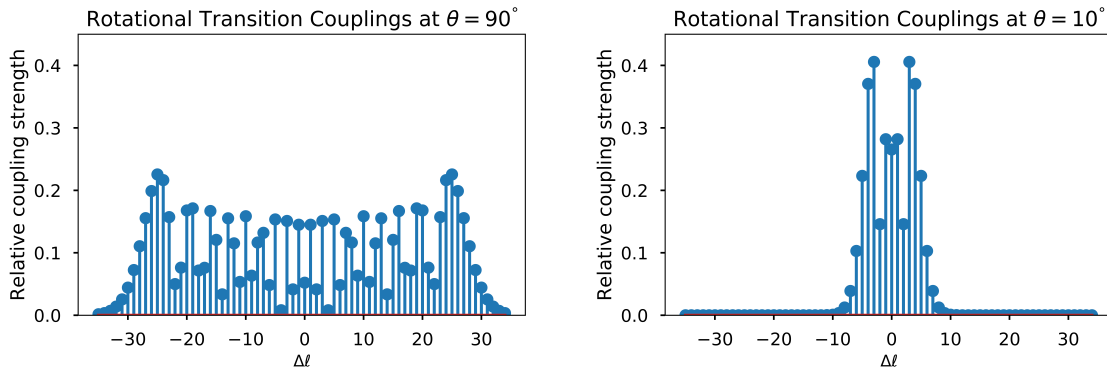
Figure 7.7: Left: Calculated coupling strengths between $|\ell\rangle$ and $|\ell + \Delta\ell\rangle$ for a spectroscopy laser in the plane of rotation. Right: Couplings between the same transitions for a laser 10° from vertical.

We can experimentally observe these transitions by scanning the laser frequency over the $|S\rangle \to |D\rangle$ transition of an ion ring rotating with 100 kHz. Fig. 7.8 shows such a spectrum

and that we do indeed observe sidebands at integer multiples of 100 kHz. We can also fit the observed spectra based on our expected couplings from Equation 7.31 for the laser angle. One can see that the experimentally observed spectrum (black) fits very well with the predicted spectrum (red) for an angle of the coupling beam with respect to the vertical of 7.56°.
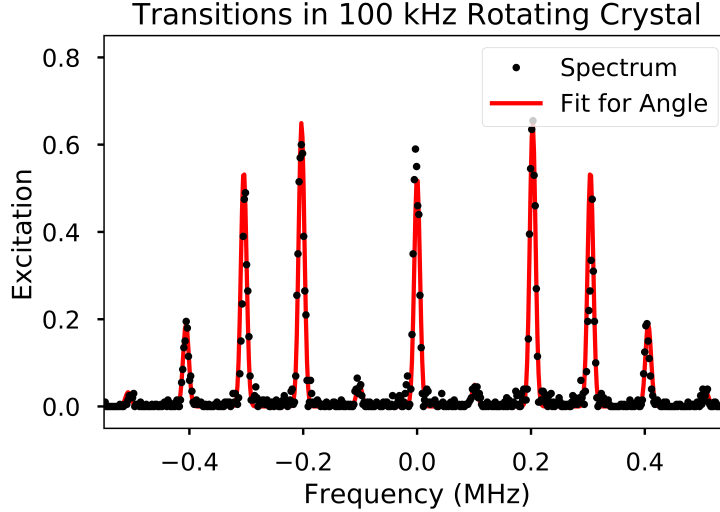
Figure 7.8: Observed spectrum of the ion crystal rotating at 100 kHz (black) and the predicted spectrum for a laser angle yielding 7.56 degrees from vertical (red).

7.5 Coherent Operations

We now consider the dynamics of population evolution between the states $|\ell\rangle$ and $|\ell + \Delta\ell\rangle$.

For rotational sidebands, the size of the coupling matrix element between angular momentum states $\langle \ell + \Delta\ell | e^{-ikx} | \ell \rangle$ is independent of ℓ and therefore the Rabi frequency is independent of ℓ, according to Equation 7.31. This is in contrast to harmonic degrees of freedom where the transition matrix element $\langle n + \Delta n | a | n \rangle$ depends on the initial Fock state, n. For finite temperatures, the dependence of the harmonic oscillator Fock state Rabi frequency of n will lead to a dephasing of sideband Rabi oscillations. On the other hand, the energy between angular momentum states $E_{\ell+\Delta\ell} - E_\ell$ depends on the initial state due to the nonlinearity of the energy in ℓ. Therefore, operations on rotational sidebands of superpositions or mixtures of angular momentum eigenstates are the weighted sum of Rabi oscillations, each with slightly different detunings:

$$P(\mathrm{D}) = \sum_\ell |c_\ell|^2 \frac{\Omega^2}{\Omega^2 + \delta_\ell^2} \sin^2\left(\frac{1}{2}\sqrt{\Omega^2 + \delta_\ell^2}t\right). \tag{7.32}$$

Here, $P(\text{D})$ is the probability of the ions respectively being excited to the $|D\rangle$ state, c_ℓ is the probability amplitude of the ion initially occupying the rotational state $|\ell\rangle$, Ω is the resonant Rabi frequency, $\delta_\ell = 2\omega_r(\ell_0 - \ell)\Delta\ell$ (equation 7.28) is the detuning of the ℓth state assuming the laser is resonance with the center of the distribution, ℓ_0, and t is time. Because we are globally addressing two ions, $P(|D\rangle) = P(|DD\rangle) + 0.5P(|DS\rangle) + 0.5P(|SD\rangle)$ and will in the future be referred to as the 'excitation' as it is the probability of exciting the addressed ions. Unlike sideband operations on harmonic oscillator modes, we find that the shape of the Rabi oscillation will be affected by the relative size of σ_ℓ and Ω. The width of a rotational line in energy space is $\gamma_\ell = 2\omega_r\Delta\ell\sigma_\ell$. If $\Omega \gg \gamma_\ell$, rotational transitions for all occupied states are effectively on resonance and the Rabi oscillation can be observed with high contrast. However if this is not the case, the contrast of the Rabi oscillation is reduced. Therefore, we can extract the width of the line γ_ℓ, and through it σ_ℓ, by fitting the experimental data with a model according to equation 7.32. For the rest of this thesis, I will assume that the occupation of angular momentum states is Gaussian distributed around an expectation value ℓ_0 with a standard deviation σ_ℓ. This is a reasonable assumption as a Boltzmann distribution in energy space has the form of a Gaussian in quantum number space if the energy goes as the quantum number squared as it does for angular momentum states. For this analysis, the exact functional form of the distribution is not critical, though the center and qualitative measure of width are. Fig. 7.9 shows Rabi oscillations on the first order rotational sideband taken for different Rabi frequencies for the same ℓ distribution. Notice the reduced contrast of the slower flops. The fit parameters given in the legend indicate the fit Rabi frequency, Ω. Fitting these Rabi oscillations returns similar distributions widths in frequency of $\gamma_\ell = 2\pi \times 8.0$ kHz and 8.8 kHz respectively. In quantum number space, this corresponds a standard deviation of angular momentum states of $\sigma_\ell = 310$ and 342 respectively.

The magnitude of σ_ℓ is affected by the occupation of the in-plane tilt mode before spin-up. When the crystal is released, the tilt mode maps into the zero frequency rotational mode. Numerical simulations using QuTiP [21] that assumes a linear voltage release suggest that for initial preparation with Doppler cooling and a voltage ramp that is linear in time, $\sigma_\ell \approx 250$ is expected as shown on the left in Fig. 7.10. This is close to our observed σ_ℓ shown on the right in Fig. 7.10.

Driving high contrast coherent operations on higher order sidebands is more difficult as the detuning width of the line grows linearly with $\Delta\ell$ for a given σ_ℓ. The blue curve in the right plot of Fig. 7.9 shows Rabi oscillations for $\Delta\ell = 4$ when all modes are only Doppler cooled before spin up. The fit indicates $\sigma_\ell = 442$ and has poor contrast. We can improve the contrast by reducing σ_ℓ by sideband cooling the in-plane tilt mode (280 kHz) to the ground state before spin up. Because this state maps to the rotational state, we ultimately reduce the spread in energy in the rotational mode after release. The red curve on the same plot shows the Rabi oscillation when the in-plane tilt mode is ground state cooled before rotation. It is much higher contrast and fits an ℓ distribution of $\sigma_\ell = 46$, nearly an order of magnitude improvement. Numerical simulations of the release dynamics (Fig. 7.10) indicate this is close to the minimum achievable σ_ℓ with a linear release of one millisecond.
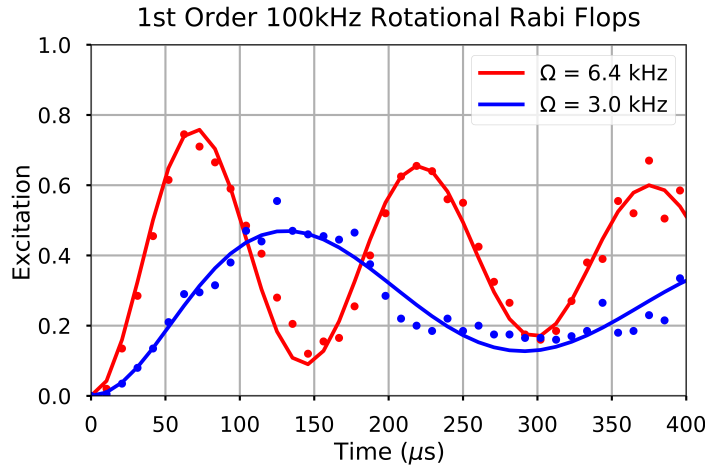
Figure 7.9: Rabi oscillations performed on the first order rotational sideband of a 100 kHz rotating crystal. The two curves are measured with different laser powers but the same rotation preparation. Ω indicates the fit Rabi frequency.
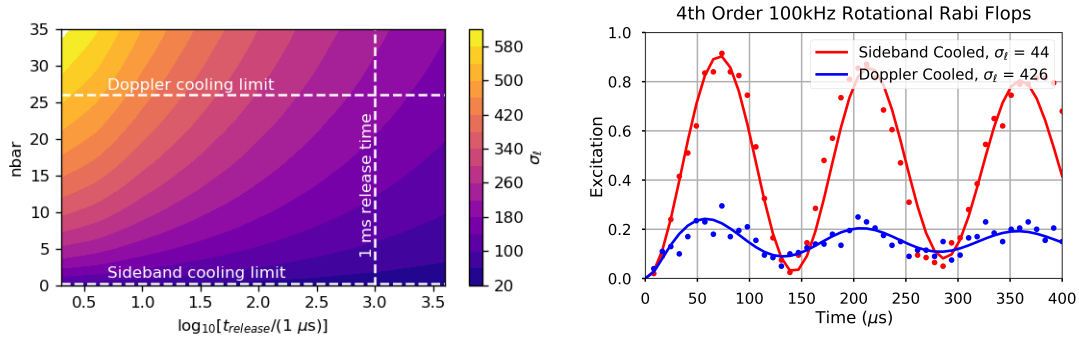
Figure 7.10: Left: Heat map of how the initial occupation of the in-plane tilt mode maps onto σ_ℓ as a function of release time. Doppler cooling limit, sideband cooling limit, and our typical release time of 1 ms are indicated with dashed lines. Right: 4th order rotational Rabi oscillations. Both oscillations are performed with the same laser intensity and rotation preparation. Doppler cooling (blue) gives $\sigma_\ell = 422$ while sideband cooling of the in-plane tilt mode (red) before spin up gives $\sigma_\ell = 46$.

Having established high-quality Rabi oscillations, let us now consider Ramsey style experiment on one of the rotational sidebands. Driving a $\pi/2$ pulse on one of these rotational sidebands from the initial state $|\Psi(0)\rangle = \sum_\ell c_\ell |SS, \ell\rangle$ and waiting produces the following superposition:

$$\begin{aligned}
|\Psi(t)\rangle = \sum_\ell c_\ell [& |SS, \ell\rangle \\
& + e^{-2i\omega_r(\ell-\ell_0)\Delta\ell t}(|SD, \ell + \Delta\ell\rangle \pm |DS, \ell + \Delta\ell\rangle) \\
& + e^{-4i\omega_r(\ell-\ell_0)\Delta\ell t}|DD, \ell + 2\Delta\ell\rangle].
\end{aligned} \tag{7.33}$$

The sign between the SD and DS terms is negative if $\Delta\ell$ is odd and positive in order to preserve the parity of the wave function (see Section 8.3 for more information). The dynamics of the evolution of this superposition can be understood by considering individual manifolds corresponding to a single initial ℓ-state that each acquire phase at their own rate. This means that if we apply a second $\pi/2$ pulse some time later, we expect a loss of contrast at rate $\gamma_\ell = 4\omega_r\ell\Delta\ell/\sigma_\ell$ which is the width of the line in frequency space as the fringes of each superposition beat against one another. Fig. 7.11 shows Ramsey experiments on the first and fourth order rotational sidebands for the same state preparation. We fit these curves to extract σ_ℓ and the overall detuning Δ with no extra decay factor included. The decay is predicted only from the beating of different manifolds of angular momentum eigenstate superpositions against each other. As expected, the fourth order superposition dephases four times as quickly as the first order. Fitting the data returns $\gamma_\ell/\Delta\ell = 1.10 \pm 0.03$ kHz and agrees well for both curves. This corresponds to $\sigma_\ell = 42.7 \pm 1.3$ which is also consistent with the observed Rabi oscillations.
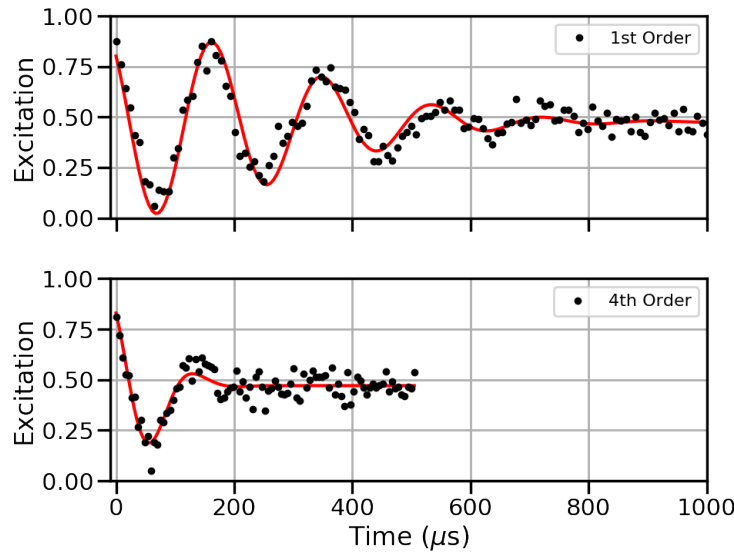
Figure 7.11: Ramsey experiment run on rotational sidebands for $\Delta\ell = 1$ and $\Delta\ell = 4$. Overall detuning of 6 kHz. Simultaneous fits to both cures (red) are made with σ_ℓ and an overall detuning for each curve as free parameters. Not term for decoherence is included. State preparation was the same for both of these scans.

   The qualitative behavior of the Ramsey experiment can also be understood in the spatial domain. After driving a $\pi/2$ pulse, three rotational states exist where each one is rotating $\Delta\ell \times 6.43$ Hz or $2\Delta\ell \times 6.43$ Hz faster than the others. Therefore, once the ions have traveled far enough to become spatially separated, one expects the contrast to vanish as they are no longer able to interfere spatially. Additionally, if σ_ℓ is large, the momentum uncertainty is large so the spatial uncertainty should be low. For low spatial uncertainty, it is expected that the wave packets should separate more quickly which is indeed what we see for large values of σ_ℓ.

Chapter 8

Investigating Indistinguishability with a Rotational Interferometer

In this chapter I will discuss a proposed experiment to demonstrate the indistinguishability of two well-separated ions in a Paul trap. I will begin with a motivation section and a section on how a rotational interferometer could investigate particle indistinguishability. Then I will present a mathematical description of the momentum states which an ion ring can occupy and reflect on how the exchange symmetry can restrict which momentum states can be occupied under certain conditions. Then I describe a way in which we can spectroscopically detect missing angular momentum eigenstates using a rotational interferometer and the signal we expect from such a system if indeed the particles are indistinguishable. With the experiment laid out, I then describe our experimental efforts to create a system which is stable enough to observe the expected signal. Finally, I reflect on the coherence time of our rotational superpositions which at this point is much worse than expected from any potential decoherence source that we have identified.

8.1   Motivation

Indistinguishability is a concept ubiquitous to quantum physics. It is a core assumption necessary to explain numerous phenomena from electronic energy levels in atoms (ortho/parahelium) [67], orbital hybridization in molecules [68], and the rotation of diatomic nitrogen [69], to the behavior of Bose-Einstein condensates [70] and the stability of neutron stars [71]. The notion of fermions and bosons in our standard model hangs on the axiom that not only are the properties of every electron the exact same, but there is only one electron field which localizes in places where we observe electrons [72]. We are comfortable with this idea in settings such as Bose-Einstein condensates and neutron stars when the consequences of indistinguishably are clear and qualitatively affect the behavior of the systems [70, 71]. However these are very large systems and the idea of single particles as we know them classically is totally lost, particularly evidenced in the use of language like

'Fermi Sea'. Alternatively, we can think of two indistinguishable electrons orbiting a Helium nucleus or even two indistinguishable nitrogen atoms forming a molecule [67, 69]. Here, indistinguishability affects the energy structure of the system, however these systems are so small that individual control of these particles is near impossible so again the idea of a classical particle seems far removed.

Now consider two $^{40}Ca^+$ ions trapped in a Paul trap. The ions form a crystal due the competing affects of the harmonic trap and their mutual Coulomb repulsion. They remain well separated at all times at a distance of about 6 μm. Because of this well-defined separation, it is easy to talk about one ion being on the left and another being on the right. In position space, this is a system we are happy to think about classically. However, it remains that these are two identical calcium ions without any distinguishing features and formally they should be considered indistinguishable. In the experiment described in this chapter, we aim to observe signatures of this indistinguishability demonstrating that even in this 'classical' well-separated system, 'particles' are still totally indistinguishable.

When we consider classical particles, it is tempting to write the wave function of a two ion crystal as

$$\Psi(x_1, x_2) = \Phi_1(x_1)\Phi_2(x_2) \tag{8.1}$$

where $\Phi_1(x_1)$ describes the spatial wave function of ion on the left and $\Phi_2(x_2)$ describes the spatial wave function of the ion on the right. This approximation captures much of the physics necessary to describe the behavior of ion chains. However, if the ions are identical, that means strictly that Ψ must satisfy

$$\Psi(x_1, x_2) = \pm\Psi(x_2, x_1) \tag{8.2}$$

Therefore, Ψ would be better written as

$$\Psi(x_1, x_2) = \Phi_1(x_1)\Phi_2(x_2) \pm \Phi_1(x_2)\Phi_2(x_1) \tag{8.3}$$

where Φ_1 is the spatial wave function for an ion localized on the left, and Φ_2 is the spatial wave function for an ion localized on the right, but x_1 is the cooridnates of quantum particle 1, and x_2 the coordinates of particle 2. This means that each 'particle' (i.e. object in spatial locations Φ_1 and Φ_2) is in fact a superposition of two *quantum mechanical particles* (i.e. 'coordinates', x_1 and x_2), and demonstrates that in classical to quantum cross over, the word 'particle' is inherently misleading [73].

8.2 A Rotational Interferometer

Experiments probing the indistinguishability of ions have been proposed previously [55]. Here we present a new protocol that highlights the strengths of the ring trap laid out in the previous chapters. Our proposed experiment is to run a Ramsey style rotational interferometer to demonstrate the indistinguishability of calcium ions in a Paul trap. The formal

presentation will come in the following section but for now let us think broadly. If the two
ions are truly identical, we should be able to interfere them with each other as one would
interfere an atom with itself. A great way to do this would be to perform a particle exchange
operation in real-space, or more precisely to create a coherent superposition of 'exchanged'
and 'non-exchanged' states. We will achieve this through a Ramsey experiment where we
place the collective motion of a 2-ion system into a superposition of rotational states where
one arm of the superposition is rotating relative to the other, as already described in chapter
7. By waiting the appropriate amount of time, we can recombine arms in an exchanged
configuration and read out the interference signal.

Fig. 8.1 illustrates this procedure. In panel (1), the ions begin totally anti-correlated with
one another in position space in a rotor potential. In (2), a $\pi/2$ pulse on a rotational sideband
creates a superposition of motional modes, which is to say an interferometer where one branch
is rotating faster than the other. (3-4) The two branches of the interferometer separate but
then begin to recombine as the periodic boundary conditions bring them back together. (5)
At a specific time, the atoms realign into an exchanged orientation. (6) A second $\pi/2$ pulse
recombines the arms and if the ions are truly indistinguishable, an interference signal can be
read out.
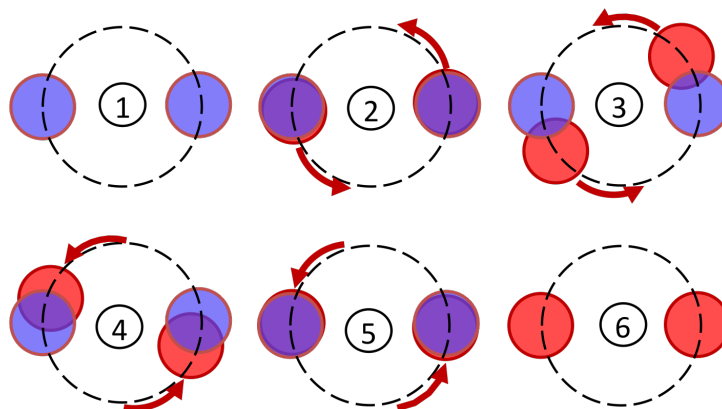
Figure 8.1: Sketch of the rotational interferometer proposed.

In the following section I will formally define this problem in terms of symmetries and
momentum states.

8.3   States and Exchange Symmetry

For this experiment, we will used the same system described in Chapter 7. In Section 7.2,
we managed to separate the Hamiltonian into a piece which depends only the center-of-mass
coordinate $\mathbf{R}$ and the relative coordinate $\mathbf{r}$. Under exchange of the two ions' coordinates,
$\mathbf{r}_1 \leftrightarrow \mathbf{r}_2$, $\mathbf{R} \to \mathbf{R}$ and $\mathbf{r} \to -\mathbf{r}$. Therefore a particle exchange operation does not affect the
parity of the center-of-mass modes and flips the parity of the relative modes. We can look

into the eigenstates of the relative modes to evaluate further how an exchange operation
affects them.

The regime of interest for us is when $\omega_x = \omega_y$. From Equation 7.15, if $\omega_{\text{rot}} \ll \omega_\rho$ the
relative horizontal Hamiltonian of system is then

$$H = \left[\frac{L_\theta^2}{2\mu r_e^2} + \frac{p_\rho^2}{2\mu} + \frac{3}{2}\mu\omega_\rho^2\rho^2 \right]. \tag{8.4}$$

where we have moved to polar coordinates so $p_x^2 + p_y^2 = p_\rho^2 + L_\theta^2/r_e^2$ where p_ρ is the momentum
in the radial direction and L_θ is the angular momentum in the plane.

This is analogous to a particle of mass μ trapped in a Mexican hat potential of frequency
$\sqrt{3}\omega_\rho$ and radius r_e. In the radial direction we have a harmonic oscillator with frequency
$\sqrt{3}\omega_\rho$ and in the angular direction a rigid rotor that has eigenfunctions that look like $\propto e^{i\ell\theta}$
where ℓ is the angular momentum quantum number and goes from $-\infty$ to ∞.

The eigenfunctions of harmonic oscillators are composed of Hermite polynomials [67]
which for odd quantum numbers are comprised of odd powers of the coordinate and for
even quantum number even powers of the coordinate. Therefore, for harmonic oscillators of
relative modes, if the quantum number is even, the wave function is even under exchange
because **r** is always raised to an even power. However, if the quantum number is odd, the
exchange is odd for the reciprocal reason. From this we extract the idea that as relative
modes increase in quanta by one, their exchange symmetry changes.

For the rotor wave functions, $e^{i\ell\theta}$, exchange is equivalent to sending $\theta \to \theta + \pi$. In this
way we see too that if ℓ is even, the exchange of the wave function returns the same wave
function and if ℓ is odd, the wave function picks up a minus sign. In this way it possess the
same exchange rules as the harmonic oscillator relative modes described above.

This alternation of the symmetry is exactly what we would like to utilize in this experi-
ment. Now that we have fully laid out the motional eigenfunctions of the system, an energy
eigenstate of total 2-ion system may be written as

$$|\Psi\rangle = |SS\rangle |N_x\rangle |N_y\rangle |N_z\rangle |n_z\rangle |n_s\rangle |\ell\rangle \tag{8.5}$$

taking for now the electronic state to be $|SS\rangle$ for simplicity, and assigning a quantum number
to each of the 6 motional degrees of freedom where n_z and n_s and the quantum number of the
vertical and radial harmonic oscillator relative modes respectively. If we write the exchange
operator as $\hat{P}$, then the exchanged state becomes

$$\hat{P}|\Psi\rangle = (-1)^{n_z}(-1)^{n_s}(-1)^\ell |SS\rangle |N_x\rangle |N_y\rangle |N_z\rangle |n_z\rangle |n_s\rangle |\ell\rangle \tag{8.6}$$

The system eigenfunction $|\Psi\rangle$ is also an eigenfunction of the exchange operator $|\Psi\rangle$, with
eigenvalue ± 1 depending on whether $n_z + n_s + \ell$ is even or odd. Since ^{40}Ca$^+$ contains 20
neutrons, 20 protons, and 19 electrons, it is a fermion and therefore its wave functions must
satisfy

$$\hat{P}|\Psi\rangle = -|\Psi\rangle \tag{8.7}$$

which means that *only eigenstates for which $n_z + n_s + \ell$ is odd are allowed.* Note that this is only true if the electronic state is $|SS\rangle$, or more generally, if it is even under exchange (in a "triplet state" in the language of spin). The opposite is true if in the singlet state $|SD\rangle - |DS\rangle$. In the general case, the quantum numbers n_z, n_s, and ℓ may individually take on any value, as long as their sum is odd. As an example, an allowed state (for these degrees of freedom) would be $\frac{1}{\sqrt{3}}(|0, 0, 1\rangle + |4, 7, 2\rangle + |1, 100, 0\rangle)$.

Now imagine that we prepare the ion in the ground state of the two harmonic relative modes and the electronic ground state. In this case, all degrees of freedom except the rotational mode have even parity: $n_z = n_s = 0$, so ℓ *must* take on only odd values in order to make the 2-ion state antisymmetric under exchange. In other words, the antisymmetric quality must be fully captured in the rotational mode and only odd rotor states can be occupied. So, if we can show that half the rotor states are unoccupied, we effectively show that the two ions are indistinguishable from one another and obey exchange symmetries. If we could show that the occupied states are odd, we could further show that the ions are fermions.

8.4 Spectroscopic detection of momentum state occupation

In order to demonstrate the indistinguishability of our calcium ions, our goal is now to observe missing angular momentum states when the ion is prepared in the ground state of all other relative modes. In order to do this, our proposal is to create a superposition of angular momentum states and observe how they interfere with each other as the system evolves. To see how this is relevant we must first consider the energy levels present in the rotational mode and how they can be used to probe which ones are missing.

In Section 7.2 we derived the energy between rotational states to be $\Delta E_\ell \approx 2\omega_r \ell \Delta \ell$. From this, we can see that unlike the harmonic oscillator, the difference between the rigid rotor's energy levels are not independent on its quantum number. Therefore, superposition of $|\ell\rangle + |\ell + \Delta \ell\rangle$ will gather phase at a rates dependent of ℓ. If such a superposition is created with several ℓ states occupied, the system will dephase due to the presence of many different frequencies as shown by the Ramsey experiments presented in Fig. 7.11. The superposition created by a $\pi/2$ pulse on a rotational sideband was found in Equation 7.33 and is repeated here for convenience:

$$
\begin{aligned}
\Psi = \sum_\ell c_\ell [& |SS, \ell\rangle \\
& + e^{-2i\omega_r(\ell - \ell_0)\Delta \ell t}(|SD, \ell + \Delta \ell\rangle \pm |DS, \ell + \Delta \ell\rangle) \\
& + e^{-4i\omega_r(\ell - \ell_0)\Delta \ell t}|DD, \ell + 2\Delta \ell\rangle].
\end{aligned}
\tag{8.8}
$$

As discussed in Section 7.5, each term in the sum will gather phase at a rate of $2\omega_r \ell \Delta \ell t$. Because the phase accumulation depends on ℓ, the phase of the superposition for each term in the sum will quickly become out of sync with one another. Despite this scrambling, all rotational eigenstates accumulate a phase of $2\pi\ell$ at a time of

$$t_{\text{revival}} = \frac{4\pi\omega_r}{\Delta\ell} = \frac{1}{12.8 \text{ Hz} \times \Delta\ell}. \tag{8.9}$$

Since ℓ is necessarily an integer, all terms in the sum will have the same phase modulo 2π at the revival time, independent of the original ℓ state. Moreover, at $nt_{\text{revival}}/2$, each superposition will have gained a phase of $\pi\ell$. Therefore, if the system only possessed even angular momentum states, we would get the revival condition not only at nt_{revival} but also $t_{\text{exchange}} = \frac{2n-1}{2}t_{\text{revival}}$ where n is an integer because now not only is ℓ and integer, but so is $\ell/2$. If it is only the odd states that are populated, we still get a revival at t_{exchange}, however, now each term in the sum has a phase of π rather than 2π at the exchange times. This extra revival occurs because if half the states are missing, then the separation between the momentum states is now 26 Hz rather than 13 Hz so revivals occur twice as fast. This early revival at t_{exchange} will be our signature for indistinguishability as it only appears given the exclusion of half the momentum states which only occurs if the system has a well defined exchange symmetry between the two ions.

Calculation of Expected Interference Signal

In this subsection we formally lay out the rotational superposition evolution and calculate the expected signal mapped onto the optical qubit. In Chapter 7 we already described how we can create the superposition of rotational states entangled with the ions' electronic state.

Both ions initially begin in the internal state $|S\rangle$, and, for simplicity, let us assume they are in a rotational eigenstate $|\ell\rangle$. If we turn on a laser tuned to the $\Delta\ell$ sideband of the $|S\rangle \to |D\rangle$ transition, then we create an effective 4-level system $\{|SS, \ell\rangle, |SD, \ell + \Delta\ell\rangle, |DS, \ell + \Delta\ell\rangle, |DD, \ell + 2\Delta\ell\rangle\}$. For a coupling strength Ω, Fig. 8.2 shows the level diagram. Note that the electronic energies have been subtracted out.

The Rabi frequencies for coupling $|S\rangle$ to $|D\rangle$ for ion 1 and ion 2 may have the same or different signs, depending on whether $\Delta\ell$ is even or odd (same if even, opposite if odd). This comes from exchange symmetry argument; an odd $\Delta\ell$ transition changes the rotational exchange symmetry and therefore must also change the electronic exchange symmetry.

So having worked out the 4-level system and its couplings, we can write out the Hamiltonian for this system as a matrix in the basis $\{|DD, \ell + 2\Delta\ell\rangle, |DS, \ell + \Delta\ell\rangle, |SD, \ell + \Delta\ell\rangle, |SS, \ell\rangle\}$

$$H_\ell = \begin{pmatrix} -\delta'_\ell & (-1)^{\Delta\ell}\frac{1}{2}\Omega e^{-i\phi} & \frac{1}{2}\Omega e^{-i\phi} & 0 \\ (-1)^{\Delta\ell}\frac{1}{2}\Omega e^{i\phi} & 0 & 0 & \frac{1}{2}\Omega e^{-i\phi} \\ \frac{1}{2}\Omega e^{i\phi} & 0 & 0 & (-1)^{\Delta\ell}\frac{1}{2}\Omega e^{-i\phi} \\ 0 & \frac{1}{2}\Omega e^{i\phi} & (-1)^{\Delta\ell}\frac{1}{2}\Omega e^{i\phi} & \delta_\ell \end{pmatrix} \tag{8.10}$$
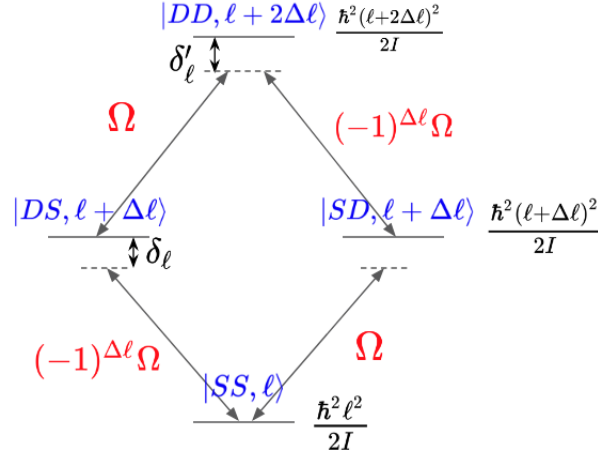
Figure 8.2: Energy levels participating in rotational Ramsey experiment.

where ϕ is an arbitrary laser phase, δ_ℓ is the detuning of the laser from the $|\ell\rangle$ to $|\ell + \Delta\ell\rangle$ transition and δ'_ℓ the detuning of the laser from $|\ell + \Delta\ell\rangle$ to $|\ell + 2\Delta\ell\rangle$ transition. These values are labeled in Fig. 8.2.

Let us generalize from an initial rotational eigenstate $|\ell\rangle$ to an arbitrary superposition $\sum_\ell c_\ell |\ell\rangle$. In Chapter 7, we showed that we can resolve individual transitions corresponding to a specific value of $\Delta\ell$ as long as the width of the distribution σ_ℓ was sufficiently narrow. Under this condition, there will be a closed 4-level system for each ℓ. We may therefore consider this an ensemble of 4-level systems, each with the same couplings Ω (Equation 7.31) but different energy splittings and thus different detunings δ_ℓ and δ'_ℓ. The total Hamiltonian of the system is thus just a sum of the Hamiltonian for each ℓ, all of which commute with each other:

$$H = \sum_\ell H_\ell \tag{8.11}$$

For the rotational Ramsey experiment we wish to run, the experimental sequence is thus:

1. $\pi/2$ pulse with phase 0 on $\Delta\ell$ sideband,

2. Wait for time T,

3. $\pi/2$ pulse with phase ϕ on $\Delta\ell$ sideband.

Given the Hamiltonian in equation 8.10, we can explicitly find the time-evolution operator for the rotational Ramsey experiment for each ℓ subsystem and therefore for the whole system altogether. This is made easier if we assume that for the $\pi/2$ pulses, the Rabi frequecy Ω is large enough that $\Omega \gg \delta_\ell$ for all ℓ which have considerable occupation. The time of each $\pi/2$ pulse is defined such that $\Omega t_{\pi/2} = \frac{\pi}{2}$. The time evolution operator for the ℓ subsystem

is then

$$U_\ell(T) = e^{-iH_{\ell,\pi/2,\phi=\phi}t_{\pi/2}} e^{-iH_{\ell,\Omega=0}T} e^{-iH_{\ell,\pi/2,\phi=0}t_{\pi/2}}$$

$$= \exp\left[-i\frac{\pi}{2\Omega}\frac{\Omega}{2}\begin{pmatrix} 0 & (-1)^{\Delta\ell}e^{-i\phi} & e^{-i\phi} & 0 \\ (-1)^{\Delta\ell}e^{i\phi} & 0 & 0 & e^{-i\phi} \\ e^{i\phi} & 0 & 0 & (-1)^{\Delta\ell}e^{-i\phi} \\ 0 & e^{i\phi} & (-1)^{\Delta\ell}e^{i\phi} & 0 \end{pmatrix}\right]$$

$$\times \exp\left[-iT\begin{pmatrix} -\delta'_\ell & 0 & 0 & 0 \\ 0 & 0 & 0 & 0 \\ 0 & 0 & 0 & 0 \\ 0 & 0 & 0 & \delta_\ell \end{pmatrix}\right]$$

$$\times \exp\left[-i\frac{\pi}{2\Omega}\frac{\Omega}{2}\begin{pmatrix} 0 & (-1)^{\Delta\ell} & 1 & 0 \\ (-1)^{\Delta\ell} & 0 & 0 & 1 \\ 1 & 0 & 0 & (-1)^{\Delta\ell} \\ 0 & 1 & (-1)^{\Delta\ell} & 0 \end{pmatrix}\right] \tag{8.12}$$

This matrix evolution can be analyzed with Mathematica. Knowing that we are starting in the initial state $|SS,\ell\rangle = (0,0,0,1)^\top$, we can take matrix elements of this operator to get the probability to end up in any of the 4 states:

$$P_{SS,\ell}(T) = |\langle SS,\ell|U_\ell(T)|SS,\ell\rangle|^2,$$
$$P_{SD,\ell+\Delta\ell}(T) = |\langle SD,\ell+\Delta\ell|U_\ell(T)|SS,\ell\rangle|^2,$$
$$P_{DS,\ell+\Delta\ell}(T) = |\langle DS,\ell+\Delta\ell|U_\ell(T)|SS,\ell\rangle|^2, \tag{8.13}$$
$$P_{DD,\ell+2\Delta\ell}(T) = |\langle DD,\ell+2\Delta\ell|U_\ell(T)|SS,\ell\rangle|^2$$

Finally, from this we can calculate the probabilities for the ions to be in the SS, SD, DS, or DD states given an initial group of ℓ states being populated. Since each 4-level ℓ system is closed within itself, this is just an incoherent sum of each of the individual probabilities, weighted by the initial populations of the ℓ states: $P_{SS} = \sum_\ell |c_\ell|^2 P_{SS,\ell}$, etc. Inserting the matrix elements that we can compute with Mathematica, we get

$$P_{SS}(T,\phi) = \sum_\ell |c_\ell|^2 \left|\tfrac{1}{4}e^{-i\delta_\ell T} + \tfrac{1}{4}e^{i\delta'_\ell T + 2i\phi} - \tfrac{1}{2}e^{i\phi}\right|^2 \tag{8.14a}$$

$$P_{SD}(T,\phi) = P_{DS}(T,\phi) = \sum_\ell |c_\ell|^2 \left|\tfrac{1}{4}e^{-i\delta_\ell T - i\phi} - \tfrac{1}{4}e^{i\delta'_\ell T + i\phi}\right|^2 \tag{8.14b}$$

$$P_{DD}(T,\phi) = \sum_\ell |c_\ell|^2 \left|\tfrac{1}{4}e^{i\delta'_\ell T} + \tfrac{1}{4}e^{-i\delta_\ell T - 2i\phi} + \tfrac{1}{2}e^{-i\phi}\right|^2 \tag{8.14c}$$

From this we can calculate observables like the excitation ($P_{DD} + 0.5P_{SD} + 0.5PDS$) and parity ($P_{DD} + P_{SS} - PDS - PSD$) we give us information about how the superposition has evolved.

Let us look at an example of the interference signal. Choosing $\Delta\ell = 4$, and with a secular radial trap frequency of $\omega_\rho = 2\pi \times 800$ kHz, Equation 8.9 predicts a revival time of $t_{\text{revival}} \approx 21.14$ ms. Fig. 8.3 gives the 4 probabilities as a function of wait time T under the conditions

- $\{c_\ell\}$ is a Gaussian-distributed with a standard deviation (σ_ℓ) of about 5 which is smaller than we are able to prepare in practice. This is chosen so that the width of the interference signal is large enough to see in the figure. The duration of the rephasing window is inversely porportional to σ_ℓ. In reality $\sigma_\ell \approx 40$. Additionally, the particles are distinguishable meaning that c_ℓ is finite for all integers ℓ.

- The phase ϕ of the second pulse is always zero.

- A detuning from the center of the distribution of $\delta_{\ell_0} \approx 2\pi \times 2$ kHz is present in order to introduce Ramsey fringes to allow the full contrast to be visible.

The excitation and parity are also shown, calculated as $P_{DD} + \frac{1}{2}(P_{SD} + P_{DS})$ and $P_{DD} + P_{SS} - P_{SD} - P_{DS}$, respectively. The initial dephasing brings both the excitation and parity quickly down to a flat 0.5. This is the same initial dephasing as measured in Fig. 7.11 in Chapter 7. At the predicted revival time, both the excitation and parity signals revive. Interestingly, if we look at the parity instead of the excitation there is an extra revival at half the time. This can be understood as the interference of just the $|SS, \ell\rangle$ and $|DD, \ell + 2\Delta\ell\rangle$ components. These two branches are separated by twice the number of angular momentum quanta, and therefore twice the energy, as the $|SD\rangle$ and $|DS\rangle$ states and therefore rephrase twice as quickly, though the signal is only observable in the parity.

Now we consider the same system where the particles are indistinguishable, such that half the momentum states are eliminated. Fig. 8.4 shows the new experimental evolution. In the case of fermions, this means that the distribution is the same as in the distinguishable example, except now c_ℓ has been set to zero for all even ℓ and the population distribution renormalized. For bosons the same is true but with odd terms set to zero. Notice the presence of the expected exchange-revival that was not present for the distinguishable case. The phase of the exchange-revival is also opposite between the two type of particles; however, it is probably difficult in practice to distinguish between the case of fermions and bosons as the difference is equivalent to a shift in the atom frequency vs the laser frequency of only 12 Hz $\times \Delta\ell = 48$ Hz.

Equation 8.14 can be simplified with an approximation, and perhaps some insight can be gained from this simplification: If we ignore the difference between δ_ℓ and δ'_ℓ which is only
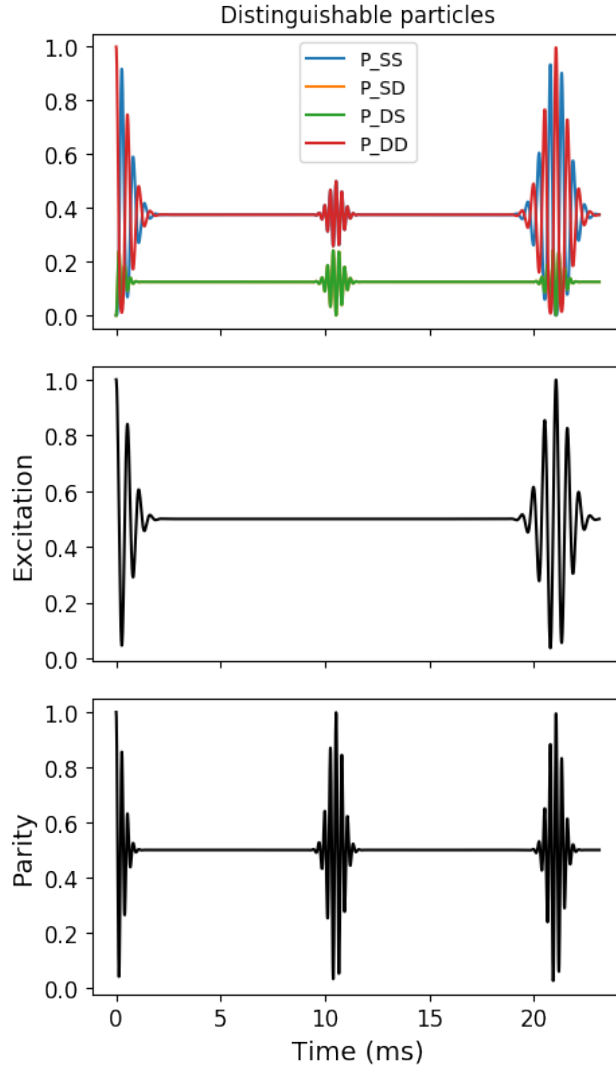
Figure 8.3: Interference signal as a function of Ramsey wait time T calculated from Equation 8.14, for $\Delta\ell = 4$, $\phi = 0$, $\sigma_\ell = 5$, and $\Delta_\ell \approx 2\pi \times 2$ kHz. In this case of distinguishable particles, all ℓ states, even or odd, have population, Gaussian distributed.

$\frac{\hbar}{I}\Delta\ell^2 \approx 12$ Hz $\times \Delta\ell^2$, then we can set $\delta'_\ell = \delta_\ell$ and equations 8.14 simplify to

$$P_{SS}(T, \phi) = \sum_\ell |c_\ell|^2 \sin^4\left(\frac{\delta_\ell T + \phi}{2}\right) \tag{8.15a}$$

$$P_{SD}(T, \phi) = P_{DS}(T, \phi) = \sum_\ell |c_\ell|^2 \frac{1}{4}\sin^2(\delta_\ell T + \phi) \tag{8.15b}$$

$$P_{DD}(T, \phi) = \sum_\ell |c_\ell|^2 \cos^4\left(\frac{\delta_\ell T + \phi}{2}\right) \tag{8.15c}$$
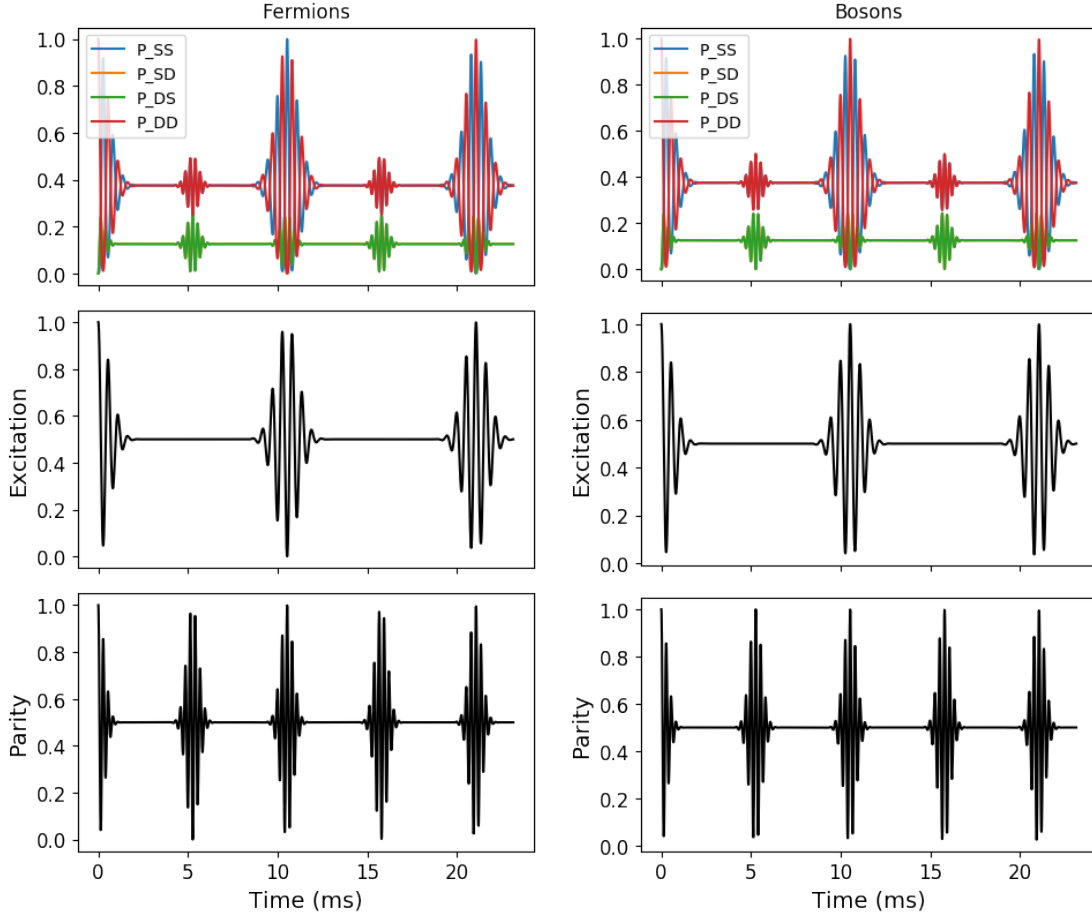
Figure 8.4: Same as Fig. 8.3, except with $c_\ell = 0$ if ℓ is even (fermions, left) or if ℓ is odd (bosons, right).

Furthermore, the excitation and parity simplify to

$$\text{exc}(T, \phi) = \sum_\ell |c_\ell|^2 \cos^2\left(\frac{\delta_\ell T + \phi}{2}\right) \tag{8.16a}$$

$$\text{par}(T, \phi) = \sum_\ell |c_\ell|^2 \cos^2(\delta_\ell T + \phi) \tag{8.16b}$$

In this simplification, the parity signal is manifestly the same as the excitation signal, except at twice the frequency. This also shows explicitly that the signal for each ℓ state is a cosine each with a slightly different frequency (namely, its own detuning from the laser frequency), so the interference comes from the beating of these cosines against one another.

Finally, note that the initial rotation frequency needed to produce the rotational superposition (or equivalently, the value of ℓ_0 around which the distribution $\{c_\ell\}$ is centered) does

not enter into this analysis; only the *difference* between the laser frequency and the rotation frequency matters (that is, only the detuning from the $\Delta\ell$ resonance matters).

8.5 Rotating Interferometer in Position Space

With the experiment laid out now, I would like to introduce a second interpretation. So far, we have discussed this experiment in terms of phase accumulations beating against one another and missing momentum states. However, going back to the idea mentioned in the Section 8.2, a more intuitive picture exists though it is harder frame mathematically.

Consider the first $\pi/2$ pulse we apply to the rotational side band. This creates a superposition of one group of ℓ states and another group of ℓ states whose value has increased slightly by $\Delta\ell$. This second group has a larger angular momentum and is therefore rotating faster than the first by an angular velocity of 12 Hz $\times \Delta\ell$. In fact, we have created a matter wave interferometer with circular boundary conditions. If we were to try to recombine these two arms with a second $\pi/2$ pulse at an arbitrary time we would not observe any interference pattern as we scanned the phase of the final pulse because the two arms would not be overlapped spatially. However, if one were to wait $\frac{1}{12 \text{ Hz}}$, the ions would return to their original locations and we could observe the full contrast of the interference as if we had run a Ramsey experiment on a stationary ion crystal. But what if the ions are indistinguishable? Well, then they should be able to not only interfere with themselves, but each other. That is to say, instead of waiting the full $\frac{1}{12 \text{ Hz}}$ to see a return of contrast, we should also observe interference when the ions have exchanged at half the time as well! If they were not indistinguishable, one should not be able to interfere them with each other. Notice, the revival of interference at the exchange time is the same result we came to when considering the occupied momentum states.

We can interpret other effects in this framework. For instance, thinking in the momentum space picture, we expect the width of the revival to be inversely related to the spread σ_ℓ (larger spread implying narrower revival), because the more states are occupied, the more differing phase contributions there are when the wait time differs slightly from the revival time. A small σ_ℓ corresponds to a large amount of spatial uncertainty as one now has a more precisely known momentum state. Therefore, with a more spread out spatial wave function, the ions' wave functions are overlapping for a longer time; therefore, the interference signal is visible over a longer window.

8.6 Experimental Stability Considerations

For our typical experimental parameters and using 4th order superpositions, t_{revival} is about 20 ms. This is the largest rotational superposition we can create at this time with high contrast ($> 80\%$). So in order to observe the interference signal predicted in Section 8.4,

our rotational superposition must be phase stable and parity stable over the 20 ms of experimental duration.

Parity stability is essential because this experiment is predicated on the idea that the parity of the wave function is enforced on the rotational mode. Therefore, if some of the relative modes are heating (changing motional state), the parity might no longer be solely encoded on the rotational mode. Subsequently the unoccupied half of the angular momentum states might become occupied. This would result in a loss of exchange signal. Since our experiment is expected to take about 20 ms for a full rotation, that means we need less than 1 quanta per 20 ms of heating in our relative modes which can change the parity of the wave function. Currently we meet this criteria for both the stretch and vertical tilt modes. Currently we have a heating rate of 40 quanta/second for the stretch mode at 1.340 MHz and <1 quantum/second for the vertical tilt mode at 1.275 MHz.

It is not clear how finite heating in the stretch mode would influence our signal. By our own arguments, heating of the stretch mode alone by odd integers should be impossible as it would change the parity of the overall wave function. However, if each heating event corresponds to a heating of the rotational state, that could change our calculations significantly. However, if the heating rate is below 1 quanta per 20 ms, we can say confidently there is no issue either way. Though our rate of 40 quanta/second is close to that limit, that number can likely be improved should it eventually limit our experiments.

Additionally, we must have stability in the phase of the superposition. This includes the optical mode and the rotational mode. The primary mechanism for decoherence of the optical mode is magnetic field fluctuations. By implementing a static magnetic field with permanent magnets and doing our operations on the less magnetically sensitive $S_{+1/2} \rightarrow D_{+1/2}$ line, we can achieve optical coherences of about 2.5 ms as shown in the Ramsey experiment on the left in Fig. 8.5, increased from ≈ 1 ms when the magnetic fields were sourced by coils. Here we are limited by the shot to shot change of the magnetic field. However, with a spin echo on the optical mode [74], we can eliminate the low frequency noise and extend the coherence to about 35% contrast at 20ms as shown in red and focused on in the right panel of the same figure. Ideally, this curve would start from zero and move to 0.5 as the system decoheres. However, the magnetic field changes with the phase of the wall voltage (60 Hz) and causes a predicable drift in the phase of the superposition. This is what causes the large fluctuations of the echoed experiment. A phase scan at any of these point reveals the full contrast though the phase from the wall wanders enough that one can get a sense of the coherence from a single time series.

In the final experiment, we will be able to perform spin echoes on the optical mode, despite the fact that the superposition is made with motional sidebands. As long an even number of echoes are performed, the system is closed and the phase of the echo pulses cancels out. If the full interferometer time is T, we apply π pulses applied on the optical carrier, not the rotational sideband, at $T/4$ and $3T/4$, a CPMG timing sequence [75]. This dynamically decouples the superposition from the decoherence of the optical mode while canceling the phase of the laser introduced by the echo pulse and keeping the system closed.

With the optical mode sufficiently coherent to see both an exchange and the distinguish-
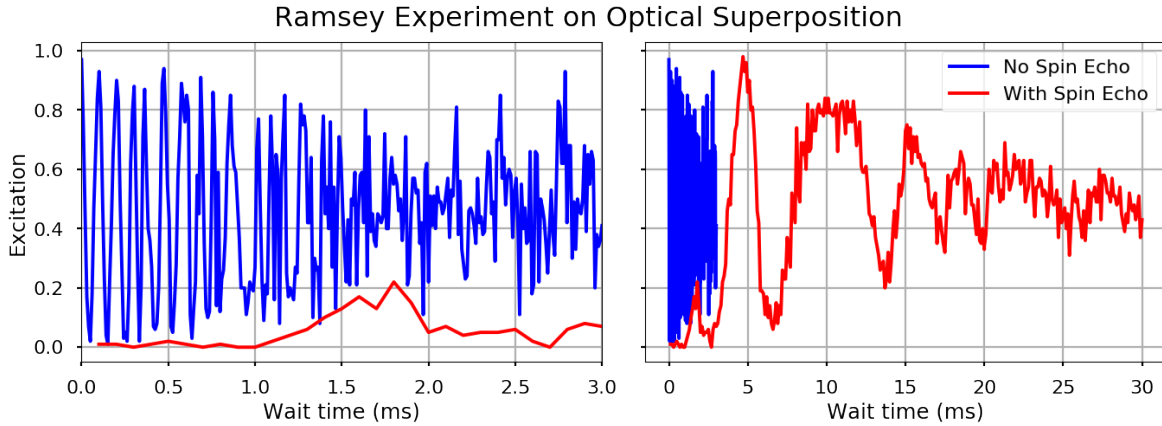
Figure 8.5: Ramsey experiments on our optical mode. Left: Zoomed in on the unechoed Rabi flop. Right: Zoomed out to show the same experiment with a single spin echo on the optical mode included.

able revival time, we must consider the stability of the rotational mode. Unlike the optical mode, we cannot spin perform a spin echo on the rotational mode as that will return the system to its original state and we will never be able to achieve an exchange. The energy difference between the two rotational modes is $\Delta E_\ell = 2\hbar\omega_r\Delta\ell$ as given by Equation 7.28. In this equation, ω_r is the only parameter subject to instability. Because ω_r depends on r^{-2} where r is still the ring radius, any decoherence source influencing r could also decohere our superposition. The most obvious candidate is what we will call 'trap instabilities' which are fast fluctuations in the power delivered to the trap by the RF drive. This causes the trap frequency, and therefore the radius, to fluctuate unpredictably. Setting the force applied to an ion by the confining trap potential with frequency ω_t equal to the Coulomb repulsion of two ions in such a trap, we can solve for r as a function of the trap frequency.

$$m\omega_t^2 r = \frac{e^2}{4\pi\epsilon_0 r^2} \implies r = \sqrt[3]{\frac{e^2}{4\pi\epsilon_0 m\omega_t^2}} \tag{8.17}$$

Therefore,

$$\Delta E_\ell = \frac{\hbar^2\ell\Delta\ell}{2m}\sqrt[\frac{2}{3}]{\frac{4\pi\epsilon_0 m\omega_t^2}{e^2}}. \tag{8.18}$$

Propagating any instability in ω_t to ΔE_ℓ yields

$$\delta\Delta E_\ell/\Delta E_\ell = \frac{4\Delta\ell}{3}\delta\omega_t/\omega_t \tag{8.19}$$

We can measure $\delta\omega_t/\omega_T$ by measuring the energy stability of a single ion in a superposition of harmonic oscillator states. Through the same arguments as above, for a harmonic oscillator superposition:

$$\delta\Delta E_{h.o.}/\Delta E_{h.o.} = \hbar\delta\omega_t/\omega_t \tag{8.20}$$

Therefore,

$$\delta\Delta E_\ell/\Delta E_\ell = \frac{4\Delta\ell}{3}\delta\Delta E_{h.o.}/\Delta E_{h.o.} \tag{8.21}$$

$$\delta\Delta E_\ell = \frac{4\Delta\ell}{3}\delta\Delta E_{h.o.}\Delta E_\ell/\Delta E_{h.o.} = \frac{4\Delta\ell}{3}\frac{\omega_{rot}}{\omega_t}\delta\Delta E_{h.o.} \tag{8.22}$$

We measure the coherence of the harmonic oscillator superposition with trap frequency 780 kHz in the same way that we did for the optical mode in Fig. 8.5 but we now create the superposition $|S, n = 0\rangle + |D, n = 1\rangle$. As stated before, we apply the spin echo only on the optical mode because in the final rotational Ramsey experiment we will not be able to echo the motional mode. Fig. 8.6 shows that we have a contrast of 30% at 15 ms. When convolved with the fact the we know the optical contrast has already been reduced to about 60% at this point, we can say that the motional mode still has about 40% contrast at this time. This is a much larger motional coherence than we have measured in other experimental set-ups in our lab. We largely attribute this high quality motional coherence to the fact that we do not need an RF amplifier to run this trap. Plugging this coherence time into $\delta\Delta E_{h.o.}$, we calculate that the coherence of a rotational superposition at 100 kHz should be about $6/\Delta\ell$ times whatever we measure for the harmonic oscillator. Therefore, a rotational superposition of 4th order should have $\approx$40% coherence at 22 ms, sufficient for us to detect a signal.
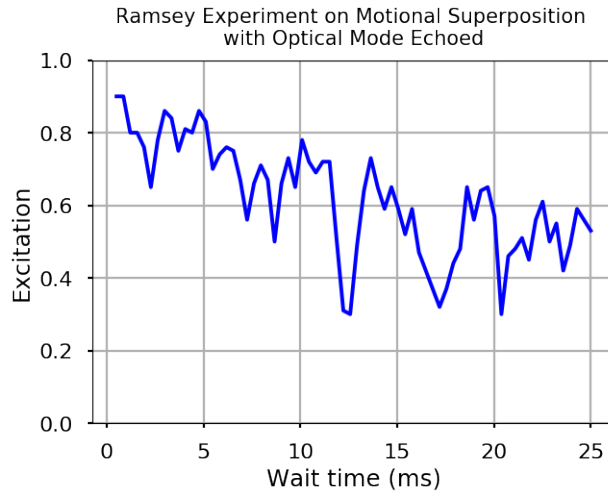
Figure 8.6: Ramsey experiment is done by first applying a $\pi/2$ pulse on the sideband cooled blue common x-radial mode. Then two echos are applied to the optical mode in a CPMG scheme to keep the optical superposition coherent. Finally another $\pi/2$ is applied and the optical state is readout.

8.7 Poor Rotational Coherence

As stated in Section 8.6, our expectations from trap instabilities and heating suggest we should observe coherence in our 4th order rotational sidebands out to 30 ms. However, when the full experiment is run, we find that we have no revival of excitation or parity at any time. This could be due to any number of decoherence effects and it is difficult to say on what time scale they take place because after the initial dephasing in less than 1 ms, we expect no intermediate signal until the revival time.

For this reason, we investigate the coherence by performing a spin echo pulse on the rotational mode. A sketch of the modified experiment is shown in Fig. 8.7. After state initialization (1), a $\pi/2$ pulse on a rotational sideband creates a rotational superposition (2). After the system is allowed to evolve and the wave functions separate for some time $T/2$ (3). Then, a π pulse on the same sideband flips the optical state and rotational state of both ions (4). This makes the two branches begin to move towards each other (5) and after $T/2$ again, the arms are recombined with a second $\pi/2$ pulse. This allows us to read out the coherence of the system as a function of time for any time, T, unlike the unechoed interferometer. It is important to remember that when studying the results of this experiment that the rotational echo could dynamically decouple decoherence effects that will ultimately limit our unechoed experiment; however, it will give us an upper limit on our unechoed coherence.
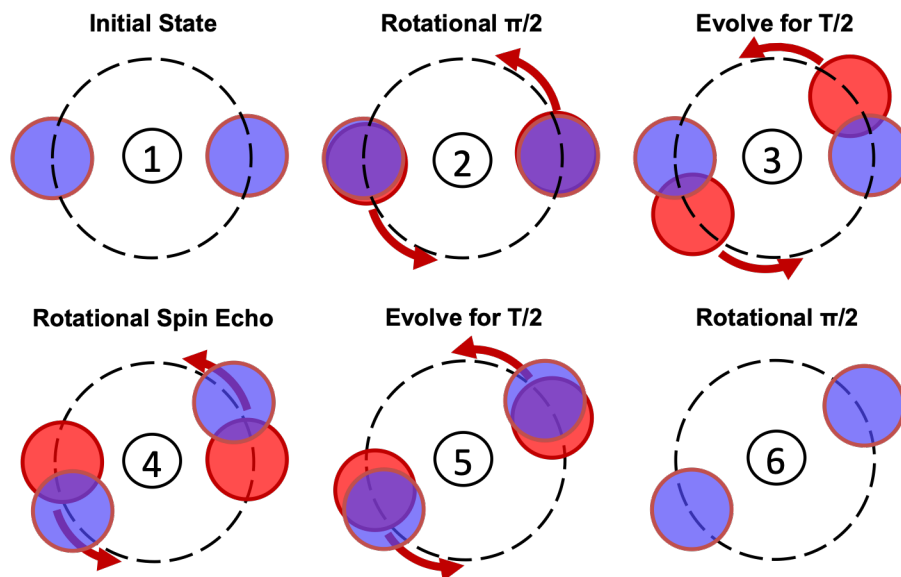
Figure 8.7: Sketch of rotational interferometer with a rotational spin echo included.

The results of this experiment are presented in Fig. 8.8. It plots the contrast of a phase scan as a function of time for the 1st and 4th order interferometers. At each point we run the echoed Ramsey sequence and scan the phase of the final pulse. This traces out a sine curve where we define the contrast as the peak to peak amplitude of that curve. We find the

coherence time is much shorter than the expected. For our fourth order sideband, we have lost all contrast by 2 ms, over an order of magnitude worse than our expectation without a spin echo. In this section I will lay out our effort to understand this phenomena and the trends we have observed, but ultimately we do not have an explanation for this rapid decoherence.
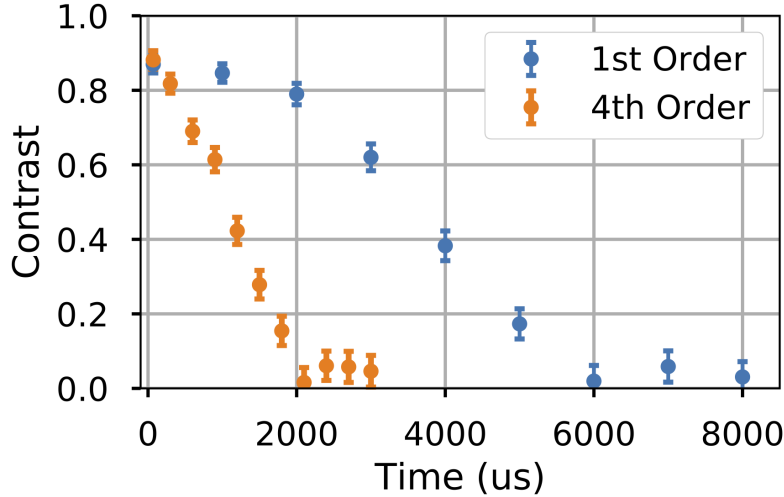
Figure 8.8: Results of rotational Ramsey experiment with a rotational spin echo.

Rotation State Diffusion

Fig. 8.8 shows that the coherence time decreases as the size of the superposition $\Delta\ell$ increases. Similar decoherence trends have been observed in harmonic oscillator Fock state superpositions where the coherence time is proportional to Δn^{-2} when the decoherence is cause by ion interaction with noisy electric fields [76, 77]. However, in order to assess if this is the cause of our decoherence, we must first understand the differences between harmonic oscillator modes and rotational modes in the context of how they interact with noisy electric fields.

For harmonic oscillators, typically we characterize an ion's interaction a with noisy electric field through what is known as a 'heating rate'. In a heating rate measurement, one prepares the ion at a certain temperature and measures the thermal occupation of a motional mode in an ion crystal as a function. Then, the measurement is repeated but after state preparation, we wait for a certain amount of time, t, before measuring the occupation of the motional mode. If the ion is interacting with a noisy field that oscillates at the same frequency as the ion's secular motion, that mode will increase linearly in temperature as a function of wait time t. This linear increase, characterized by $\dot{\bar{n}}$, is due to the fact that the coupling between Fock states of a motional mode in harmonic oscillator through electric fields is

$\langle n + \Delta n| \, e^{ikx} \, |n\rangle \approx \langle n + \Delta n| \, a^\dagger + a \, |n\rangle \propto \sqrt{(n)}$. Therefore, if we subtract the difference in coupling rates between $|n\rangle \to |n+1\rangle$ and $|n\rangle \to |n-1\rangle$, we find that

$$\dot{n} \propto \sqrt{n}^2 - \sqrt{n-1}^2 = \text{constant.} \tag{8.23}$$

Now consider the same analysis for a rigid rotor. We know from Equation 7.31 that $\langle \ell + \Delta\ell| \, e^{ikx} \, |\ell\rangle$ is independent of $|\ell\rangle$. Therefore $\dot{\ell}_0 = 0$. However, there is still a coupling between levels such that a state $|\ell\rangle$ has an equal chance of moving to either $|\ell+1\rangle$ or $|\ell-1\rangle$ at some frequency, D. This sort of system defines a random walk in angular momentum space. Therefore, if the angular momentum distribution starts off with some center ℓ_0 and spread σ_ℓ, we do not expect ℓ_0 to change; however, σ_ℓ will increase according to the evolution of a random walk:

$$\sigma_\ell(t) = \sqrt{2D(t + \sigma_{\ell 0}^2/2D)} \tag{8.24}$$

where $\sigma_\ell(t)$ is the final distribution after time t, D is the diffusion constant (rate of hopping between $|\ell\rangle$ and $|\ell \pm 1\rangle$), and $\sigma_{\ell 0}$ is the initial angular momentum spread.

With this in mind, we can characterize how the rotor states are interacting with the noise in the system by measuring the diffusion rate of angular momentum distribution of the rotating crystal. We find that the most reliable method of measuring σ_ℓ is by fitting the first order Ramsey dephasing curve for a significant detuning as shown in the top plot of Fig. 7.11. Fitting this curve is advantageous for several reasons. Firstly, the dephasing rate is sensitive to σ_ℓ and if the detuning is large, the fit has only a small covariance between the detuning and σ_ℓ. Secondly, the decay of the curve is not sensitive to the occupation of any harmonic oscillator modes (like Rabi flops would be). And finally, the contrast of the operation is relatively high since the width of the transition in frequency space is smallest for $\Delta\ell = 1$. Fitting Ramsey scans as a function of wait time we get the curve shown in orange in Fig. 8.9 which yields a diffusion rate of 15 ± 3 ms^{-1}.

Unlike for harmonic oscillator states, dipole fields do not couple to rotor states because their spatial profile does not match the motion of the ions. However, in-plane quadrupole fields can effect rotational states. Therefore, in order to experimentally investigate whether this diffusion rate is responsible for the decoherence of our rotational states, we can inject white noise onto one of our rotation circuit AWG channels which will produce a noisy quadrupole at the ion trapping site. As we increase the amount of noise injected, the diffusion rate should increase and we look for a corresponding increase in rotational decoherence rate. Fig. 8.9 shows that we do indeed manage to increase the diffusion rate over an order of magnitude through quadrupole noise injection. Furthermore, we can be sure that this is indeed quadrupole noise as the heating rate of the common harmonic oscillator modes are unaffected by this noise inject.

Fig. 8.10 shows that we do see an increase in the decoherence rate of both the first and fourth order rotational superpositions as we increase the diffusion rate of the rotational mode. However, the dependance is very weak. For a 30 fold increase in the diffusion rate, we only observe at most a 3 fold increase in the decoherence rate.
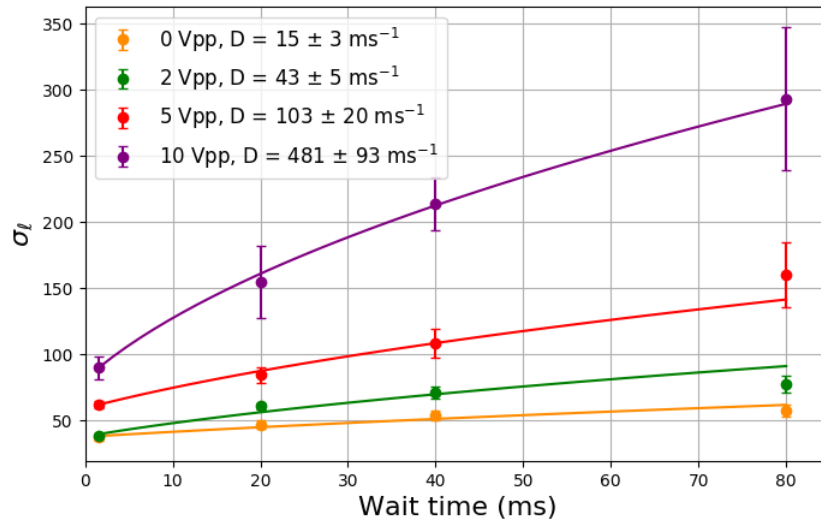
Figure 8.9: Diffusion rate measurement for various levels of quadrupole noise injection. The
level of injected noise and fit diffusion rate are given in the legend. The noise injection level is
given in volts peak-to-peak as displayed on the AWG but the majority of that is filtered out
before reaching the ion, therefore it is only useful as a relative voltage scale. Additionally,
the noise at the ion goes as the voltage squared.
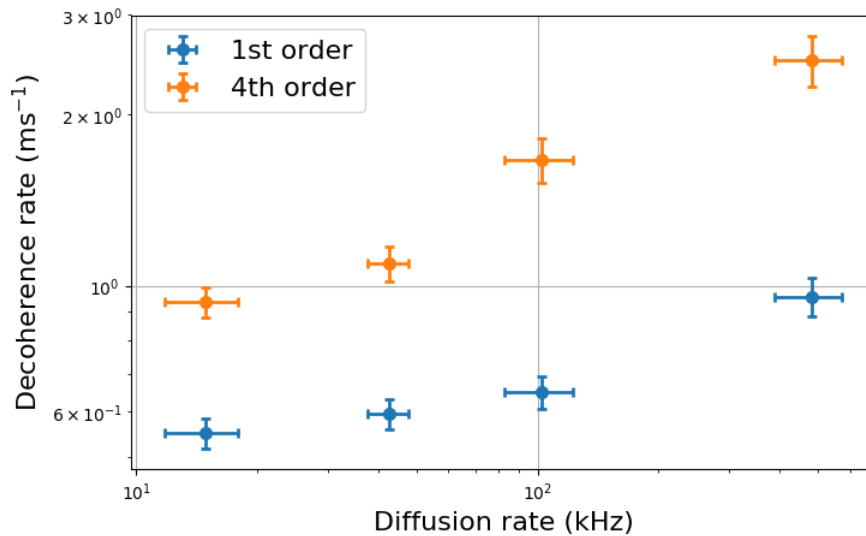
Figure 8.10: Rotational coherence versus diffusion rate caused by quadrupole noise injection
for first and fourth order rotational superpositions.

This does not prove that quadrupole noise such as we are injecting is the cause of our
decoherence. It could that the noise injection is a secondary effect that has been increased
to the point that it begins to impact the coherence when it was not before or that by

injecting the noise we are influencing some other property of the system that is causing our superposition to decohere. Either way, it would be useful to theoretically understand the mechanism through which quadrupole noise can cause rotational decoherence.

For harmonic oscillators, Turchette et al. [76] uses a master equation treatment to calculate how noisy dipole fields decohere harmonic oscillator Fock state superpositions. In doing a naive translation of this method to rotational states, we replace the harmonic oscillator raising and lowering operators (a and $a^\dagger$) with the angular momentum raising and lowering operators defined as $L^\pm |\ell\rangle = |\ell \pm 1\rangle$. With this analysis, we are able to reproduce the decoherence observed in harmonic oscillator superposition but we find no decoherence in our rotational superposition.

These two results are not necessarily contradictory. Most likely, quadrupole noise is not directly causing our decoherence as our simulations suggests, but perhaps injecting noise is increasing diffusion (as expected) but also affecting some secondary system property that directly influences rotational coherence. For example, one could imagine noise injection decreasing the stability of our trap frequency which can effect our coherence. We have already checked that this is not the case, but it serves a point that there are indirect means through which noise injection can affect our coherence.

Coherence vs. Rotation Frequency

Interestingly, we find that the rotational coherence has a slight dependence on the speed at which the crystal is rotating, f_{rot}. One might imagine this would be the case if pure dephasing due to instabilities in r were to blame because now the energy between rotational states is larger so the energy instability would be amplified. However, we find that we have a negative relationship between decoherence rate, γ, and rotation speed which is the opposite of what we would expect from pure dephasing. Fig. 8.11 shows this dependance. Empirically, we find the decoherence rate goes as $f_{\text{rot}}^{-1/3}$ for both the 1st and 4th order superpositions. There are a few reasons why increasing the rotation speed could help our coherence. Firstly, increasing the rotation speed increases the energy of the crystal and therefore decreases the relative size of residual fields that affect our symmetry. Secondly, rotating faster increases the frequency separation of each $\Delta \ell$ transition so if off-resonant excitation is to blame, that also could be improved. We intentionally increase the size of the in-plane symmetry breaking quadrupole and do not see a reduction of coherence time eliminating the first mechanism as the cause of decoherence. Additionally, we find that the coherence is independent of the Rabi frequency of the Ramsey pulses. If off-resonant coupling were to blame, one would expect the coherence to improve as the Rabi frequency is decreased therefore we can eliminate the second mechanism as well. Although both of these mechanisms have been ruled out, there could be others which we have not yet considered.
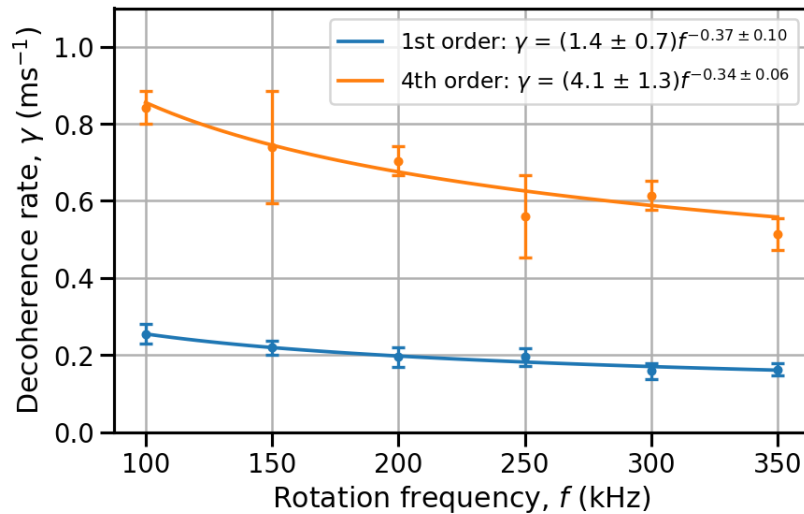
Figure 8.11: Decoherence rate versus rotation speed of the ion crystal. The data for each order respectively is fit to a power law.

Potential Mechanisms for Decoherence

Through our investigations we have considered and ruled out many potential mechanisms that would explain our smaller than expected rotational superposition coherence time. A list of theories and mechanisms for decoherence that we have explored and ruled out are given here.

- *The occupation of many angular momentum states*: The number of angular momentum states populated, σ_ℓ, could potentially affect our coherence for a number of reasons. Though we perform a spin-echo on the motional mode which should rephase each superposition independent of its detuning from the laser frequency, perhaps the loss of contrast in our Ramsey experiment is a product of the exact state we are preparing. However, we find that the coherence time of a first order superposition is independent of σ_ℓ between $\sigma_\ell = 40$ and $\sigma_\ell = 400$. This suggests that our decoherence mechanism should persist for even a single state $|\ell\rangle$ and is not a function of state preparation or effects emerging from mixtures or ensembles of many angular momentum eigenstates.

- *Coupling between finite temperature relative modes*: For harmonic oscillators, it is a known effect that superpositions of relative mode Fock states decohere faster than common modes if all other relative modes are not in the ground state [78]. This is due to the fact that if the two ions are moving relative to each other, their separation is modulated which in turn modulates the frequency of the other relative harmonic modes of motion. By cooling all relative modes to the ground state, the modulation is removed and the coherence of the relative mode superpositions are restore to levels consistent with the common modes. Because the rotational mode is a relative mode,

we could expect a similar mechanism to be the source of our decoherence. However, we find that sideband cooling both the in-plane stretch mode as well as the vertical tilt mode to the ground state before spin-up does not affect the rotational coherence in any way. Therefore we can conclude that although the finite temperature of differential modes might limit our coherence eventually, it is not the current limiting mechanism.

- *Parametric coupling of motional modes*: If the frequency of two modes of motion within an ion crystal are close to one another, electric fields with the correct spatial profile oscillating at the difference frequency can be used to parametrically couple energy between the two modes [79]. It is possible that an integer multiple of the rotation frequency is close to another mode of motion within the crystal and being coupled to it through some noisy field in the system. If this were the case, changing the frequency of the motional modes of the system by changing the trap frequency should affect the rotational coherence. We find this is not the case. Additionally, one would not expect a smooth, monotonic coherence time as a function of rotation frequency such as we observed in Fig 8.11. Rather one would expect several peaked resonances as the difference in trap frequencies aligned with the noise source.

- *Motional coupling through micromotion lines*: If trapped ions are held away from the RF null, they experience a driving force at the frequency of the trapping RF voltage in addition to the pseudopotential (Sec. 2.1). In these experiments, the ion rotor is formed by two ions pushing each other out of a single RF null (Sec. 7.2). Therefore, in this experiment, the ions will always experience micromotion. This creates another set of frequencies present in the system which might cause coupling between motional modes as described in the previous bullet point. Therefore, we attempted this experiment with an RF drive increased by 2 MHz and decreased by 2 MHz to try to avoid any potentially unlucky selections of drive frequency. We found this had no effect on the coherence time of the rotational mode.

- *Ions not centered at RF null*: If the center of the ions is not aligned with the RF null, one side of the ring will experience more micromotion than the other. This asymmetry in the field of fields could apply a modulation to the rotational state energies and induce decoherence. However, we change the in-plane dipole fields by ± 3 V/m, much more than our uncertainty in micromotion compensation fields (± 0.2 V/m), and don't observe any change in coherence. Similarly, changing the vertical field (which does not impact the dynamics of the in plane motion but we check for completeness anyway) by ± 10 V/m does not affect the coherence of the rotational mode either.

- *Residual quadrupole fields*: Similarly, when we compensate the static quadrupole to create our symmetric rotor potential, it is possible we have a residual field that modulates the motion of the rotor. However, we find that we can change the size of our in-plane quadrupole fields ± 500 V/m^2 (larger than our compensation uncertainty ± 100 V/m^2) without changing our rotational coherence.

- *Initial state dispersion*: A quantum rotor that begins in a spatially localized state, as our state certainly is at some point during the release process, disperses on the timescale of $1/4\sigma_\ell\omega_r$ which is inversely proportional to the initial angular uncertainty of the wavefunction [80]. Therefore for our parameters, the wavefunction has dispersed around the circumference of the ring in about 1 ms. However, we find our coherence time is independent of how long we let the state disperse after state preparation but before running the Ramsey experiment.

- *Large spatial extent of the rotor wavefunction*: The physical size of the rotor eigenstates is determined by the diameter of the crystal ($\sim$6 µm). Compared to harmonic oscillator eigenstates which are only a few 10s of nanometers for trap frequencies around 1 MHz, this is very large and also on the same order as the projection of the wavevector of the 729 nm spectroscopy laser on the rotational mode (729 nm/$\sin 7° = 6.0$ µm) which is a characteristic length scale of the atom/laser coupling. However, we find that the coherence of the optical mode observed in Fig. 8.5 is maintained when the experiment is performed on a freely rotating crystal suggesting the size of the wavefunction relative the wavelength of the light does not impact our coherence.

- *Misaligned spectroscopy laser*: The 729 nm spectroscopy laser address our rotor globally and is centered on the rotor from a near-vertical angle ($\sim 7°$). However, if it is not perfectly centered, this could introduce a positional asymmetry into our system which could break our symmetry. Typically, we can align the beam such that the coupling between the laser and the ion is within 10% on either size of the ring by performing optical Rabi oscillations on a pinned crystal and measuring the Rabi frequency of the individual ions. We find that we can translate the laser such that the coupling to the ions on one side of the ring is twice that on the other but this does not affect our rotational coherence.

- *Background gas collisions*: Background gas collisions have been proposed as a decoherence mechanism in molecular rotors [81]. Because ions can be trapped without the presence of a background gas, it is unlikely that this is our source of decoherence. However, we can confirm this by turning off our active vacuum pumps for tens of minutes, letting the vacuum degrade, then attempting our rotational coherence measurement. We observe a reduction in the time we can hold a single ion in the trap from many hours to a few minutes suggesting at least an order of magnitude increase in the background pressure. However, we find that the rotational coherence in unaffected under these conditions.

- *Experimental miscalibrations*: Perhaps we have an experimental issue where either the duration or placement in time of one of our pulses is miscalibrated. We vary the time and power of both the spin-echo pulse and the final Ramsey pulse but find that our current setting produce the largest contrast at all times suggesting a properly calibrated system.

Conclusions

The observed decrease in rotational coherence time with injected quadrupole noise and the dependence of the coherence time on rotation frequency suggest a mechanism that does indeed depend on a noisy field that interacts with our system in a way that is dependent on the rotation speed. However, our basic attempt to translate the treatment of harmonic oscillator states in noisy field suggested that no decoherence should be observed. An empirical investigation of other system parameters did not reveal a promising mechanism for rotational decoherence either.

It seems that the most likely cause of the rotational decoherence in this system is a physical mechanism that arises from how rotational states interact with external fields that is not captured by our basic model. The next step in addressing this issue would be to develop a more complete underlying theory of how rotational modes might decohere in the presence of noise sources. Some work has been done in this area of study for other systems such as molecules [82, 83] though most are focused on background gas scattering which we have already eliminated as a mechanism in our experiment.

Chapter 9

Summary and Outlook

In this thesis, I discussed a new type of ion ring trap. I began by describing the interesting properties and applications of symmetric ring traps as well as assessing the success of past designs. I presented our new design which uses vias to apply electric potentials to our electrodes keeping the trap symmetric. Additionally, our compact design allowed us to create a small ring very high above the trap surface which is a means of overcoming the primary issue affecting past ring traps.

In this trap we demonstrated our ability to compensate all stray fields at the trapping location and restore the symmetry of the ring. We trapped over 15 ions in the trap and observed delocalization of the ion crystal. This delocalization is an expected effect in a rotationally symmetric system and shows that any imperfection in our potential landscape is less than the thermal energy of the ion crystal. This was a previously unrealized benchmark and indicates the success of our design.

Next, I moved on to lay out our achieved capabilities with this ring system. I discussed spectroscopy of the ring, sub-Doppler cooling methods, and rotational control prospects. The success of these controls dictates which experiments might be accessible to this system in the future.

Continuing, I discussed in detail a protocol for both classical and quantum control of the rotational motion of a small ion ring. By creating a high angular momentum rotational state using a smoothly released rotating asymmetry, I demonstrated how we can spectrally resolve rotational transitions in an ion crystal and coherently drive population between rotational states. We performed Rabi oscillations changing the rotational state by up to four quanta and demonstrated the expected behavior in Ramsey dephasing.

Finally, I concluded this thesis with a discussion of a new experiment that could be run in this symmetric ring system using our new rotational control. I described a rotational interferometer that should allow us to probe the indistinguishable nature of two well-separated calcium ions. I laid out the expected theoretical signatures, the experimental stability requirements, and our efforts towards achieving them. Finally, I reflected on possible causes of our surprisingly low coherence times and mechanisms we have considered and ruled out.

Identifying the source of this unknown decoherence mechanism is the next big step for this

project. If the decoherence mechanism is either an interesting physics effect or a technical limitation, the answer is important for further rotational studies. Additionally, decoherence is a very general phenomena is quantum physics and if rotational states decohere through an unintuitive mechanism, it could be very interesting to learn how that might affect other similar systems such as molecules and other rotors. Furthermore, studying the scalability of the rotation protocol to more ions in both the ring trap and the point trap would be interesting. If the rotational coherence question is solved and indistinguishability observed, it would be very interesting to study under what conditions indistinguishability is maintained. The well-separated system affords many opportunities to apply different measurements to the classical 'particles' and observe how they affect the signature of the ions' quantum indistinguishability.

Bibliography

[1] Tongcang Li et al. "Space-Time Crystals of Trapped Ions". In: *Physical Review Letters* 109.16 (2012), p. 163001. ISSN: 0031-9007. DOI: 10.1103/PhysRevLett.109.163001. arXiv: arXiv:1206.4772v1.

[2] Wolfgang Paul. "Electromagnetic traps for charged and neutral particles". In: *Reviews of Modern Physics* 62.3 (1990), pp. 531–540. ISSN: 0034-6861. DOI: 10.1103/RevModPhys.62.531.

[3] D. Leibfried et al. "Quantum dynamics of single trapped ions". In: *Reviews of Modern Physics* 75.1 (2003), pp. 281–324. ISSN: 0034-6861. DOI: 10.1103/RevModPhys.75.281.

[4] J. Chiaverini et al. "Surface-electrode architecture for ion-trap quantum information processing". In: *Quantum Information and Computation* 5 (2005), pp. 419–439.

[5] Peter Lukas Wilhelm Maunz and Peter Lukas Wilhelm. *High Optical Access Trap 2.0*. Tech. rep. Albuquerque, NM, and Livermore, CA (United States): Sandia National Laboratories, 2016, pp. 796–2016. DOI: 10.2172/1237003.

[6] Da An et al. *Surface trap with dc-tunable ion-electrode distance*. 2018. DOI: 10.1063/1.5046527. arXiv: 1807.06043.

[7] M. Kumph et al. "Operation of a planar-electrode ion-trap array with adjustable RF electrodes". In: *New Journal of Physics* 18.2 (2016). ISSN: 13672630. DOI: 10.1088/1367-2630/18/2/023047. arXiv: 1402.0791.

[8] R Maiwald et al. "Stylus ion trap for enhanced access and sensing". In: *Nature Physics* 5.8 (2009), pp. 551–554. ISSN: 1745-2473. DOI: 10.1038/nphys1311.

[9] K. Mølhave and M. Drewsen. "Formation of translationally cold [Formula Presented] and [Formula Presented] molecules in an ion trap". In: *Physical Review A - Atomic, Molecular, and Optical Physics* 62.1 (2000), p. 4. ISSN: 10941622. DOI: 10.1103/PhysRevA.62.011401.

[10] L. Schmöger et al. "Coulomb crystallization of highly charged ions". In: *Science* 347.6227 (2015), pp. 1233–1236. ISSN: 10959203. DOI: 10.1126/science.aaa2960.

[11] R N Gosselin, E H Pinnington, and W Ansbacher. "Measurement of the lifetimes of the 4p levels in Ca II using laser excitation of a fast beam". In: *Physical Review A* 38.9 (1988), pp. 4887–4890.

[12] Michael Ramm et al. "Precision Measurement Method for Branching Fractions of Excited P$_{1/2}$ States Applied to ^{40}Ca^{+}". In: *Physical Review Letters* 111.2 (2013), p. 023004. ISSN: 0031-9007. DOI: 10.1103/PhysRevLett.111.023004.

[13] P A Barton et al. "Measurement of the lifetime of the 3d ^2D_5/2 state in ^40Ca^+". In: *Phys.˜Rev.˜A* 62 (2000), p. 32503.

[14] D. Budker, D. Kimball, and D. DeMille. *Atomic physics: An exploration through problems and solutions.* 2nd. Oxford Univ. Press, 2008.

[15] C. F. Roos et al. "Experimental demonstration of ground state laser cooling with electromagnetically induced transparency." In: *Physical Review Letters* 85 (2000), p. 5547. DOI: 10.1103/PhysRevLett.85.5547.

[16] G. Morigi, J. Eschner, and C. Keitel. "Ground state laser cooling using electromagnetically induced transparency". In: *Physical Review Letters* 85 (2000), pp. 4458–4461. DOI: 10.1103/PhysRevLett.85.4458.

[17] B. Lounis and C. Cohen-Tannoudji. "Coherent population trapping and Fano profiles". In: *J Phys II France* 2.4 (1992), pp. 579–592. ISSN: 1155-4312. DOI: 10.1051/jp2:1992153.

[18] Regina Lechner et al. "Electromagnetically-induced-transparency ground-state cooling of long ion strings". In: *Physical Review A* 93.5 (2016), p. 053401. ISSN: 2469-9926. DOI: 10.1103/PhysRevA.93.053401.

[19] Andre Van Rynbach, Peter Maunz, and Jungsang Kim. "An integrated mirror and surface ion trap with a tunable trap location". In: *Applied Physics Letters* 109.22 (2016), p. 221108. ISSN: 00036951. DOI: 10.1063/1.4970542. arXiv: 1608.06923.

[20] Lei-Lei Yan, Shi-Lei Su, and Mang Feng. "Determining temperature and Rabi frequency regarding trapped ions in Doppler cooling: An analytic investigation". In: (2019). arXiv: 1902.00302.

[21] J.R. R R R R Johansson, P.D. D D D D Nation, and Franco Nori. "QuTiP: An open-source Python framework for the dynamics of open quantum systems". In: *Computer Physics Communications* 183.4 (2013), pp. 1760–1772. ISSN: 00104655. DOI: 10.1016/j.cpc.2012.02.021. arXiv: arXiv:1110.0573v2.

[22] Hilmar Oberst. "Resonance fluorescence of single Barium ions". PhD thesis. Universit\"{a}t Innsbruck, 1999.

[23] Michael A Nielsen and Isaac L Chuang. *Quantum Computation and Quantum Information: 10th Anniversary Edition.* 2010, p. 702. ISBN: 1107002176. DOI: 10.1017/CBO9780511976667. arXiv: arXiv:1011.1669v3.

[24] Hao-Kun Kun Li et al. "Realization of Translational Symmetry in Trapped Cold Ion Rings". In: *Physical Review Letters* 118.5 (2017), p. 053001. ISSN: 10797114. DOI: 10.1103/PhysRevLett.118.053001. arXiv: 1605.02143 [arXiv:quant-ph].

[25] S. Debnath et al. "Demonstration of a small programmable quantum computer with atomic qubits". In: *Nature* 536.7614 (2016), pp. 63–66. ISSN: 0028-0836. DOI: 10.1038/nature18648.

[26] G.-D. Lin et al. "Large-scale quantum computation in an anharmonic linear ion trap". In: *Preprint* 86.6 (2009), p. 60004. ISSN: 0295-5075. DOI: 10.1209/0295-5075/86/60004.

[27] T W B Kibble. "Topology of cosmic strings and domains". In: *J. Phys.* A9.8 (1976), p. 1387.

[28] S Ulm et al. "Observation of the Kibble-Zurek scaling law for defect formation in ion crystals". en. In: *Nature Communications* 4 (2013), p. 2290. ISSN: 20411723. DOI: 10.1038/ncomms3290. arXiv: arXiv:1302.5343v1.

[29] K Pyka et al. "Topological defect formation and spontaneous symmetry breaking in ion Coulomb crystals." en. In: *Nature Communications* 4 (2013), p. 2291. ISSN: 2041-1723. DOI: 10.1038/ncomms3291. arXiv: 1211.7005.

[30] J P Home et al. "Normal modes of trapped ions in the presence of anharmonic trap potentials". In: *New Journal of Physics* 13.7 (2011), p. 73026. ISSN: 13672630. DOI: 10.1088/1367-2630/13/7/073026. arXiv: 1105.4752.

[31] H. Landa et al. "Structure, dynamics and bifurcations of discrete solitons in trapped ion crystals". In: *New Journal of Physics* 15 (2013). ISSN: 13672630. DOI: 10.1088/1367-2630/15/9/093003. arXiv: arXiv:1305.6754v1.

[32] H. Kaufmann et al. "Fast ion swapping for quantum-information processing". In: *Physical Review A* 95.5 (2017), p. 052319. ISSN: 24699934. DOI: 10.1103/PhysRevA.95.052319. arXiv: 1607.03734.

[33] C. L. Pekeris. "The rotation-vibration coupling in diatomic molecules". In: *Physical Review* 45.2 (1934), pp. 98–103. ISSN: 0031899X. DOI: 10.1103/PhysRev.45.98.

[34] B. Horstmann et al. "Hawking radiation from an acoustic black hole on an ion ring". In: *Physical Review Letters* 104.25 (2010), p. 250403. ISSN: 00319007. DOI: 10.1103/PhysRevLett.104.250403. arXiv: 0904.4801.

[35] Tommaso Calarco et al. "Quantum gates with neutral atoms: Controlling collisional interactions in time-dependent traps". In: *Physical Review A* 61.2 (2000), p. 022304. ISSN: 10941622. DOI: 10.1103/PhysRevA.61.022304. arXiv: 9905013 [quant-ph].

[36] Marek Sasura and Andrew M Steane. "Realistic fast quantum gates with hot trapped ions". In: *Quantum* iv (2002), p. 24. DOI: 10.1103/PhysRevA.67.062318. arXiv: 0212005 [quant-ph].

[37] U. Schramm, T. Schätz, and D. Habs. "Bunched crystalline ion beams". In: *Physical Review Letters* 87.18 (2001), pp. 184801–1–184801–4. ISSN: 10797114. DOI: 10.1103/PhysRevLett.87.184801.

[38]   Boyan Tabakov et al. "Assembling a Ring-Shaped Crystal in a Microfabricated Surface Ion Trap". In: *Physical Review Applied* 4.3 (2015), p. 31001. ISSN: 23317019. DOI: `10.1103/PhysRevApplied.4.031001`. arXiv: `1501.06554`.

[39]   Robert J. RJ J Robert J Robert J Robert J Clark. "Ideal multipole ion traps from planar ring electrodes". In: *Applied Physics B* 113.2 (2013), pp. 171–178. ISSN: 0946-2171. DOI: `10.1007/s00340-013-5451-0`. arXiv: `arXiv:1207.6101v2`.

[40]   Po-Jen Wang et al. "Surface traps for freely rotating ion ring crystals". en. In: *Journal of Physics B: Atomic, Molecular and Optical Physics* 48.20 (2015), p. 205002. ISSN: 0953-4075. DOI: `10.1088/0953-4075/48/20/205002`.

[41]   Gary S. May and Costas J. Spanos. *Fundamentals of Semiconductor Manufacturing and Process Control*. IEEE, 2006, pp. 1–463. ISBN: 0471784060. DOI: `10.1002/0471790281`. arXiv: `arXiv:1011.1669v3`.

[42]   W. R. Thurber. "Resistivity-Dopant Density Relationship for Boron-Doped Silicon". In: *Journal of The Electrochemical Society* 127.10 (1980), p. 2291. ISSN: 00134651. DOI: `10.1149/1.2129394`.

[43]   R C Sterling et al. "Increased surface flashover voltage in microfabricated devices". In: *Applied Physics Letters* 103.14 (2013), p. 143504. ISSN: 00036951. DOI: `10.1063/1.4824012`. arXiv: `1208.5672`.

[44]   Guy F Steib and Eberhard Moll. "High-voltage conditioning at large gaps in industrial vacuum". In: *Journal of Physics D: Applied Physics* 6.2 (1973), pp. 243–255. ISSN: 00223727. DOI: `10.1088/0022-3727/6/2/311`.

[45]   Francis E.H. Tay et al. "Defect-free wet etching through pyrex glass using Cr/Au mask". In: *Microsystem Technologies*. Vol. 12. 10-11. Springer-Verlag, 2006, pp. 935–939. ISBN: 0054200601. DOI: `10.1007/s00542-006-0116-0`.

[46]   L M Bennie et al. "A versatile high resolution objective for imaging quantum gases." EN. In: *Optics express* 21.7 (2013), pp. 9011–6. ISSN: 1094-4087. DOI: `10.1364/OE.21.009011`.

[47]   Bruce W. Shore and Donald Howard Menzel. *Principles of Atomic Spectra*. Wiley, 1968, p. 554. ISBN: 047178835X.

[48]   Grigorios A. Pavliotis. *Stochastic Processes and Applications (Diffusion Processes, the Fokker-Planck and Langevin Equations)*. 2014, pp. 1–345. ISBN: 9789812704139. DOI: `10.1007/978-1-4939-1323-7`.

[49]   F. Diedrich et al. "Laser Cooling to the Zero-Point Energy of Motion". In: *Physical Review Letters* 62.4 (1989), pp. 403–406. ISSN: 0031-9007. DOI: `10.1103/PhysRevLett.62.403`.

[50]   C Monroe et al. "Resolved-sideband Raman cooling of a bound atom to the 3D zero-point energy." In: *Physical Review Letters* 75 (1995), pp. 4011–4014. DOI: `10.1103/PhysRevLett.75.4011`.

[51] Klaus Mølmer and Anders S Sørensen. "Multiparticle entanglement of hot trapped ions." In: *Phys. Rev. Lett.* 82 (1999), p. 1835. DOI: `https://doi.org/10.1103/PhysRevLett.82.1971`.

[52] J Benhelm et al. "Towards fault-tolerant quantum computing with trapped ions". In: *Nature Physics* 4 (2008), p. 463.

[53] Stefan Weigert. "Quantum Particle on a Rotating Loop: Topological Quenching due to a Coriolis-Aharonov-Bohm Effect". In: *Physical Review Letters* 75.8 (1995), pp. 1435–1438. ISSN: 0031-9007. DOI: `10.1103/PhysRevLett.75.1435`.

[54] Atsushi Noguchi et al. "Aharonov–Bohm effect in the tunnelling of a quantum rotor in a linear Paul trap". en. In: *Nature Communications* 5.1 (2014), p. 3868. ISSN: 2041-1723. DOI: `10.1038/ncomms4868`.

[55] C. F. Roos et al. "Revealing Quantum Statistics with a Pair of Distant Atoms". In: *Physical Review Letters* 119.16 (2017), p. 160401. ISSN: 0031-9007. DOI: `10.1103/PhysRevLett.119.160401`.

[56] W C Campbell and P Hamilton. "Rotation sensing with trapped ions". In: *Journal of Physics B: Atomic, Molecular and Optical Physics* 50.6 (2017), p. 064002. ISSN: 0953-4075. DOI: `10.1088/1361-6455/aa5a8f`.

[57] Brynle Barrett et al. "The Sagnac effect: 20 years of development in matter-wave interferometry". In: *Comptes Rendus Physique* 15.10 (2014), pp. 875–883. ISSN: 1631-0705. DOI: `10.1016/J.CRHY.2014.10.009`.

[58] Birger Horstmann et al. "Hawking radiation on an ion ring in the quantum regime". en. In: *New Journal of Physics* 13.4 (2011), p. 45008. ISSN: 1367-2630. DOI: `10.1088/1367-2630/13/4/045008`.

[59] Carlos A. Arango, William W. Kennerly, and Gregory S. Ezra. "Classical and quantum mechanics of diatomic molecules in tilted fields". In: *The Journal of Chemical Physics* 122.18 (2005), p. 184303. ISSN: 0021-9606. DOI: `10.1063/1.1888574`.

[60] Peter H. Berens and Kent R. Wilson. "Molecular dynamics and spectra. I. Diatomic rotation and vibration". In: *The Journal of Chemical Physics* 74.9 (1981), pp. 4872–4882. ISSN: 0021-9606. DOI: `10.1063/1.441739`.

[61] L. Yuan et al. "Dynamics of molecules in extreme rotational states". In: *Proceedings of the National Academy of Sciences* 108.17 (2011), pp. 6872–6877. ISSN: 0027-8424. DOI: `10.1073/pnas.1018669108`.

[62] Milan Šindelka and Nimrod Moiseyev. "Theory of diatomic molecules in an external electromagnetic field from first quantum mechanical principles". In: *Journal of Physical Chemistry A* 110.16 (2006), pp. 5561–5571. ISSN: 10895639. DOI: `10.1021/jp057120j`.

[63] Alan Lenef et al. "Rotation Sensing with an Atom Interferometer". In: *Physical Review Letters* 78.5 (1997), pp. 760–763. ISSN: 10797114. DOI: `10.1103/PhysRevLett.78.760`.

[64] Yuxiang Yang, Giulio Chiribella, and Qinheping Hu. "Units of rotational information". In: *New Journal of Physics* 19.12 (2017), p. 123003. ISSN: 13672630. DOI: 10.1088/1367-2630/aa94e5. arXiv: 1707.05631.

[65] James P. Cryan et al. "Ensemble of Linear Molecules in Nondispersing Rotational Quantum States: A Molecular Stopwatch". In: *Physical Review X* 1.1 (2011), p. 11002. ISSN: 2160-3308. DOI: 10.1103/PhysRevX.1.011002.

[66] Hans C. Fogedby and Alberto Imparato. "Autonomous quantum rotator". In: *EPL (Europhysics Letters)* 122.1 (2018), p. 10006. ISSN: 0295-5075. DOI: 10.1209/0295-5075/122/10006.

[67] David J. (David Jeffery) Griffiths. *Introduction to quantum mechanics*. Pearson Prentice Hall, 2005, p. 468. ISBN: 0131118927.

[68] Donald A. (Donald Allan) McQuarrie and John D. (John Douglas) Simon. *Physical Chemistry : A Molecular Approach*. University Science Books, 1997, p. 1360. ISBN: 0935702997. DOI: 10.1021/ed075p545.

[69] W. Heitler and G. Herzberg. "Gehorchen die Stickstoffkerne der Boseschen Statistik?" In: *Die Naturwissenschaften* 17.34 (1929), pp. 673–674. ISSN: 00281042. DOI: 10.1007/BF01506505.

[70] Franco Dalfovo et al. "Theory of Bose-Einstein condensation in trapped gases". In: *Reviews of Modern Physics* 71.3 (1998), pp. 463–512. ISSN: 0034-6861. DOI: 10.1103/RevModPhys.71.463. arXiv: 9806038 [cond-mat].

[71] J M Lattimer and M Prakash. *The Physics of Neutron Stars*. 2004. DOI: 10.1126/science.1090720. arXiv: 0405262 [astro-ph].

[72] Michael Edward Peskin and Daniel V. Schroeder. *An Introduction To Quantum Field Theory*. Westview Press, 1995, p. 864. ISBN: 0201503972.

[73] Dennis Dieks and Andrea Lubberdink. "How Classical Particles Emerge From the Quantum World". In: *Foundations of Physics* 41.6 (2011), pp. 1051–1064. ISSN: 00159018. DOI: 10.1007/s10701-010-9515-2. arXiv: 1002.2544.

[74] Michael J. Biercuk and David J. Reilly. "Quantum computing: Solid-state spins survive". In: *Nature Nanotechnology* 6.1 (2011), pp. 9–11. ISSN: 17483395. DOI: 10.1038/nnano.2011.261.

[75] A. M. Souza, G. A. Alvarez, and D. Suter. "Robust dynamical decoupling". In: *Philosophical Transactions of the Royal Society A: Mathematical, Physical and Engineering Sciences* 370.1976 (2012), pp. 4748–4769. ISSN: 1364-503X. DOI: 10.1098/rsta.2011.0355.

[76] Q. A. Turchette et al. "Decoherence and decay of motional quantum states of a trapped atom coupled to engineered reservoirs". In: *Physical Review A* 62.5 (2000), p. 053807. ISSN: 1050-2947. DOI: 10.1103/PhysRevA.62.053807.

[77] C. J. Myatt et al. "Decoherence of quantum superpositions through coupling to engineered reservoirs". In: *Nature* 403.6767 (2000), pp. 269–273. ISSN: 0028-0836. DOI: 10.1038/35002001.

[78] C. F Roos et al. "Nonlinear coupling of continuous variables at the single quantum level". In: *Physical Review A* 77.4 (2008), p. 40302. ISSN: 1050-2947. DOI: 10.1103/PhysRevA.77.040302.

[79] Dylan J Gorman et al. "Two-mode coupling in a single-ion oscillator via parametric resonance". In: *Physical Review A* 89.6 (2014), p. 062332. ISSN: 1050-2947. DOI: 10.1103/PhysRevA.89.062332.

[80] Ronald F. Fox and Mee Hyang Choi. "Generalized coherent states and quantum-classical correspondence". In: *Physical Review A* 61.3 (2000), p. 032107. ISSN: 1050-2947. DOI: 10.1103/PhysRevA.61.032107.

[81] Benjamin A. Stickler, Farhad Taher Ghahramani, and Klaus Hornberger. "Rotational Alignment Decay and Decoherence of Molecular Superrotors". In: *Physical Review Letters* 121.24 (2018), p. 243402. ISSN: 0031-9007. DOI: 10.1103/PhysRevLett.121.243402.

[82] Benjamin A. Stickler, Björn Schrinski, and Klaus Hornberger. "Rotational Friction and Diffusion of Quantum Rotors". In: *Physical Review Letters* 121.4 (2018), p. 040401. ISSN: 0031-9007. DOI: 10.1103/PhysRevLett.121.040401.

[83] Changchun Zhong and F. Robicheaux. "Decoherence of rotational degrees of freedom". In: *Physical Review A* 94.5 (2016), p. 052109. ISSN: 2469-9926. DOI: 10.1103/PhysRevA.94.052109.